Design and Fabrication of Diffusion doped PIN Waveguides for Silicon Photonics

A THESIS

submitted by

SAKTHIVEL PAVADAI

for the award of the degree

of

MASTER OF SCIENCE

(by Research)

DEPARTMENT OF ELECTRICAL ENGINEERING.
INDIAN INSTITUTE OF TECHNOLOGY MADRAS.

October 2015

THESIS CERTIFICATE

This is to certify that the thesis titled **Design and Fabrication of Diffusion doped PIN Waveguides for Silicon Photonics**, submitted by **SAKTHIVEL PAVADAI**, to the Indian Institute of Technology, Madras, for the award of the degree of **Master of Science**, is a bonafide record of the research work done by him under our supervision. The contents of this thesis, in full or in parts, have not been submitted to any other Institute or University for the award of any degree or diploma.

Dr. Nandita Dasgupta
Research Guide
Professor
Dept. of Electrical Engineering
IIT-Madras, 600 036

Dr. Bijoy Krishna Das
Research Guide
Associate Professor
Dept. of Electrical Engineering
IIT-Madras, 600 036

Place: Chennai, India

Date: Mon 5th Oct, 2015

Dedicated to my parents, **Mr. Pavadai G** and **Mrs. Mallika P** for their extreme love, support, motivation and patience and to my music guru, Arul Isai Siddhar, **T. M. Soundararajan**, who inspired music in me through his songs.

ACKNOWLEDGEMENTS

I would like to express my deep gratitude to my research supervisors **Prof. Nandita DasGupta** and **Dr. Bijoy Krishna Das** for their dedicated guidance, enthusiastic encouragement and useful comments of this research work. Doing research under the guidance of Prof. Nandita Dasgupta is a unique experience. Her clarity of thought to get into bottom of the research bottle neck was indeed a great help to shape up the present thesis. The courses taught by **Prof. Nandita Dasgupta** viz, VLSI technology, Solar cell device physics and technology, MOS device modeling and Compound semiconductors were lively and very much helpful throughout my research. It would not have been possible to fabricate variable optical attenuators and optical modulators in SOI platform without her suggestions and guidance during the design, fabrications and optimization of fabrication process steps. I once again deeply thank her for her keen interest, passions and invaluable time she spent on discussions towards my progress in research.

My grateful thanks to **Dr. Bijoy Krishna Das** for introducing me to the new field of integrated optoelectronics through the course "integrated optical devices and circuits" in unique way. The course was very much needful to understand and design the variable optical attenuators and optical modulators from the basic. I am very much thankful to him for the invaluable time he had spent with me on discussions and interpretations of experimental results and offering professional advise for planning various simulations and experiments. His excellent guidance and constant motivation instilled enormous confidence to strive hard to excel in research. His suggestions during the phase of analysis, design and characterization of various devices was very much important and encouraging. I astonish to see his way of analyzing the basic scientific processes and technology in different views and ways. I personally feel that the amount of freedom he gives to his research students on discussing various topics and related issues during the weekly group meetings make a progressive and synergistic research environment.

I would like to express my sincere thanks to **Prof. Amitava Dasgupta**, laboratory head, microelectroics lab, for his suggestions during my M.S seminar. I extend my thanks to **Dr. Anjan Chkrovarthy** for his suggesstions during the seminar. I thank my GTC members **Prof. Enakshi Bhattacharya**, **Dr. G. Ramanathan**, department of Chemical Engineering and comity chair **Prof. Vinitha Vasudevan** for their comments and valuable suggestions during the GTC meetings and seminar.

I appreciate **Mr. Rupesh Kumar Navalakhe** and **Mr. John P. George** for their encouragement during my earlier days at IOLAB. I express my thanks to **Mr. Gaurang Bhatt** for his help and wish on my research and career. I thank **Mr. Krishna Karthik** and **Sreevathsa Bhatt**. I express my special thanks to **Mr. I. Solomon Krubhakar** for his personal encouragement and discussions on multimode interference couplers. I express my deep thanks to late **Ms. Neeti Anand**, an internship student at IOLAB, for her insightful questions on MMI and related discussions. I express my deep thanks to **Mr. R. Narendran** for his well wish and suggestions towards my career. I thank **Mr. Sujith Chandran** for his help in writing photo masks, and encouragement. I heartfelt thanks to **Mr. S. Meenatchi Sundaram** help and support at various stages of both my personal and research life at IITM. I thank **Mr. Shantanu** for his encouragement. I thank **Mr. Uppu Karthick for his encouragements**. I express my gratitude to **Mr. Harish** for his help in automating some Matlab related calculations and saving time and making our USA conference trip enjoyable. I express my thanks to **Mr. G. Sreedhar** for his help in integrating probe station with end-fire optical coupling system and for his good wishes and encouraging words whenever it was necessary. I express my special thanks **Mr. Sreevatsa Kurudi** and **Ms. Riddhi Nandi** for their assistance and help during the characterization of the fabricated samples. I express my thanks to **Mr. Sidharth Raveendran**, **Mr. Parimal Shah**, **Mr. Varun Singh**, **Mr. Dadavalli Dudekula**, **Mr. Saket Kaushal**, **Mr. Vivek**, **Ramesh K Gupta** and **Mr. Mandar**, **Ms. Rashmi Joshi**, **Ms. Seethalakshmi**, **Ms. Sireesha Nambighari** and **Ms. Sumi R** for their encouragements.

I express my special thanks to **Mr. V. Mohana Sundaram** for his encouragement, discussions, timely help and interest on my career throughout my time at IITM. I thank **Mr. Kamesh** for the discussions on Medici. I thank **Dr. Kalai Selvi**, **Mr. Sreejith**

Thyku, **Mr. A. Vijayakumar**, **T. Sreenidhi**, **Dr. Balachndra Achar** and **Mr. Noel Prashanth** for their wishes and encouragements. I thank **Mr. Rahul Kumar, Ms. Meenakshi rajasekaran, Mr. Vikram Vamsi, Mr. K. Naveen, Ms. Noel Augutine, Mr. George Thachil** and **Mr. Gourab Dutta** for their wishes.

I express my thanks to **Mr. C. Rajendran**, Jr. technical superintendent for his technical support in the microelectronics lab. I express my special and deep gratitude to **Mr. J Prakash**, Jr. technician in the lab for his extraordinary dedication and help during the fabrication and characterization of the samples in the microelectronics and Integrated Optoelectronics Laboratories. I express my thanks to **Mr. T. Sridhar**, attendant for his support in the microelectronics lab. I thank **Mr. B. Deepak**, technitian IOLAB for his wishes. I thank **Ms. Tamil Selvi**, senior clerk in the department office for her wishes and support.

I express my extreme gratefulness to all my physics professors at Government Arts College, Thiruvannamalai for their dedication and unforgettable teachings, I also owe a lot to Late. **Prof. S. Marga Sahayam** for his beautiful teachings and every day examples in chemistry. I express my gratitude to **Swamy Sathyapriyananda**, Sri Ramakishna Mission Vivekananda college, Mylapore for his blessings and help during my post graduation.

I express my heartfelt thanks to my dear friend **Mr. B. Seenuvasan** for his love and wishes. I thank my R.K.M. Vivekanada college friends **Mr. M. Anand Raj** and **Mr. R. Maheswaran** for their wishes and help. I also express my garatitude to my Kerala friend **Mr. Arun K.N** for his help during my difficult time.

Words are very limited to thank my father **Mr. G. Pavadai**, mother **P. Mallika**, brother **P. Saravanan**, sister **P. Sarala** brother-in-law **Mr. E. Balamurugan** and their children **B. Nishanth** and **B. Rakshitha** for their extreme love.

ABSTRACT

KEYWORDS: SOI, Waveguides, Integrated Optics, Silicon Photonics, Modulator, Variable optical attenuator, Diffusion doping, Mach-Zehnder Interferometer.

Design of diffusion doped PIN structures with large cross-section ($\sim 25\mu m^2$) single mode rib waveguide structures on SOI platform have been studied. Various simulation tools were used for the final design of p-i-n optical phase modulator,variable optical attenuator and Mach-Zehnder modulator. These devices were fabricated with optimized design parameters by using conventional microelectronic technology. The DC modulation characteristics of Mach-Zehnder modulator and the attenuation characteristics of variable optical attenuator were experimentally studied and compared with the simulation results. The typical attenuation of VOA was measured to be 2(3.6) dB/mm for TE(TM) - polarized light ($\lambda \sim$ 1550 nm) at a forward current of 15 mA. The extinction ratio of the modulator were found to be 12.4 and 12 dB for TE and TM polarizations respectively. These measured characteristics were found in close agreement with the simulated characteristics.

TABLE OF CONTENTS

LIST OF TABLES

LIST OF FIGURES

ABBREVIATIONS

Acronyms

Band C	Conventional wavelength band ($\lambda \sim 1527$ to 1567 nm)
Band L	Long wavelength band ($\lambda \sim 1567$ to 1607 nm)
BOX	Buried Oxide
BPM	Beam Propagation Method
CMOS	Complementry Metal Oxide Semiconductor
DI	De-ionized (water)
DUV	Device Under Test
FEM	Finite Element Method
FSR	Free Spectral Range
ICP	Inductively Coupled Plasma
LCRW	Large Cross-section Rib Waveguide
MZI	Mach Zehnder Interferometer
MZM	Mach Zehnder Modulator
PPR	Positive Photo Resist
LCRW	Large Cross-section Rib Waveguide
RIE	Reactive Ion Etching
SEM	Scanning Electron Microscope
SMF	Single Mode Fiber
SOI	Silicon-On-Insulator
TE	Transverse Electric (polarization)
TM	Transverse Magnetic (polarization)
TOX	Top Oxide Cladding
EMI	Electromagnetic interference
UV	Ultra-Violet
VOA	Variable Optical Attenuator

Chemical Names

Al	Aluminum
Ar	Argon
B_2O_3	Boron Trioxide
BN	Boron Nitride
CHF_3	Tri-fluoro Methane
Cr	Chromium
HF	Hydro Fluoric Acid
HNO_3	Nitric Acid
H_2O	Water
H_2O_2	Hydrogen Peroxide
KOH	Potassium Hydroxide
NaOH	Sodium Hydroxide
P_2O_5	Phosphorus Pentoxide
$POCl_3$	Phosphorus Oxichloride
SF_6	Sulfur Hexafluoride
Si	Silicon
SiO_2	Silicon dioxide
TCE	Tri-chloro Ethylene

Units

dB	Decibel
dBm	Decibel milli-Watts
mA	Milli Ampere
mW	milli Watts
V	Volt
μm	Micrometer
ps	Pico Second
μ**s**	Micro Second
sccm	standard cubic centimeter per minute
mTorr	milli-Torr (of pressure)

mbar	milli-Bar (of pressure)
ml	milli-liter (of fluid)

NOTATION

$\mathbf{n}$	Refractive index
$\mathbf{n}_{eff}$	Effective refractive index
$\boldsymbol{\epsilon}$	Permitivity
$\boldsymbol{\lambda}$	Wavelength
$\boldsymbol{\beta}$	Propagation constant
$\boldsymbol{\phi}$	Phase of the EM wave
$\mathbf{R}$	Waveguide bending radius
$\mathbf{L}$	Length (refers to device length, component length)
$\boldsymbol{\kappa}$	Imaginary part of refractive index
$\boldsymbol{\alpha}$	Absorption coefficient
$\boldsymbol{\omega_x}$	Electric field distribution in horizontal direction (along x-axis)
$\boldsymbol{\omega_y}$	Electric field distribution in vertical direction (along y-axis)

CHAPTER 1

Introduction

The present work is a study of diffusion doped p-i-n waveguides and its applications to optical interconnect devices like variable optical attenuator and Mach-Zehnder Modulator in silicon-on-insulator (SOI) platform. In this introductory chapter, we first discuss briefly about the importance of interconnects in integrated circuit (IC)technology and the recent demands of broadband optical interconnects. This will be followed by problem definition / motivation and research objectives.

1.1 Technology Node and Interconnect Bottleneck

The impact of electronic integrated circuits (ICs) in modern life of humans need not be overemphasized as they are used in all kinds of electronic applications from simple calculators to super computers. A typical multi-functional IC consists of millions of semiconductor devices [1, 2] interconnected with many layers of metal tracks protected with insulating films. The metal interconnects of the IC can be classified into three types as shown in Fig.1.1, namely, local, intermediate, and global. The metal tracks interconnecting the terminals of transistors within a functional block of the IC are known as local interconnects. In general these are very short in length and hence contribute very little delay in carrying the signals among the transistors. The intermediate level interconnects (also called semi-global interconnects) carry signals and clocks within the functional block and covering a distance of a few millimeters. The metal tracks connecting various functional blocks to distribute electrical supply, signals and clocks within the IC are known as global interconnects. In general, these are very long and give rise to a large transmission delay. Therefore, high conductivity metals and low-k dielectrics are being used to keep the resistance of the metal tracks and capacitance of the interconnects minimum. (i.e. to make the RC time constant small). During the early years of manufacturing of ICs, Al/SiO_2 materials were used for interconnecting

applications [3]. Traditionally to increase the operating speed of the ICs the minimum feature sizes of the transistors and interconnects are scaled down in the industries. However, the scaling of metal interconnect leads to reduction of its cross sectional area and spacing, consequently, the interconnect delay begin to dominate in the overall delay of the circuit as shown in Fig. 1.2. Since the year of 1998, copper interconnects with various low-k dielectrics are used in IC technology [4]. However, as can be seen from Fig. 1.2, though Cu / low-k dielectric provides a low delay compared to Al/SiO_2 interconnects, even this may not be sufficient in the long run, as the interconnect delay with Cu / low-k dielectric becomes more than the logic gate delay beyond 180 nm technology node. Thus further scaling of the transistor dimensions may not result in any significant improvements in circuit performance unless the interconnect delay is reduced drastically.

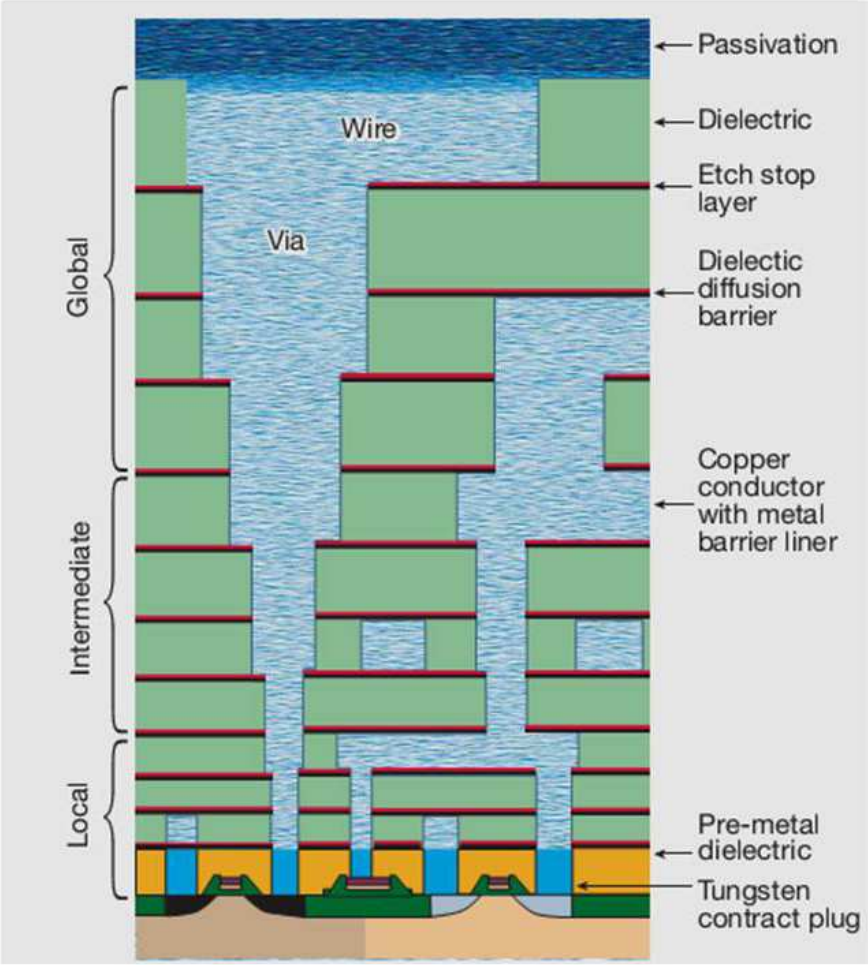

Figure 1.1: The schematic cross-section view of the multilevel metal interconnects of an IC showing local, intermediate and global interconnects [5].

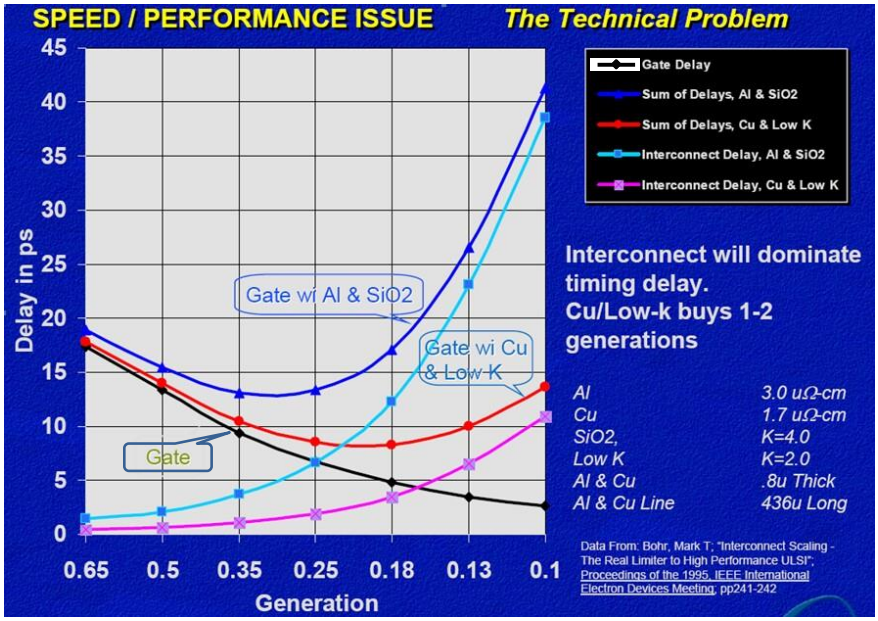

Figure 1.2: The graph showing signal processing delay of typical logic gates, propagation delay of interconnects and sum of both the delays for both Al/SiO_2 and Cu/low-k dielectric interconnect systems as a function of advancing technology nodes [6].

1.2 Optical Interconnects: Silicon Photonics

It has been proposed by scientists and engineers that a paradigm shift from metal interconnects to optical interconnects could give a solution for alleviating the problems of interconnect delay in ICs. Optical interconnection is a way of realizing communication among the electronic systems or subsystems or even devices by using modulated optical carriers. A group of photonic / optoelectronic devices connected in a proper sequence to implement the optical communication between two electronic systems is known as an optical interconnect. Fig. 1.3, shows the block diagram of the IC in which the global metal interconnects have been replaced with optical interconnects. A typical optical interconnect consists of four basic components such as a laser source, an optical modulator, a passive optical routing device (such as waveguides splitters, interleaves, MUX/DEMUX etc.) and a photo detector [7]. The data from the digital logic cell is fed in to the modulator via a driver circuit which makes voltage level (also for matching the impedance between digital logic cell and modulator) of electrical data compatible with the modulator. The modulator encodes the optical carrier obtained from the laser source in accordance with the data obtained from the driver and feeds it into the waveguide.

The waveguide routes and guides the modulated optical signal (having a certain wavelength and polarization) to the photodetector located nearby another electronic module. The photodetector converts the optical signal in to an electronic signal and sends it to the amplifier to improve the signal to noise ratio. The data is finally sent to the another digital logic cell.

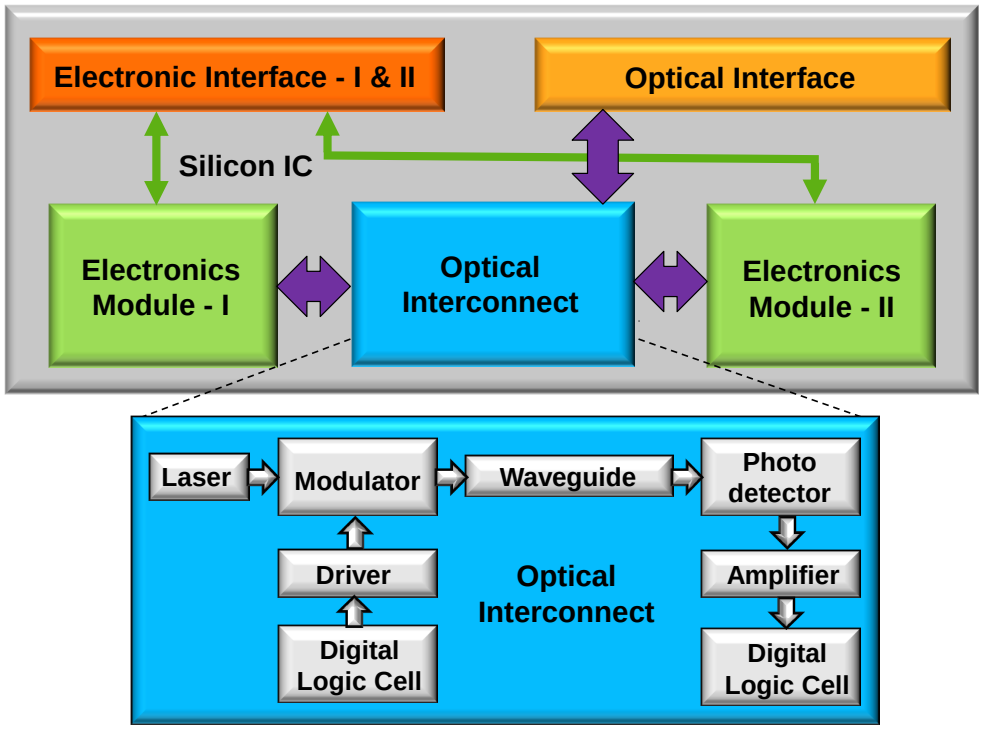

Figure 1.3: Block diagram of a basic IC in which the optical interconnects (shown in blue and violet colors) have been used in place of global metal interconnects. The figure shows, electronic modules, electrical and optical interfaces and their interconnection by optical interconnects

Optical interconnects are superior to the metal interconnects in terms of basic physics and technological aspects. They do not require metal as the medium (except in case of plasmonic waveguides) and hence there is no limitations in terms of skin effect, voltage isolation, and impedance matching among the modules of the ICs. Use of light as the information carrier puts virtually no limit on bandwidth and makes the signal's immunity power high against electromagnetic interferences (EMI) [8].

The modulation of light in a waveguide is accomplished in general by locally controlling the refractive index by applying the controlling signal. The physical effects by which the refractive index of the waveguide region may be controlled are, the acousto optic effect [9], thermooptic effect [10], Pockel's effect [11], Kerr effect [12], Frandz-

Keldysh effect [13] and plasma dispersion effect [14]. As far as crystalline silicon is considered, the plasma dispersion and thermo-optic effects are strong and Pockel's effect is absent, which is due to the centro symmetric nature of the crystal lattice of silicon. Even though silicon has relatively large positive thermo-optic coefficient ($dn/dT = 1.86 \times 10^{-4} K^{-1}$) [15], its relatively slow nature (a few MHz of operating frequency) and difficulty in localizing the heat [16] makes it less attractive. So, it is felt that the plasma dispersion is the most effective way by which the attenuation and phase modulation of light may be achieved in silicon.

For semiconductors, the change in refractive index (Δn) and optical absorption coefficient ($\Delta \alpha$) with change in electron and hole concentrations are expressed by Drude-Lorentz equations [17] as,

$$\Delta n = -\frac{e^2 \lambda^2}{8\pi^2 \varepsilon_o c^2 n} \{ \frac{\Delta N_e}{m_e^*} + \frac{\Delta N_h}{m_h^*} \} \tag{1.1}$$

$$\Delta \alpha = \frac{e^3 \lambda^2}{4\pi^2 \varepsilon_o c^3 n} \{ \frac{\Delta N_e}{\mu_e (m_e^*)^2} + \frac{\Delta N_h}{\mu_h (m_h^*)^2} \} \tag{1.2}$$

where n and α are the real and imaginary (absorption) parts of complex refractive indices of guiding medium, e is the electronic charge, λ, c and ε_o are wavelength, velocity of light and permittivity in free space respectively. The m_e^* and m_h^* and μ_e, μ_h are effective masses and mobility of electron and hole respectively, ΔN_e and ΔN_h, are change in electron and hole concentrations in cm^{-3} respectively. Soref and Bennett have estimated the numerical relations for the plasma dispersion in silicon by investigating experimental results of light absorption spectrum of silicon as a function of impurity doping concentrations. The Soref-Bennett equations for crystalline silicon at room temperature and $\lambda \sim$1550 nm are;

$$\Delta n = -\{8.8 \times 10^{-22} \Delta N_e + 8.5 \times 10^{-18} (\Delta N_h)^{0.8}\} \tag{1.3}$$

$$\Delta \alpha = 8.5 \times 10^{-18} \Delta N_e + 6.0 \times 10^{-18} \Delta N_h \tag{1.4}$$

In general for the realization of active photonic devices in silicon especially for phase-shifter applications, the plasma dispersion effect may be employed in waveguide structures in three ways, namely, by utilizing carrier accumulation in the MOS capacitor, carrier depletion in the p-n diode and carrier injection in the p-i-n diode.

The phase-shifter shown in the Fig. 1.4 consists of a lightly doped n-type substrate or body with a thin gate oxide and p-type polysilicon gate forming a MOS-capacitor-ribwaveguide structure. For good ohmic contacts, the two outer edges of polysilicon gate are heavily doped with p-type impurities and connected with metal pads. The body metal contacts are formed by the heavily doped n-type regions of the substrate. When a positive voltage is applied to the gate with respect to the body, holes are pushed near the upper interface of the gate oxide and electrons are accumulated (attracted) near the bottom surface of the gate oxide causing refractive index to change in those regions. So, the light being guided through the structure undergoes a phase shift in accordance with the refractive index change by plasma dispersion. This type of configuration utilizes accumulation of majority carriers in the waveguide regions, offering a few gigahertz of modulation bandwidth and suffer from poor modulation depth, longer interaction length, insertion loss and heavy polarization dependency.

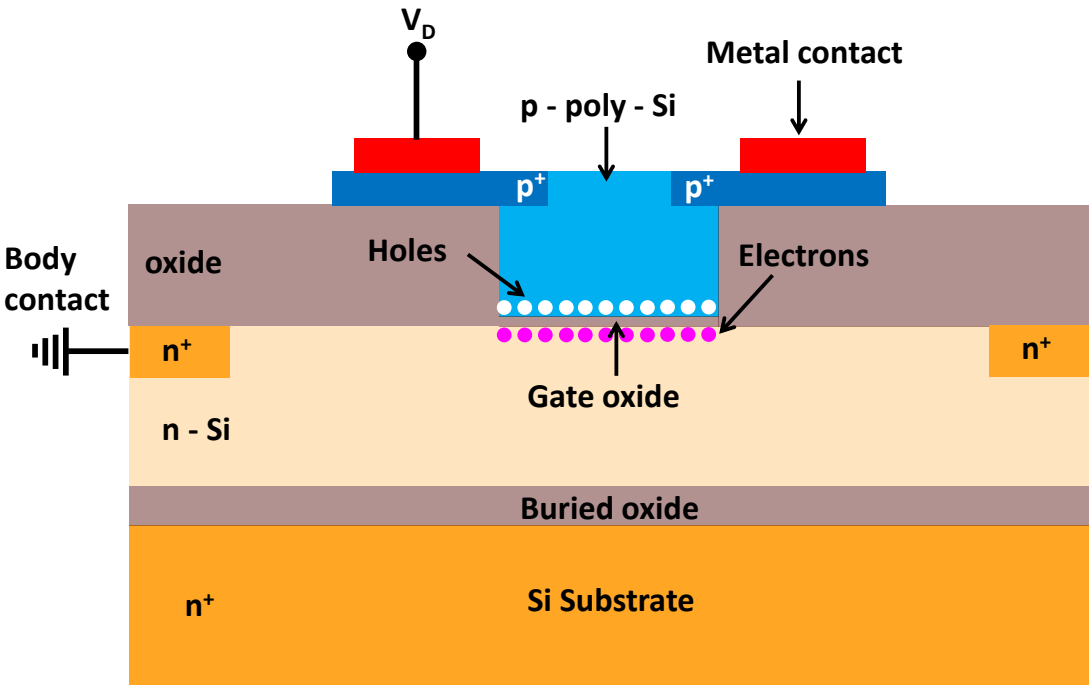

Figure 1.4: Implementation of plasma dispersion by exploiting the carrier accumulation in the MOS-capacitor-ribwaveguide in SOI platform [18].

The phase shifter shown in the Fig. 1.5 consists of a rib waveguide in which one part of the rib is doped with p-type impurities and the other side with n-type impurities forming, a lateral p-n diode. The anode and cathode metal contacts are formed with the extreme ends of the slabs after heavily doping with p-type and n-type impurities respectively. These anode (grounded) and cathode (where signal is applied) metal pads form a pair of traveling wave electrodes to operate at very high frequencies (tens of gigahertz). This structure is operated in depletion mode, causing the widening of depletion region due to the extraction of majority carriers under the rib. since this phase-shifter is operated in depletion mode, the change of carrier concentration and depletion width would be small-making the interaction length of the modulator longer.

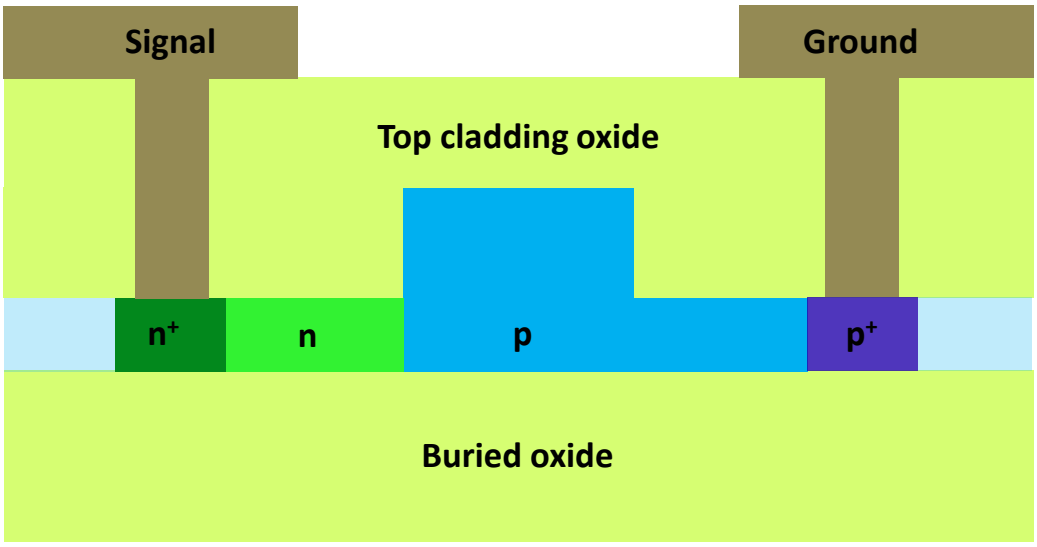

Figure 1.5: Implementation of plasma dispersion by exploiting the carrier depletion in the lateral p-n diode/waveguide in SOI platform [19]

The phase-shifter shown in the Fig. 1.6 consist of a large cross section and nearly intrinsic rib waveguide in which a thin region of the top surface of the rib is moderately doped with p-type impurities and the slab which away from the rib side walls are heavily doped with n-type impurities forms a symmetric p-i-n diode. These heavily doped slab regions act as cathodes and the top surface of the rib acts as anode. Application of forward bias to the electrodes inject the free carriers into the waveguide region and hence produce phase shift in the guided light. This type of large cross section injection based phase-shifter offer a bandwidth of the order of tens of megahertz, high modulation depth, lower length and low coupling loss with the standard single mode fiber.

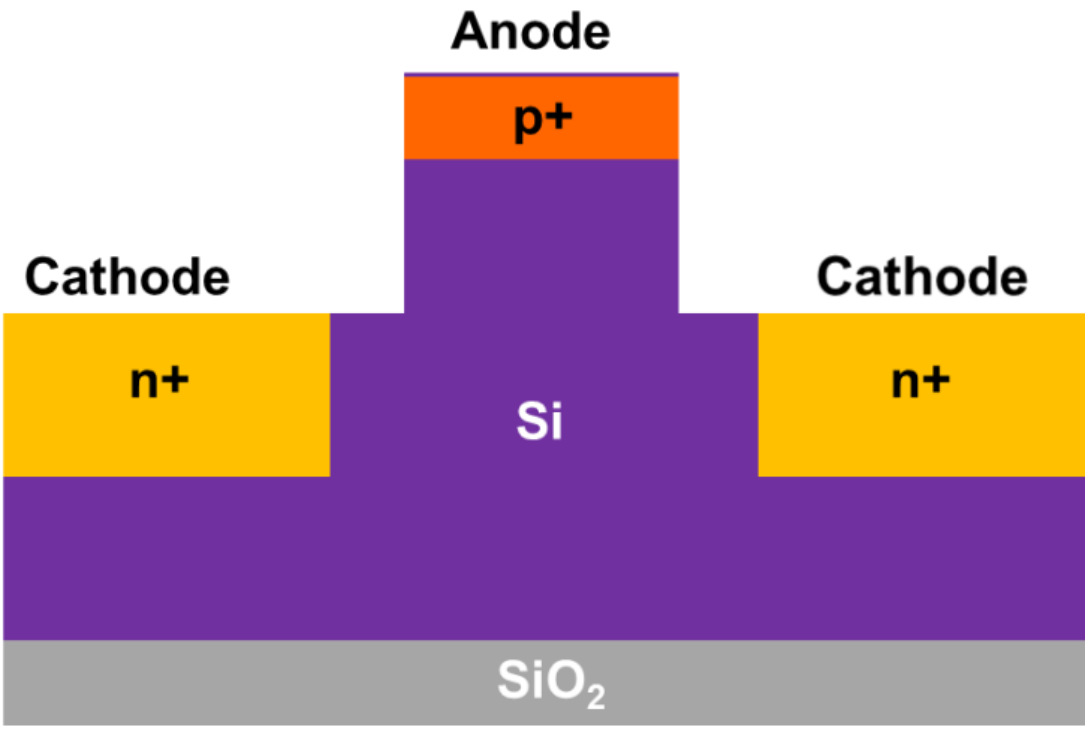

Figure 1.6: Implementation of the plasma dispersion by exploiting the carrier injection in the large cross section of symmetrical p-i-n waveguide in SOI platform [20].

1.3 Research Objective

Interest in silicon photonics is mainly due to various factors such as infrared transparency of silicon around the optical communication wavelength of 1550 nm, viability of tight light confinement and compact waveguide structures due to the high refractive index contrast between the Si and SiO_2. existence of plasma dispersion effect in silicon for making active photonic devices, potential integrability of photonic and electronic devices [21], matured CMOS processing technology [22], high volume manufacturability and cost effectiveness [23] of silicon platform. Development of high performance optical interconnects [24] for ICs in place of existing global metal interconnect has been a potential research problem for researchers for many years. Worldwide, research is being carried out at accelerated pace for developing lasers [25] [26] [27], low loss wave guides [28] and routing devices, efficient photo detectors [29], modulators [30] and variable optical attenuators [31] in silicon. Optical routing devices like rib waveguides, power splitters [32], inter-leavers and de-inter-leavers [33], MUXs / DEMUXs [34], filters [35] etc., have already been demonstrated successfully in SOI.

The variable optical attenuator and phase-shifter are very important components for vast range of applications such as for optical power control [36] and Q switching [37] in lasers, suppressing optical transients in amplifiers [38], optical power equalizations in long haul fiber optic communication channels [39], multiwavelength semiconductor optical amplifiers [40], amplitude and phase modulation of light [41], various feedback control applications [42], cross talk reduction in optical networks [43], distributions, repeaters and regeneration nodes [44].

To the best of our knowledge, for the development of VOA and optical phase-shifters, the data available in the literature so far are for devices with step impurity doping profiles, which are usually achieved by multiple ion implantations [45] [46] or / and doping during epitaxial growth [47] [48]. However, doping of impurities in silicon by using high temperature diffusion process offer high quality junctions in terms of very low leakage current [49], low surface and bulk defect concentrations [50]. Also, the thermal diffusion of impurities is being economic for batch processing of photonic integrated circuits (PICs)- it does not require high end manufacturing technologies like ion implantations, depositions and epitaxial growth. Nevertheless, the impurity diffusion and corresponding effects for the photonics devices like VOA and phase-shifters have not yet been investigated much in the literature.

The objective of this M.S. research work is to design, fabricate and characterize the VOA and Mach-Zehnder modulator (MZM) by making use of exclusively designed low loss and high efficient diffusion doped p-i-n waveguide operating in carrier injection mode.

This thesis work has been split up into five chapters. (1) Introduction; in this topic we have discussed the IC technology nodes and interconnect bottleneck, metal interconnects and their issues, optical interconnects, motivation for the research, research objective. (2) Design and simulation; discuss the design of single mode rib waveguides, of p-i-n waveguide, MZI in SOI and mask layout. (3) Process optimization and device fabrication; discuss the optimization of fabrication process using tsuprem4, mask fabrication, sample preparations, waveguide fabrications, oxidation, phosphorous and boron diffusions, metallization, and end facet preparations. (4) Experimental results and discussions; discuss the waveguide loss and mode-profile measurements, electrical

characterization of of p-i-n waveguide, optical characterization of MZI, optoelectronic characterization of VOA and MZM. (5) Conclusions; concludes the research work with summary and outlook.

CHAPTER 2

Design and Simulation

A single-mode rib waveguide structure has been designed with a lateral p-i-n diode configuration to be fabricated on a SOI substrate with 5 μm device layer thickness (see Fig. 2.1). It has been shown that such a p-i-n rib waveguide geometry can not only be used as phase-shifter but also as a variable optical attenuator for various silicon photonics applications. While optimizing various design parameters, a feasible fabrication process-line (see Fig. 2.2) has been kept in mind.

In section 2.1, we have discussed about SOI rib waveguides and single-mode guiding condition. The effects of p-type / n-type diffusion doping on guided mode (with and without biasing) have been discussed in section 2.2. The p-i-n waveguide has been integrated with one of the arms of suitably designed Mach-Zehnder interferometer - design and performances have been presented in section 2.3. Finally, the conclusions are made in section 2.4.

2.1 Single Mode Rib Waveguides

Single mode waveguide is a fundamental building block for developing variety of integrated optic and optoelectronic devices. The schematic cross section view of a typical rib waveguide with oxide cladding on its surfaces (TOX) and buried silicon dioxide (BOX) at the bottom of the silicon core is shown in Fig. 2.1. Since the fabrication of both VOA and modulator require hard masking layers during diffusion and passivating layer(s) (silicon dioxide or silicon nitrides) for their reliable operation, we have included a uniform layer of silicon dioxide over the waveguide sufaces in its design. The fabrication flow shown in Fig. 2.2 justifies (discussed in detail in chapter 3) the requirement of silicon dioxide of the waveguide top surfaces.

The vertical confinement of light in SOI rib waveguide is achieved due to the refractive index difference between the top and bottom cladding. The horizontal confinement

is partly achieved due to the rib region. However, one can design a rib waveguide to support only the fundamental mode by maintaning a certain range of values of ratio between the slab height (h) to rib height (H) for a given width (W) of the waveguide.

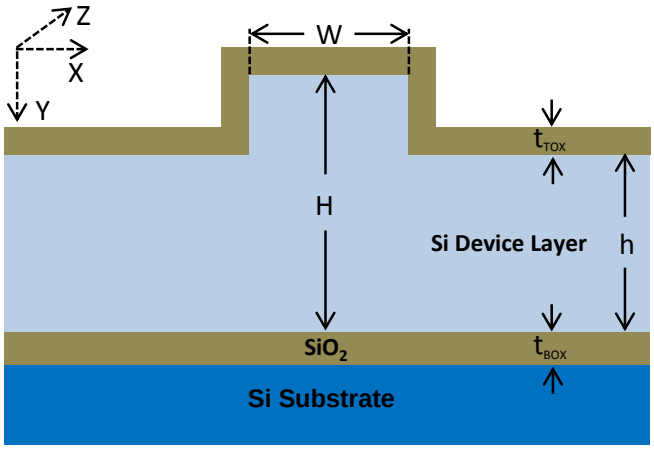

Figure 2.1: Schematic cross-section view of the SOI rib waveguide with silicon dioxide top cladding.

In order to estimate the waveguide dimensions, viz. width (W), height (H) and slab heigth (h), which ensure single mode guiding at around $\lambda \sim 1550$ nm, finite element method simulations were carried out using Rsoft-FEMSim tool to obtain the effective indices of first four eigen modes of the rib waveguide while varying W with h as a parameter for $H = 4$ μm, 4.5 μm and 5 μm respectively. Similar simulation was carried out for the slab waveguide, to calculate the effective index of the fundamental mode for various values of h. As we know from the concept of effective indices of the eigen modes, a rib waveguide would become multimoded if the effective index of the fundamental mode of the slab region becomes greater than that of the effective index of the first order mode of the rib region. For every values of h, we find the single mode cut-off value of W for above mentioned three values of H. Fig. 2.3 shows curves in $W - h$ plane with H as a parameter. For each values of H, the region below the curve ensures the single mode range of values of (W, h) and above it the waveguide becomes multimoded.

In general, under carrier injection mode the operating speed of the p-i-n waveguide is limited by its RC time constant, transit time of the free carriers and life time of minority carriers. For efficient phase modulation and attenuation, a waveguide is expected to have a low loss and tighter confinement of light and for high speed operation it requires

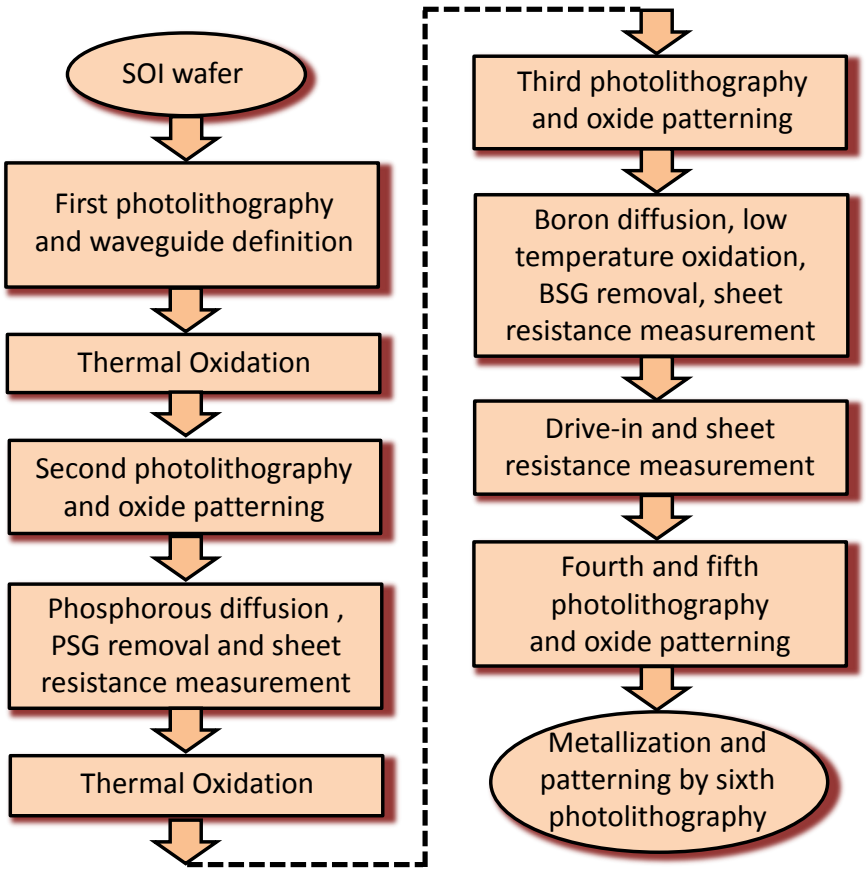

Figure 2.2: Flow chart showing fabrication steps for VOA and MZM on SOI substarte.

Table 2.1: Optimized waveguide parameters, effective indices and effective guided mode-sizes (1/e full width) of p-i-n waveguide and interconnect passive waveguides. The refractive index of silicon and silicon dioxide cladding are considered to be 3.4777 and 1.5277 respectively at a wavelength of 1550 nm.

Waveguides	W (μm)	H (μm)	h (μm)	n_{eff}^{TE}	n_{eff}^{TM}	Mode-Size (TE-pol) (μm^2)	Mode-Size (TM-pol) (μm^2)
p-i-n waveguide	4	4.5	3	3.4711	3.4708	5.37×3.34	5.16×3.43
Interconnect passive waveguide	5.5	4.5	3	3.4753	3.4752	5.64×3.5	5.55×3.47

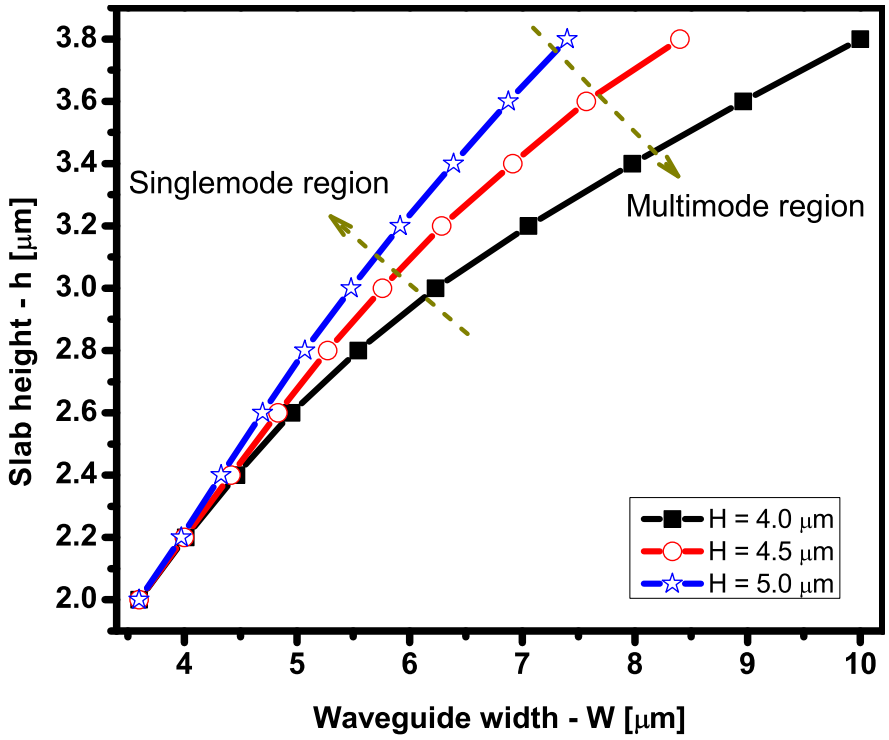

Figure 2.3: A family of curves in $W - h$ plane for different values of H showing the regions for single mode and multimode operations of the SOI waveguide. The values of W and h in the regions above each one of the curves satisfy single mode guiding and below the waveguide become multimoded.

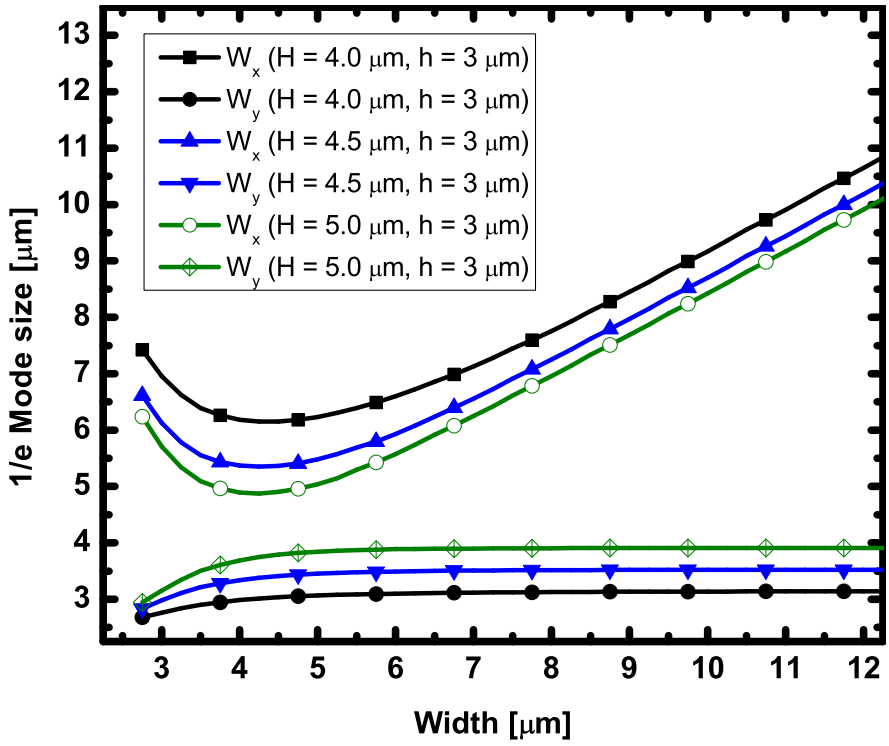

Figure 2.4: Effective mode size ω_x (along x coordinate) and ω_y (along y coordinate) for the fundamental mode of the oxide cladded SOI rib waveguide as a function of width of the waveguide W.

a shorter transit time - demanding smaller W. Hence, a single mode rib waveguide with dimensions of H = 4.5 μm, h = 3 μm and W = 4 μm has been chosen for making of p-i-n waveguide as it offer a tight confinement of field along x direction. From Fig. 2.4 it is known that highest mode confinement could be obtained when $3.5 \leq W \leq 5\ \mu m$. For lower coupling loss with the single mode fiber we have chosen the dimensions, H = 4.5 μm, h = 3 μm and W = 5.5 μm for interconnecting passive waveguides which would be used to design bend waveguides, and connect with the input and output ports of p-i-n waveguides, Mach-Zehnder interferometers in their design. The dimensions of the waveguides, guided fundamental mode profile and corresponding effective indices have been listed in Table. 2.1.

2.2 p-i-n Waveguide

The p-i-n waveguide is a basic active device which is used in the designs of VOA and MZM. The 2D device simulator Medici has been used for the design and optimization of the p-i-n diode / waveguide. In order to obtain better overlap between the injected carrier and to have improved speed of response of the p-i-n waveguide, the single mode rib waveguide width (W) is reduced to 4 μm and with which p^+ and n^+ regions of width W_d, junction depth Y_j, are introduced at 'g' distances from the left and right side walls of the rib as shown in Fig. 2.5. The 'i' region of the of p-i-n waveguide may be lightly doped with acceptor or donor impurities. In the present case we consider it as a lightly doped p-type region (also called as π region) with uniform impurity concentration of N_B = $2.5\times10^{12}\ cm^{-3}$. This holds a spacing of D_x between the inner edges of doping windows. The p^+ and n^+ regions are assumed to be diffused with boron and phosphorous impurities respectively with Gaussian distribution profiles having a surface concentration N_s.

2.2.1 Effect of variations in diffusion profile parameters

In order to investigate the effect of variations in design parameters of p-i-n waveguide viz. Y_j, D_x, and N_s on steady state I-V characteristics, carrier distributions and transient

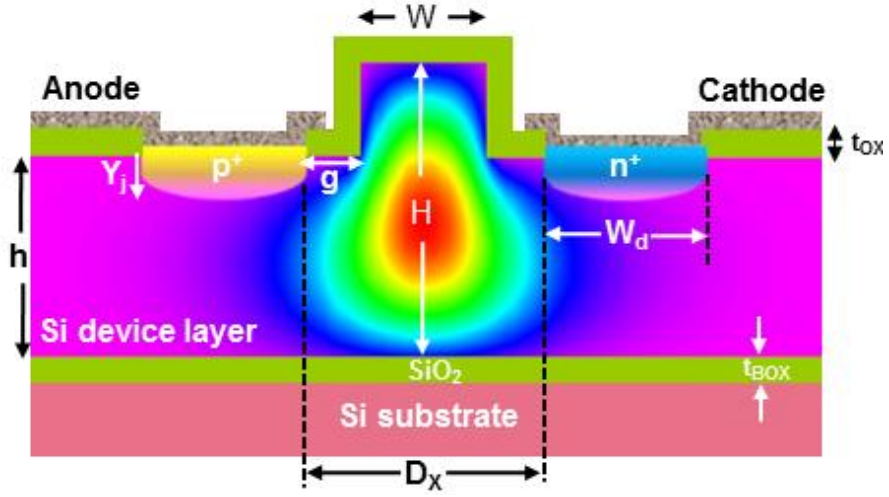

Figure 2.5: Schematic cross-section view of the oxide cladded SOI rib waveguide showing p^+ and n^+ doped regions, metal contacts and single mode electric field profile (TE polarization) of guided light at λ = 1550 nm (simulated) - making a complete p-i-n diode cum waveguide.

responses, simulations were carried out against the variations in each one of the above mentioned parameters while freezing the values of remaining parameters.

Variations in junction depth

At a forward biased state of the p-i-n waveguide (say at 1 V) the carrier concentration profiles for electrons $n(y)$ and holes $p(y)$ are monitored under the rib. The peak concentration of electrons $n_0(y_0)$, holes $p_0(y_0)$ and corresponding positions (y_0) are estimated for various values of Y_j. It is clear from Fig. 2.6 and Fig. 2.7, when the junctions of p^+ and n^+ regions become deeper, the peak values of carrier concentration under the rib and the corresponding positions along the y coordinate are increasing. It is also noted from Fig. 2.8 that when the junction depth reduces the carrier concentration under the rib decreases. Which leads to a reduction in interaction of optical fields with free carriers. On the other hand when the junction is deeper there is heavy optical loss due to mode overlapping with doped regions because of laterally diffused impurities. So, the optimum junction depth Y_j = 1 μm is chosen for the final design.

The current-voltage (I-V) characteristics of the p-i-n waveguide shows increased forward current and decreased dynamic resistance when the junction depth is decreased from 2.0 to 0.5 μm as shown in Fig. 2.8, for a forward bias voltage range of 0 V to

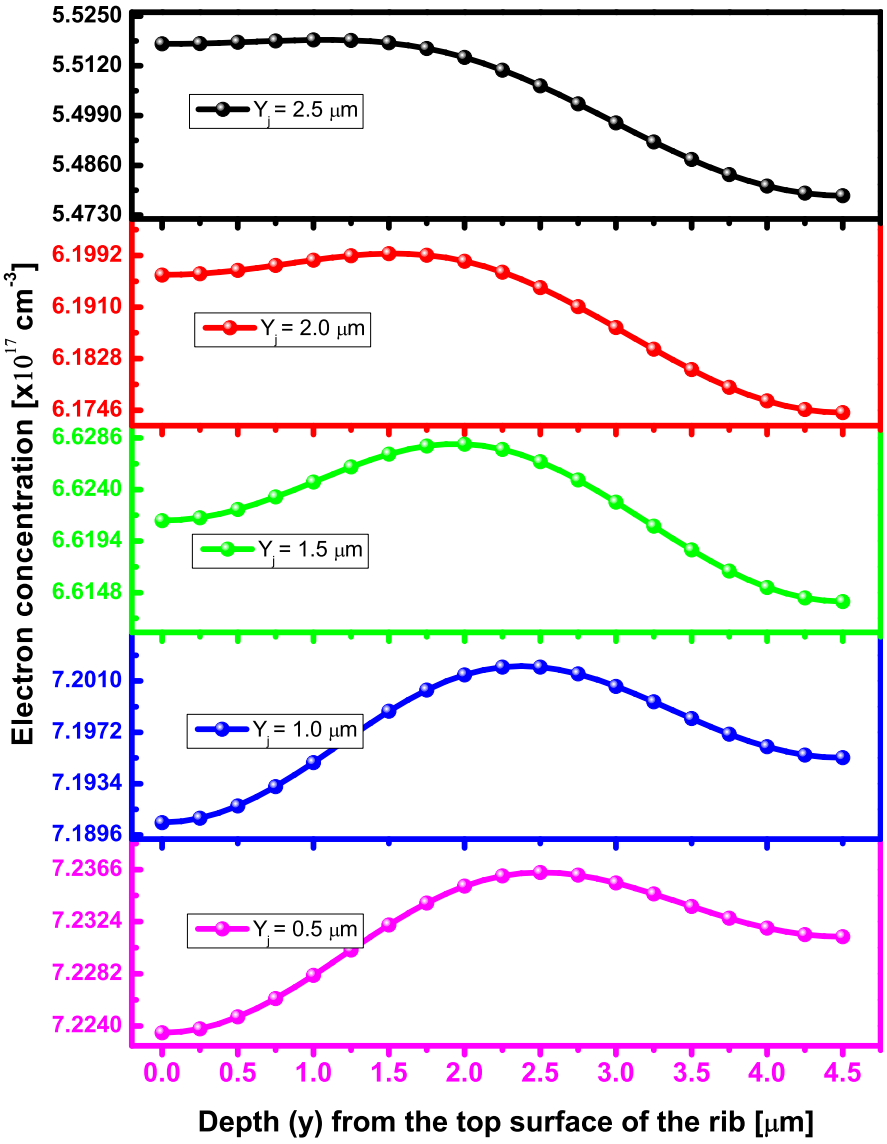

Figure 2.6: Depth dependent free electron concentration monitored from the interface between silicon and top oxide cladding (TOX) to the silicon and BOX interface of the p-i-n waveguide for 1 V forward bias with junction depth Y_j as a parameter.

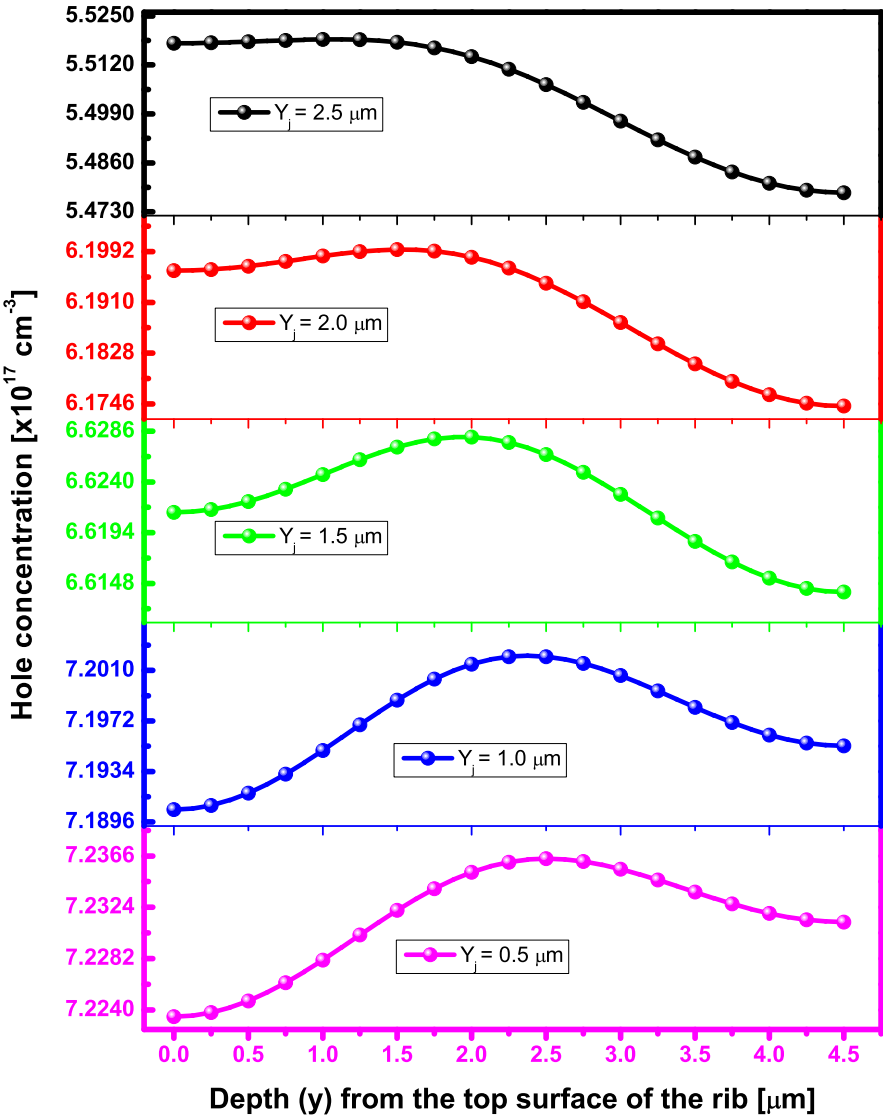

Figure 2.7: Depth dependent free hole concentration monitored from the interface between silicon and top oxide cladding (TOX) to the silicon and BOX interface of the p-i-n waveguide for 1 V forward bias with junction depth Y_j as a parameter.

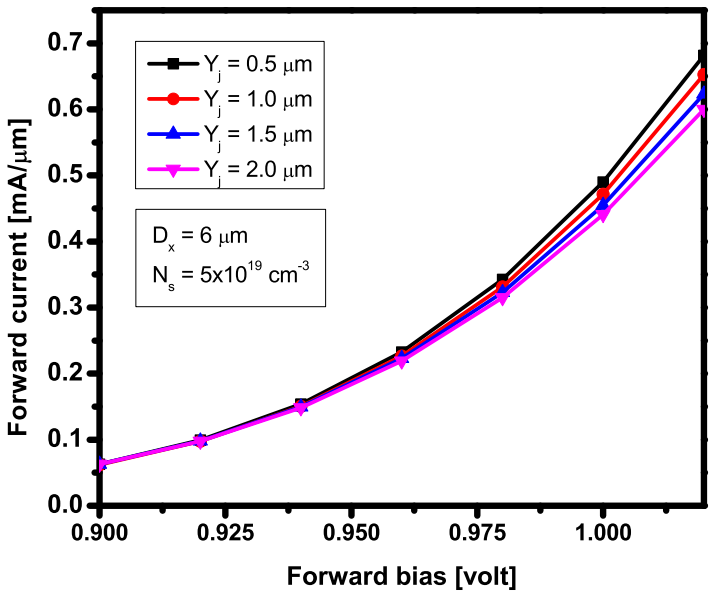

Figure 2.8: Steady state I-V characteristics of the p-i-n waveguide with junction depth Y_j as a parameter, showing increasing forward current with decreasing junction depth.

1.3 V. When the voltage dependent effective index and effective absorption of the p-i-n waveguide are calculated for Y_j = 0.5 μm, 1.0 μm and 1.5 μm, we observe that the former is exponentially decreasing and the later is exponentially increasing with voltage. However, as shown in the Fig. 2.21 for lower values of Y_j (0.5 μm) their change is steeper than for higher values. From this experiment it is known that the p-i-n waveguides with shallow junction depth would be a better choice for the good control of index and absorption upon carrier injection. Since the achievement of shallow junctions in silicon by high temperature diffusion process would be difficult, we have chosen the junction depth of 1 μm for the final design.

Variations in spacing between doping windows

In this simulation, the distribution of free carriers, net recombination-rate profile for electron-hole pairs along y coordinate and transient times (rise and fall times) are observed while varying the distance between the nearest edges of p^+ and n^+ diffusion windows (D_x) of p-i-n waveguide for N_s = 5×10^{19} cm^{-3} and Y_j = 1 μm.

As shown in the Fig. 2.9, the net recombination rate for both electrons and holes under the rib increases from $2 \times 10^{24}\ cm^{-3}s^{-1}$ to $2.54 \times 10^{24}\ cm^{-3}s^{-1}$ with decreasing values of D_x.

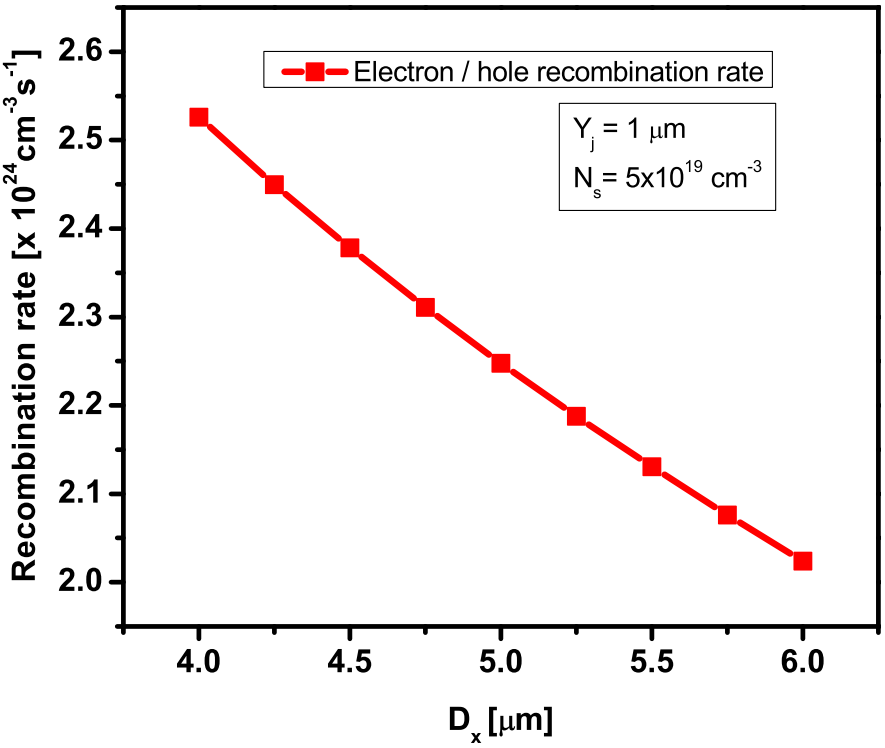

Figure 2.9: Net recombination rate for electrons or holes at y = 2.3 μm (at the center of the guided mode profile) as a function of the spacing between the closer edges of p^+ and n^+ windows at 1 V forward bias.

Transient response of the p-i-n waveguide (see Fig. 2.11 for example) for different values of D_x is studied while applying a pulse-voltage ranging from 0.5 V to 1.5 V and found that the rise time (fall time) decreases from 81.3 (63.5) ns to 50.2 (46.3) ns when D_x is reduced from 6 μm to 3 μm as shown in Fig. 2.11. This type of transient behavior implies that for a high speed operations the diffusion windows situated on both sides of the rib may be kept close to each other. However, in order to avoid overlapping of guided mode field with the doped regions and hence the loss, the value of D_x has been chosen as 6 μm, which is little greater than the lateral mode size of 5.5 μm for TE polarization at λ = 1550 nm. The forward bias current of the p-i-n waveguide is observed as a function of forward bias voltage for different values of D_x. As shown in the Fig. 2.12, when D_x is decreased, we find that the forward current and the dynamic conductance are increasing.

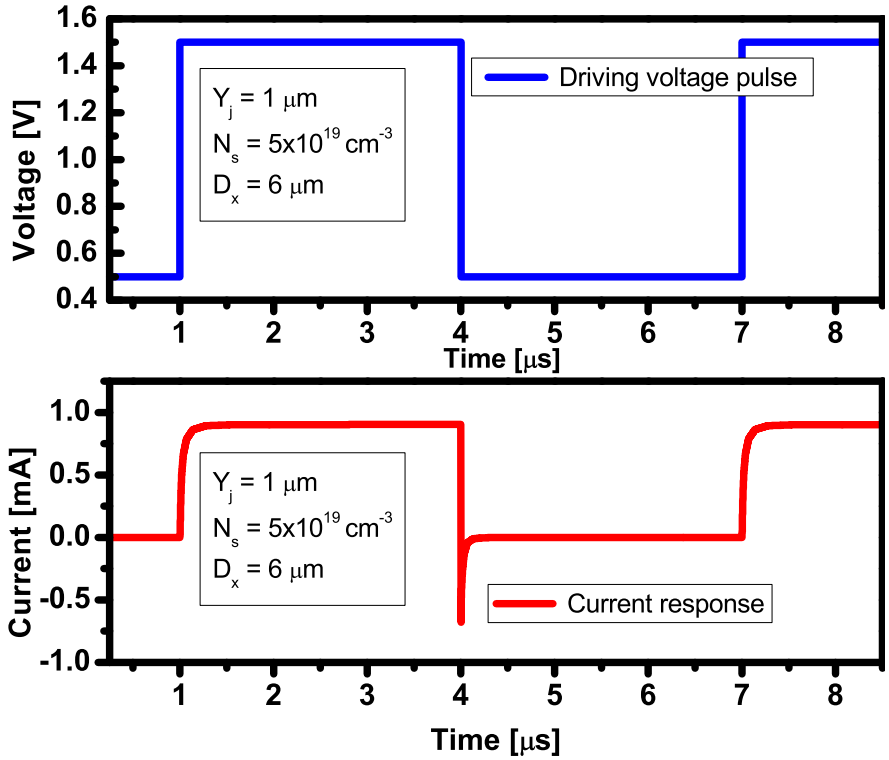

Figure 2.10: Rise time of 81.3 ns and fall time of 63.5 ns are exhibited by the p-i-n waveguide when excited with a pulse of voltage ranging from 0.5 V to 1.5 V - estimated from Medici simulations.

Variations in surface doping concentrations

In this simulation the surface impurity concentrations of p^+ and n^+ diffusion windows are varied from $2 \times 10^{19}\ cm^{-3}$ to $1 \times 10^{20}\ cm^{-3}$ when Y_j = 1 μm, D_x = 6 μm to monitor the net recombination rate for electrons and holes from the surface of each doping window to the BOX layer. The above specified range of concentrations have been chosen, by considering the solid solubility limits of boron and phosphorus in silicon at normal diffusion temperatures.

As shown in Figs. 2.13 and 2.14, the net recombination rate for electrons and holes near by the top surface of the doping windows are found to be increasing with surface impurity concentrations. This actually leads to a betterment of ohmic contact between the deposited metal film and silicon, fall of average minority carrier life time and hence the low diffusion capacitance - leads to faster device response.

The rise and fall time characteristics with doping concentrations of the p+ and n+ regions have been obtained by applying a pulse with rise and fall times of 0.1 ns, width

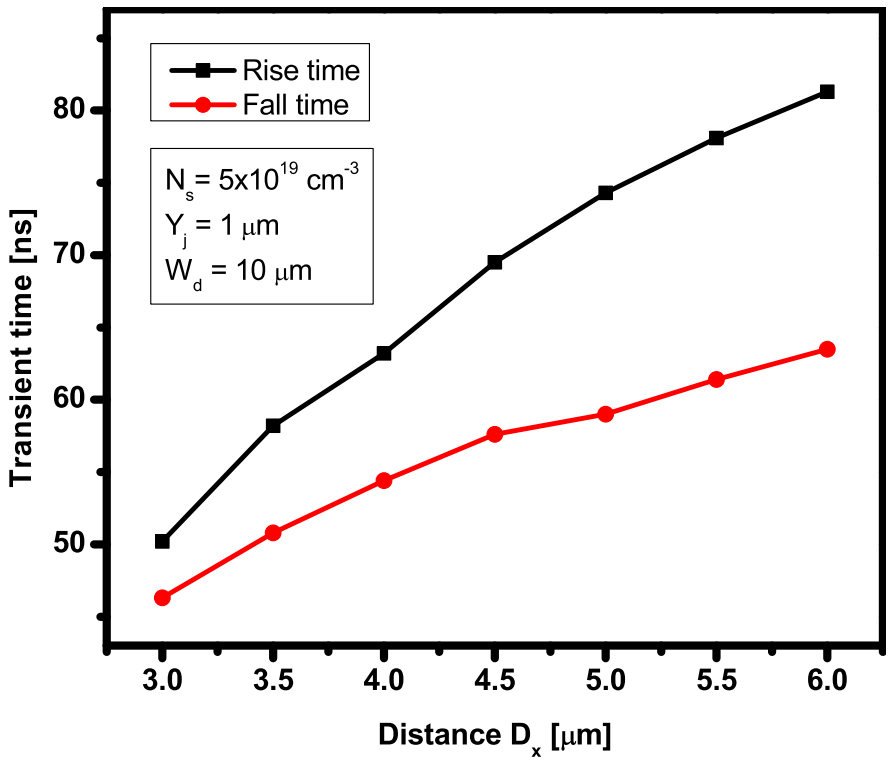

Figure 2.11: Rise time and fall time as a function of distance between the diffusion window D_x of p-i-n waveguide when applied with a pulse of voltage ranging from 0.5 V to 1.5 V. It is clear from this figure that both rise and fall times are getting increased when D_x is increased from 3 μm to 6 μm.

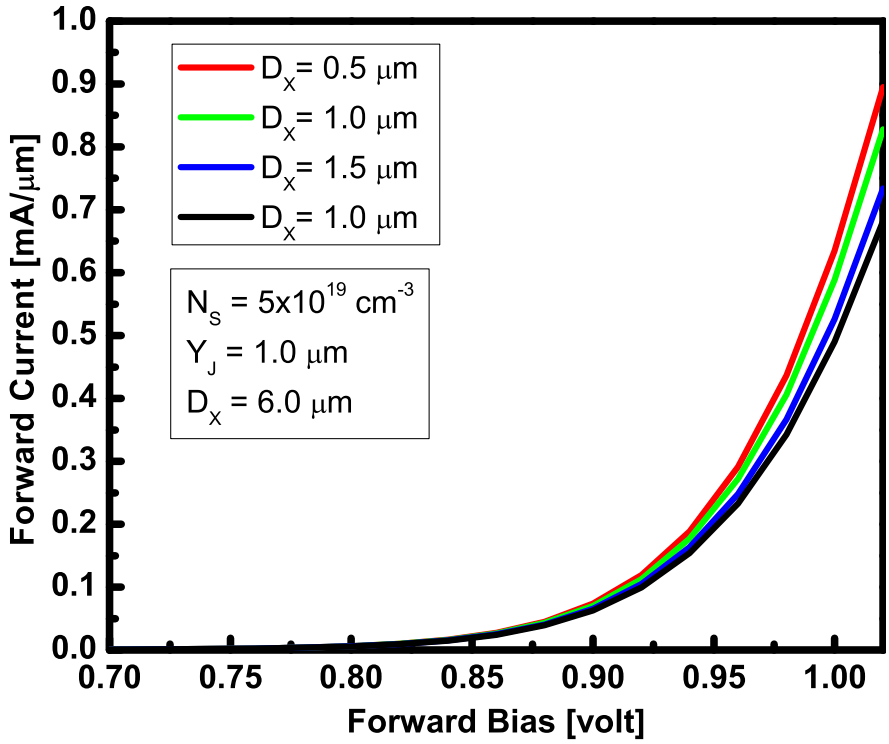

Figure 2.12: Steady state I-V characteristics of p-i-n waveguide for different values of the spacing D_x.

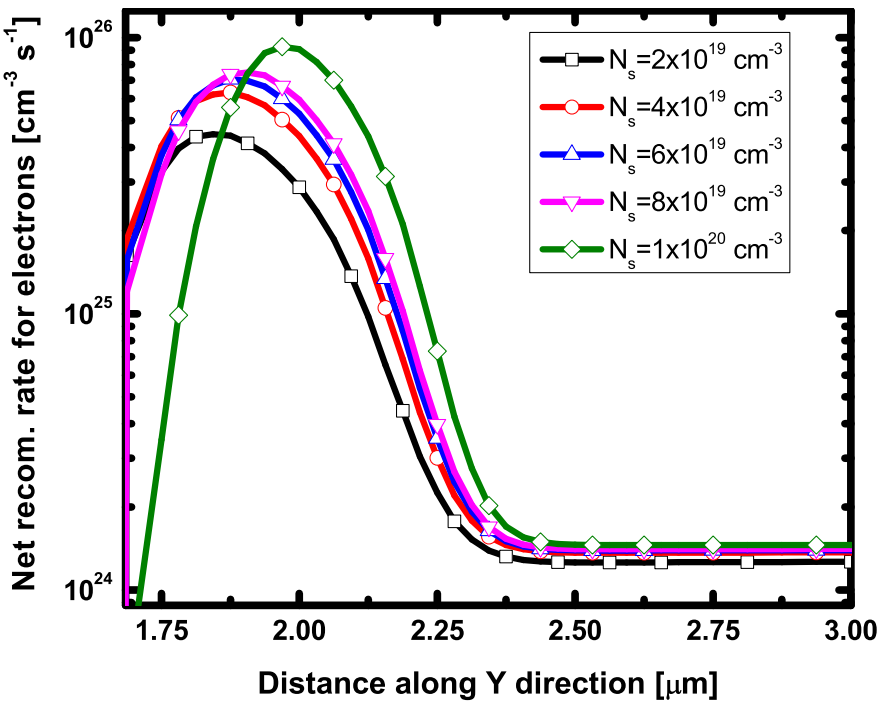

Figure 2.13: Net recombination rate for electrons as a function of depth (along y coordinate) from the surface of p^+ doping window with N_s as a parameter when the p-i-n waveguide is forward biased at 1 V.

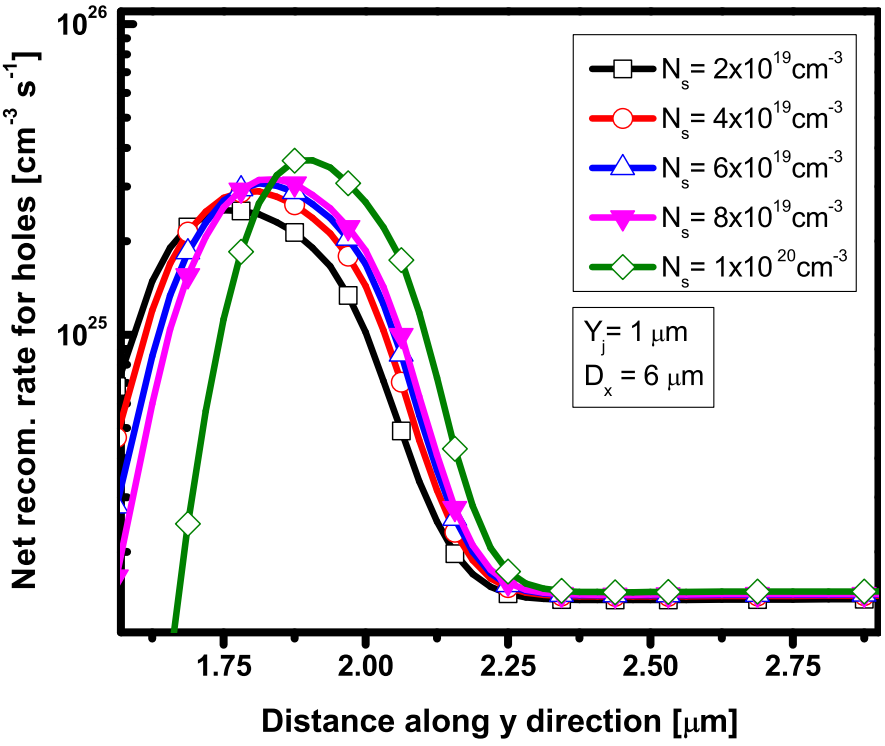

Figure 2.14: Net recombination rate for holes as a function of depth (along y coordinate) from the surface of n^+ doping window with N_s as a parameter when the p-i-n waveguide is forward biased at 1 V.

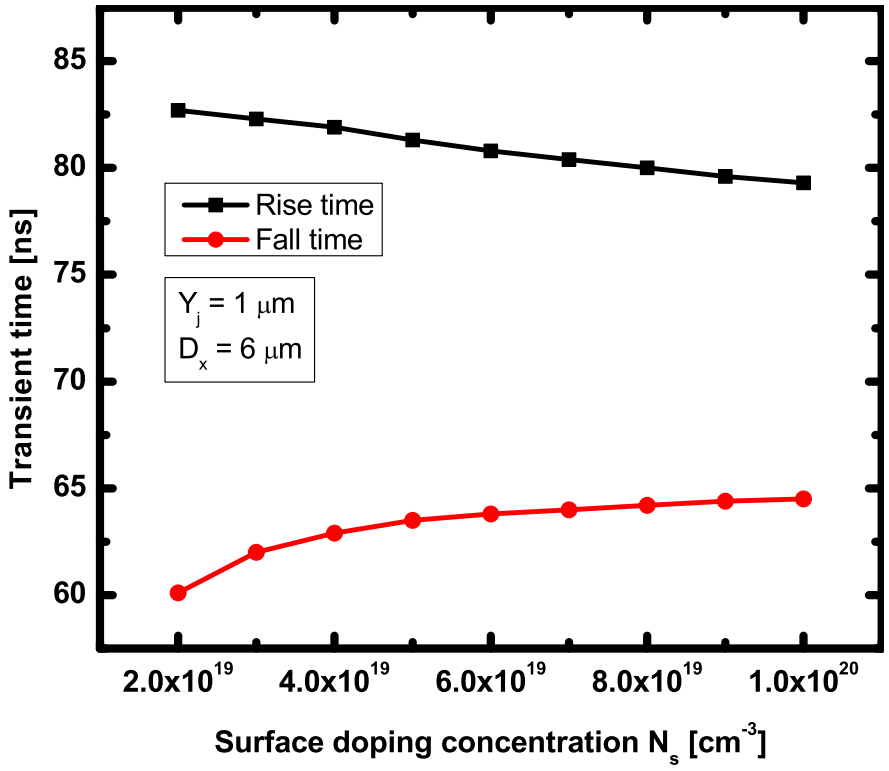

Figure 2.15: Rise and fall time as a function of surface doping concentration of diffusion window of the p-i-n waveguide upon applying a pulse of voltage ranging from 0.5 V to 1.5 V.

of 2 μs and period of 4 μs having an amplitude ranging from 0.5 V to 1.5 V. As shown in Fig. 2.15, the rise time is found to decrease but the fall time is found to increase slowly as the surface impurity concentration is increased. The increasing doping concentration increases both the depletion capacitance and the built in electric field. The former effect leads to the increment of RC delay but the later helps in faster removal of minority carries (this helps to reduce the fall time to some extent but the capacitive effect may be dominant) from those regions.

2.2.2 Optimized design

Having analyzed the effects of design parameters variation on the characteristics of p-i-n waveguide, we have chosen optimum values for final design as listed in Table. 2.2. The steady state voltage dependent electron and hole concentrations under the rib have been estimated to find the influence of forward voltage in changing the free carrier concentrations. The estimated results shown in Fig. 2.17 are indicating rapid

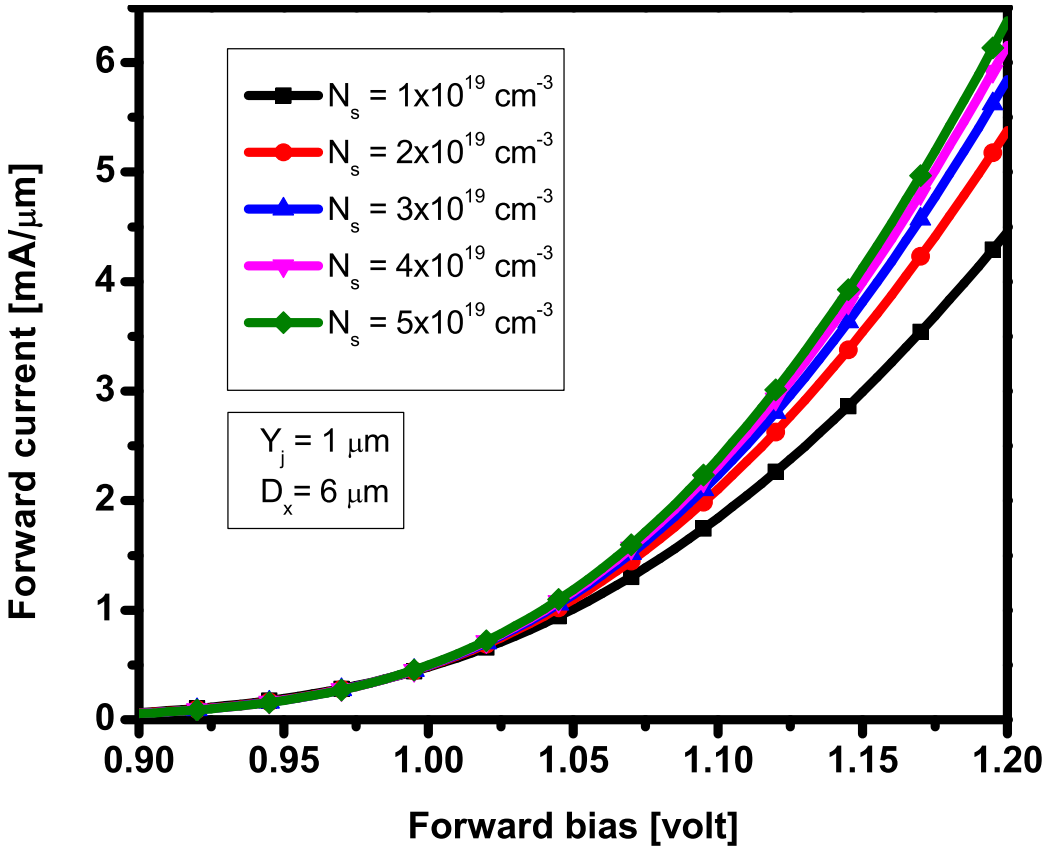

Figure 2.16: Steady state I-V characteristics of p-i-n waveguide with surface doping concentration N_s as a parameter.

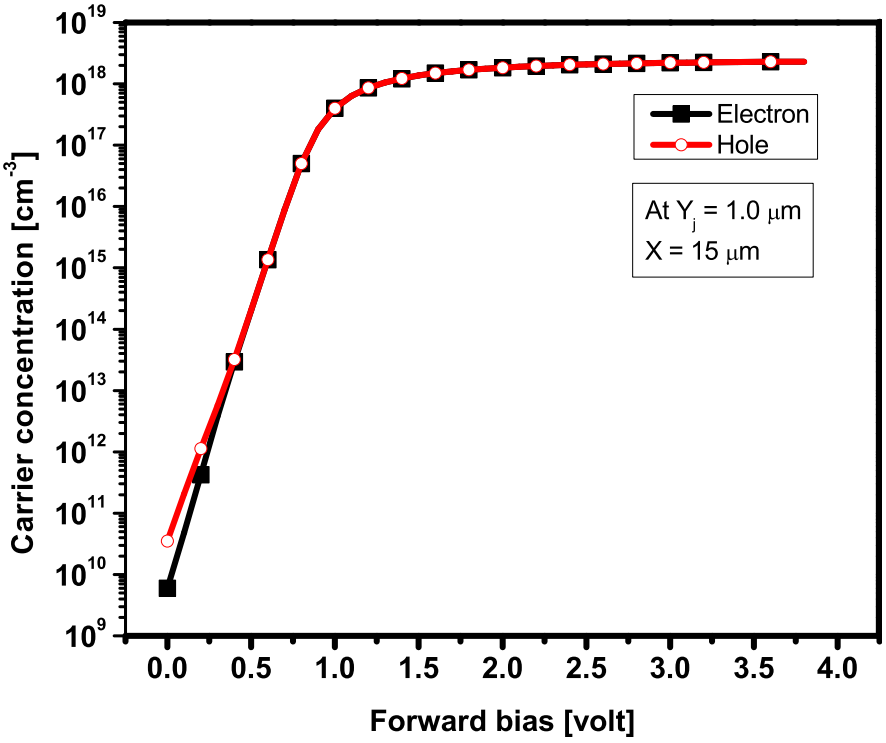

Figure 2.17: Electron and hole concentrations at the middle point of the guided TE mode of the p-i-n waveguide where electric field gets peak value (at a depth of 2.5 μm from the top surface of the rib of the p-i-n waveguide / VOA) as a function of forward bias voltage.

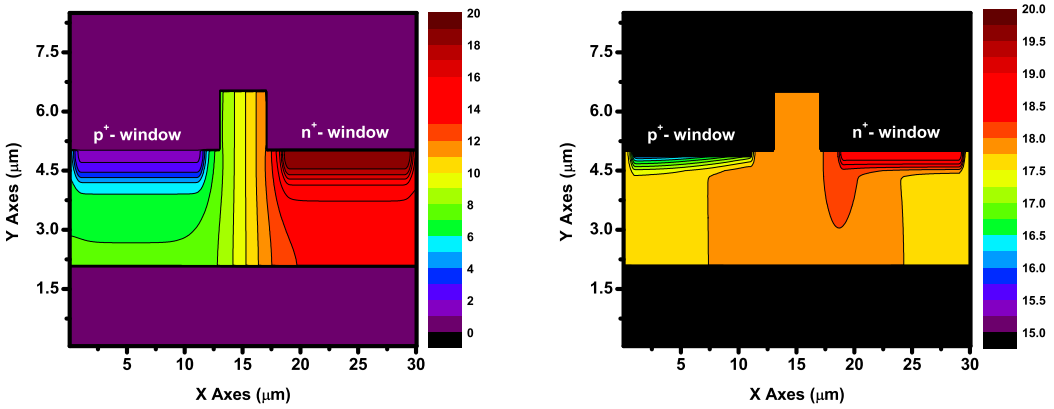

(a) (b)

Figure 2.18: 2D plot of logarithmic value of free electron concentrations for p-i-n waveguide (a) Under 0 V bias. (b) Under 1.3 V forward bias.

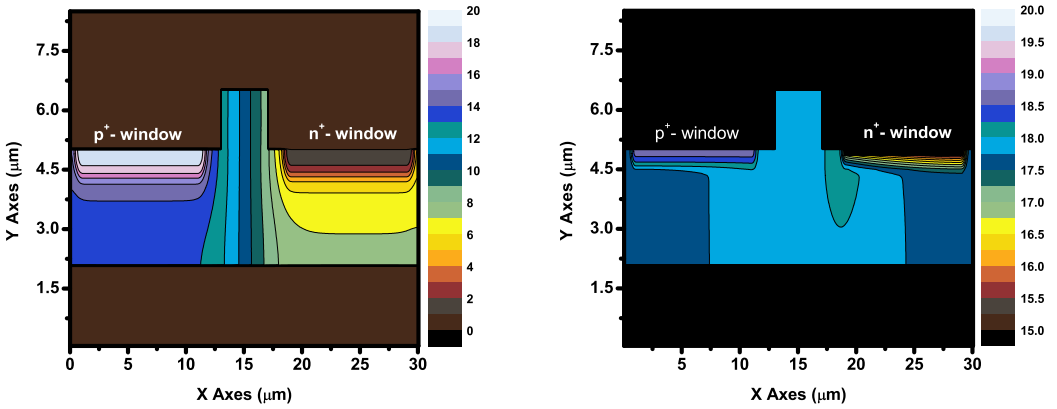

(a) (b)

Figure 2.19: 2D plot of logarithmic value of hole concentrations for p-i-n waveguide (a) Under 0 V bias. (b) Under 1.3 V forward bias.

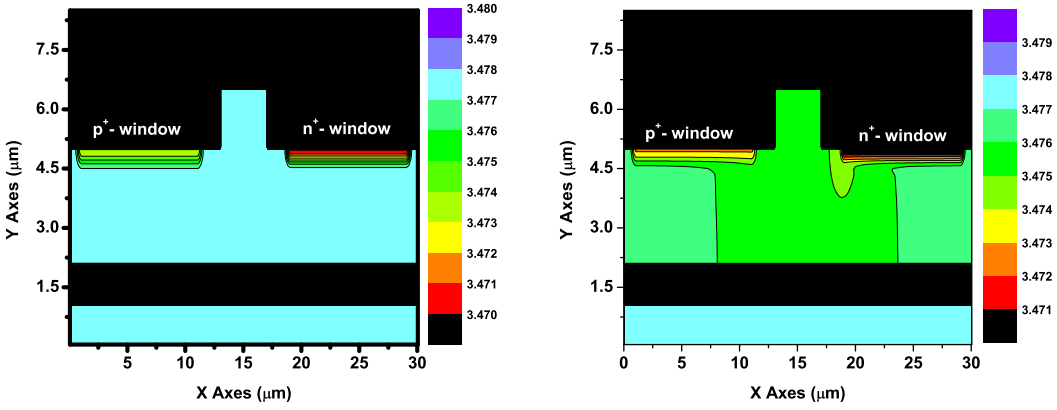

(a) (b)

Figure 2.20: Refractive index profiles of the of p-i-n waveguide (a) The refractive index is uniform everywhere except in the heavily doped regions for 0 V bias. (b) The refractive index has been changed from its equilibrium value due to carrier injection at 1.3 V forward bias.

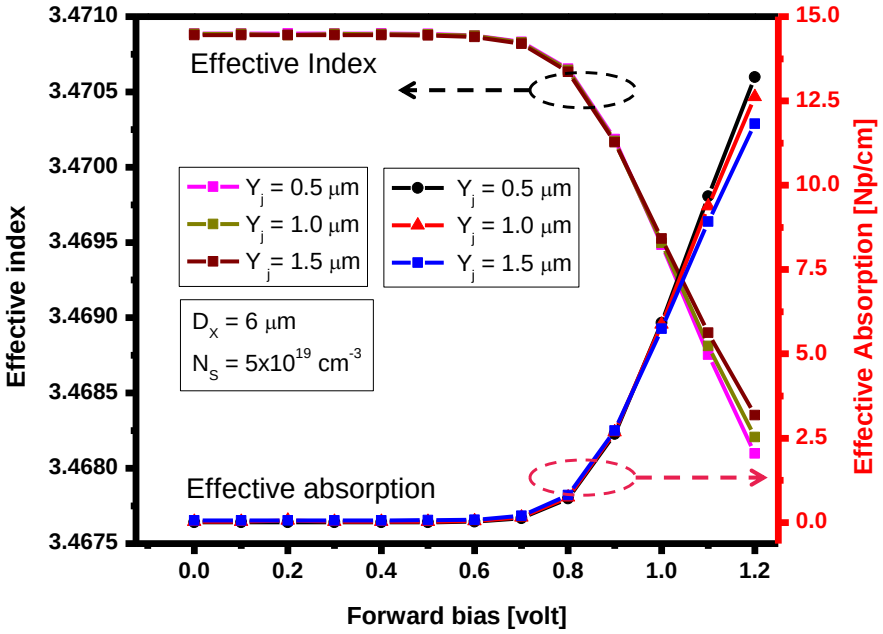

Figure 2.21: Effective index and absorption as a function of forward bias voltage of p-i-n waveguide with junction depth Y_j as a parameter under TE polarized light of wavelength around 1550 nm.

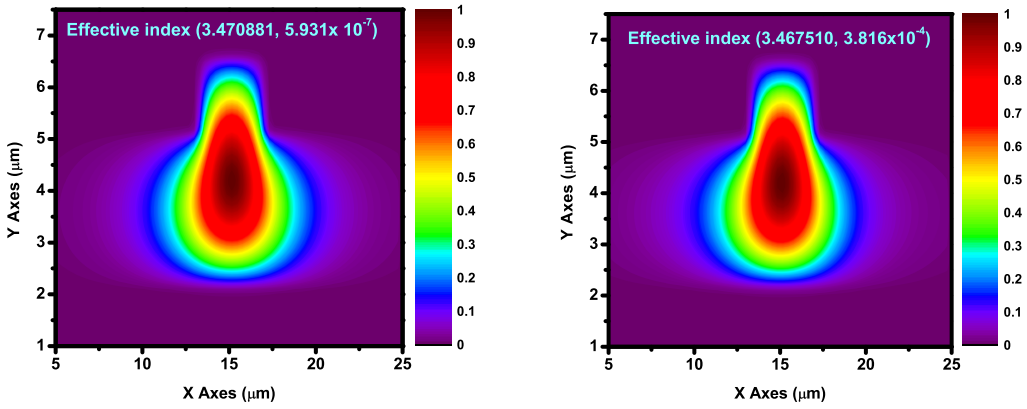

(a) (b)

Figure 2.22: Fundamental mode profiles of the p-i-n waveguide for TE polarized light of wavelength around λ = 1550 nm depicted with a complex effective index ($n_{eff} + jK_{eff}$). (a) The complex effective index, the effective width and the height of the guided mode are estimated to be (3.470881+j5.931$\times 10^{-7}$), ω_x = 5.20547 and ω_y = 3.32567 respectively under 0 V bias. (b) The complex effective index, the effective width and height of the guided mode are estimated to be (3.467510+j3.816$\times 10^{-4}$), ω_x = 5.13970 and ω_y = 3.33201 respectively under 1.3 V bias.

increase of free carrier concentration with voltage upto V = 1.3 V, beyond which the carrier concentrations tend to saturate due to the resistive nature rather than the diode nature of the device. Hence, we expect a small variation in the refractive index and absorption beyond V = 1.3 V (beyond the current of 130 mA). In order to find the change in the effective index and absorption due to carrier injection, the electron and hole concentration profiles for 0 V and 1.3 V biases have been found and which are shown in Fig. 2.18 and Fig. 2.19, respectively. Then the concentration profiles are used to estimate the absolute profiles for refractive index and absorption by using the equations (2.1), (2.3) and (2.2), (2.4) given below for 0 V and 1.3 V biases respectively. The refractive index profiles for 0 V and 1.3 V biases have been shown in Fig. 2.20. The Rsoft-FEMSim tool has been employed to find the effective values of refractive index and absorption coefficient and corresponding fundamental mode profiles of the of p-i-n waveguide for TE polarization are shown in Fig. 2.22 for both at 0 V and 1V biases. From the effective index verses forward bias voltage plot shown in Fig. 2.21, the expected change in effective index for a voltage change 0 to 1.3 V under TE polarized light is estimated to be Δn_{eff} = 3.37$\times 10^{-3}$ and corresponding interaction length of the of p-i-n waveguide for π phase shift of guided light as around 230 μm by using the equations (2.5) and (2.7) respectively.

Table 2.2: Optimized design parameters of the p-i-n waveguide.

Junction depth Y_J (μm)	Surface doping concentration N_S (cm^{-3})	Width of the diffusion window W_D (μm)	Spacing D_x (μm)
1	5$\times 10^{19}$	20	6

The real part of the refractive index at any point in the p-i-n waveguide at 0 V bias (n_0) is expressed as,

$$n_0 = 3.47772 - \{8.8 \times 10^{-22}\Delta N_{e0} + 8.5 \times 10^{-18}(\Delta N_{h0})^{0.8}\} \tag{2.1}$$

where 3.47772 is the refractive index of the bulk silicon (for SOI wafer we have used) at $\lambda \sim$ 1550 nm and before any diffusion is carried out. The real part of the

refractive index at any point in the p-i-n waveguide at 1.3 V bias ($n_{1.3}$) is expressed as,

$$n_{1.3} = 3.47772 - \{8.8 \times 10^{-22}\Delta N_{e1.3} + 8.5 \times 10^{-18}(\Delta N_{h1.3})^{0.8}\} \quad (2.2)$$

The absorption coefficient at any point in the p-i-n waveguide at 0 V bias (α_0) is expressed as,

$$\alpha_0 = \{8.5 \times 10^{-18}\Delta N_{e0} + 6.0 \times 10^{-18}\Delta N_{h0}\} \quad (2.3)$$

The absorption coefficient at any point in the p-i-n waveguide at 1.3 V bias ($\alpha_{1.3}$) is expressed as,

$$\alpha_{1.3} = \{8.5 \times 10^{-18}\Delta N_{e1.3} + 6.0 \times 10^{-18}\Delta N_{h1.3}\} \quad (2.4)$$

The change in real part of effective index due to the bias voltage change of 1.3 V ($\triangle n_{eff}$),

$$\triangle n_{eff} = n_{eff1.3} - n_{eff0} \quad (2.5)$$

The change in absorption coefficient due to the forward bias voltage change of 1.3 V ($\triangle \alpha_{eff}$),

$$\triangle \alpha_{eff} = \alpha_{eff1.3} - \alpha_{eff0} \quad (2.6)$$

The interaction length of p-i-n waveguide (L_π) to have π phase shift in the guided mode is expressed as,

$$L_\pi = \frac{\lambda}{2\Delta n_{eff}} \quad (2.7)$$

2.2.3 Variable Optical Attenuator (VOA)

The VOA has been designed by interfacing two straight waveguides of width W = 5.5 μm to the input and output sides of the p-i-n waveguide through two number of taper waveguides of length 250 μm as shown in Fig. 2.23. The interfacing waveguides have been used here for reducing the coupling loss when VOA is connected with single mode optical fibers.

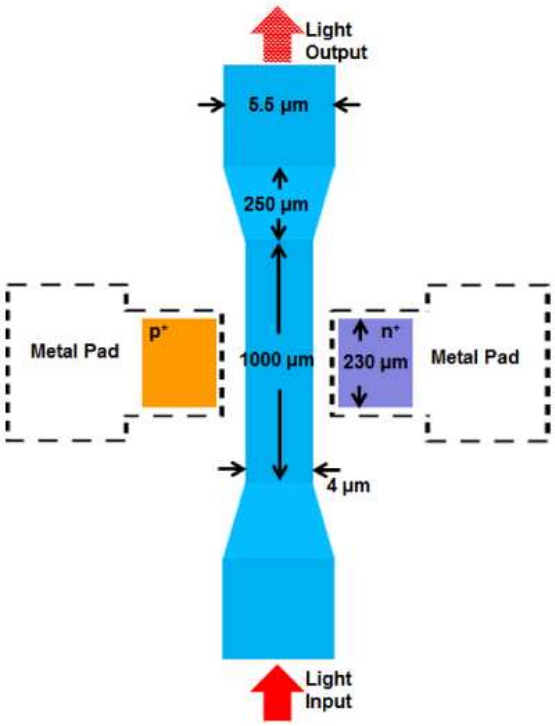

Figure 2.23: Schematic top view of the VOA showing the p^+ and n^+ doping windows, metal pads, taper waveguides and interfacing waveguides.

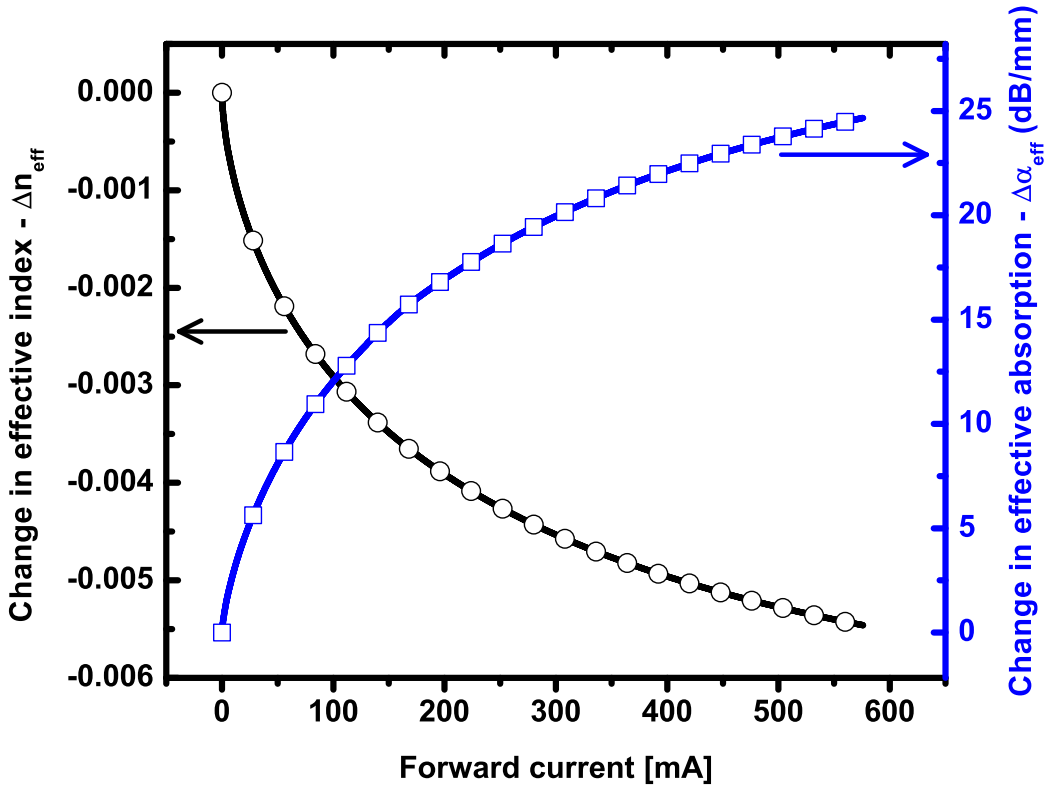

Figure 2.24: Change in effective index and effective absorption as a function of forward bias current to the p-i-n waveguide guiding TE polarized light of $\lambda \sim 1550$ nm.

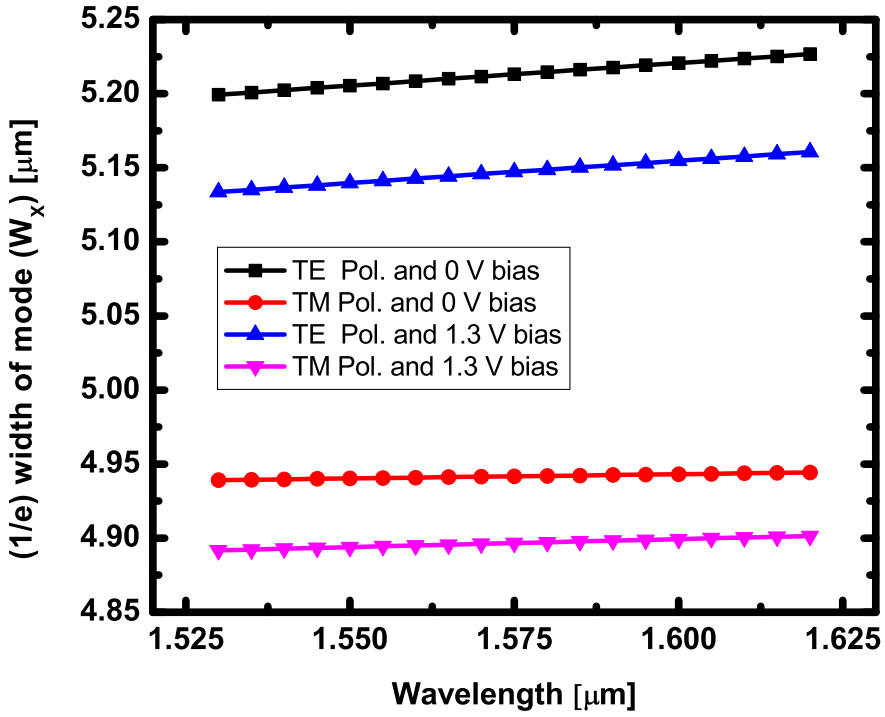

Figure 2.25: (1/e) width (ω_x) of fundamental mode as a function of wavelength ranging from 1530 nm to 1620 nm for TE and TM polarizations with 0 V and 1.3 V bias to the VOA. It is clear from the plot that the ω_x decreases when the VOA is forward bised at 1.3 V when compared to for 0 V.

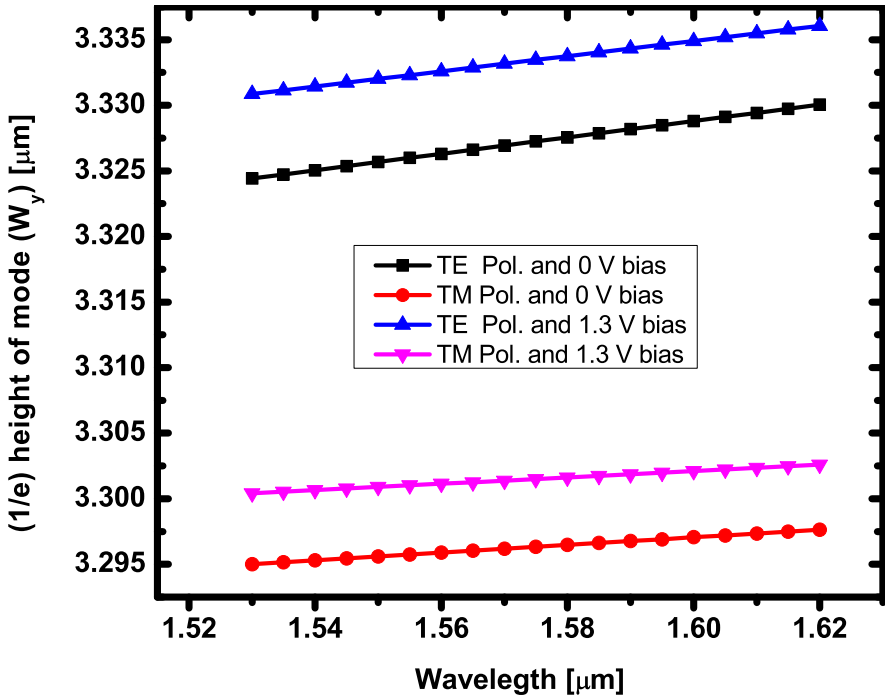

Figure 2.26: (1/e) height (ω_y) of fundamental mode as a function of wavelength ranging from 1530 nm to 1620 nm for TE and TM polarizations with 0 V and 1.3 V bias to the VOA. It is clear from the plot that the ω_y increases when the VOA is forward bised at 1.3 V when compared to for 0 V.

The attenuation characteristics of VOA for TE polarized light of wavelength around λ = 1550 nm have been estimated from Medici and Rsoft-FEMSim simulations. The effective absorption coefficient as a function of both forward voltage and forward current have been calculated by importing the complex refractive index profile and carrying out the FEMSim for effective index and effective absorption for the fundamental modes at different forward bias current and corresponding voltages. Fig. 2.24 shows the attenuation versus injected forward current of VOA exhibiting around 3.6 dB/mm of attenuation at 15 mA of injected current. At low injected current the VOA shows high change of attenuation but when current is increased the change of attenuation is found to decrease. In order to find the effect of carrier injection and variation in wavelengths on the confinement of the guided mode, Medici and FEMSim simulations have been carried out for 0 V and 1.3 V biases and for the wavelength range from 1520 to 1630 nm to find the effective mode width ω_x and mode height ω_y for the fundamental mode of TE and TM polarizations.

In general the effective index and the confinement of light of a single mode waveguide decreses as the wavelenth is increased. From Fig. 2.25 and 2.26 it is known that both ω_x and ω_y increase with increasing wavelength under both TE and TM polarizations. Also it is important to note from the figures, while comparing the mode sizes for 0 V and 1.3 V biases as the voltage is increased the confinement of light along lateral direction increases (ω_x decreases) but along the vertical direction it is decreased (ω_y increases). This increased lateral confinement of the mode is due to the reduction of effective index at the slab region by carrier injection. But the decreased vertical confinement of mode is due to the reduction of index contrast between core (rib region) and oxide cladding due to the injection of carriers.

2.2.4 Mach-Zehnder Interferometer (MZI)

Mach-Zehnder interferometer (MZI) is an optical device, which is used here to convert phase modulated optical signals into the intensity modulated signals. We have designed the MZI based on the multimode interference (MMI) couplers for its optical splitting and combining operations. Fig. 2.27(a) shows a schematic top view of the MZI, which

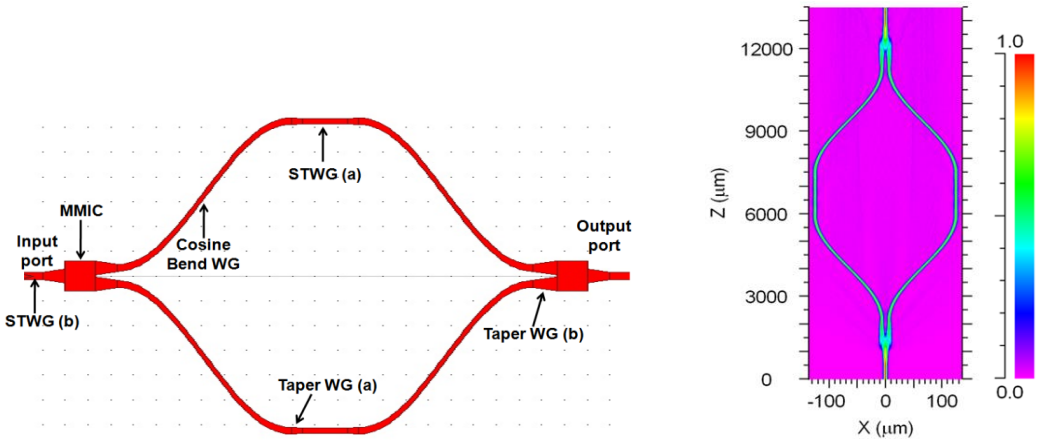

(a) (b)

Figure 2.27: (a) Schematic top view of MZI showing its various sections, (b) The Rsoft-BeamProp simulation shows guiding of light in the MZI with very low loss.

uses straight waveguides, bend waveguides, tapered waveguides and multimode interference (MMI) couplers.

1x2 MMI Coupler

The MMI coupler is basically a multimode waveguide with N inputs and M outputs (NxM MMI coupler), which is used extensively in integrated optics as it can perform many functions like splitting, combining, filtering and switching of optical signals. MMI devices operate based on the principle of self-imaging. The self imaging is a property of multimode waveguide by which an input field profile is reproduced as a single or multiple images at periodic intervals along the direction of propagation of light through it [51]. These structures offer several advantages over traditional waveguide structures, such as compact in size, low loss, low polarization and wavelength dependency and relaxed fabrication tolerances. We did not use Y splitter/ combiner structures for making MZI since, at the junction the leakage of power would not be the same due to the effective mode size inside the Y junction will be different for TE and TM polarization. However this would not be the case in the case of MMI, due to its fundamentally different character of power localization due to multimode interference phenomenon.

Buy the good rule of thumb, a low loss MMI based $1 \times$M coupler requires more than

M+1 suppoted eigen modes for achieving M number of highly resolved images. The design of our MZI requires two 1×2 MMI couplers; one for spliting at the input side and another for combining at the output side. The width of the MMI coupler W_{mmi} has been chosen such that it offers two number of highly resolved images of its input field profile.

For designing the 1×2 MMI coupler, a single mode rib waveguide (W = 5.5 μm, h = 3 μm and H = 4.5 μm) is connected at the center point of input side of sufficiently long multimode waveguide (MMI) of with W_{mmi} as shown in Fig. 2.28(a).

A fundamental mode with TE polarization of wavelength around 1550 nm is launched into the input single mode waveguide and it is allowed to propagate into the multimode waveguide for exciting multiple guided modes. In order to observe the expansion of single mode field into multiple modes in the MMI region and locallization of the fields, the X-Z field patterns of the complete structure is monitored while increasing W_{mmi} from 5.5 μm until two number of highly resolved images are formed at shortest distance from the interface between the two waveguides. It is found from the simulations that for W_{mmi} = 24 μm, at a distance of around 630 - 670 μm from the interface, two distinct images appear in the multimode waveguide as shown in Fig. 2.28(b). Then the length of the multimode waveguide L_{mmi} is shortened roughly to the point where two images appear, then two identical single mode waveguides with same dimensions as the input single mode waveguide are connected symmetrically at its output as shown in 2.29 (a) . In order to find the optimum position of the output waveguides, their power outputs are monitored while moving them away from each other from their close positions. Fig. 2.30 shows power at either output waveguides as a function of their positions from the center of multimode waveguide. From the simulation results it has been found that the optical power at the output waveguides get maximum when the position of them is at 6.5 μm.

In order to estimate the exact value of L_{mmi} which offer equal power splitting and highest throughput, BeamProp simulations are carried out while sweeping L_{mmi} from 630 to 700 μm and monitoring the power at the output waveguides. It is clear from Fig. 2.31 showing power at the two output waveguides get equally split and reach maximum for L_{mmi} = 650 μm.

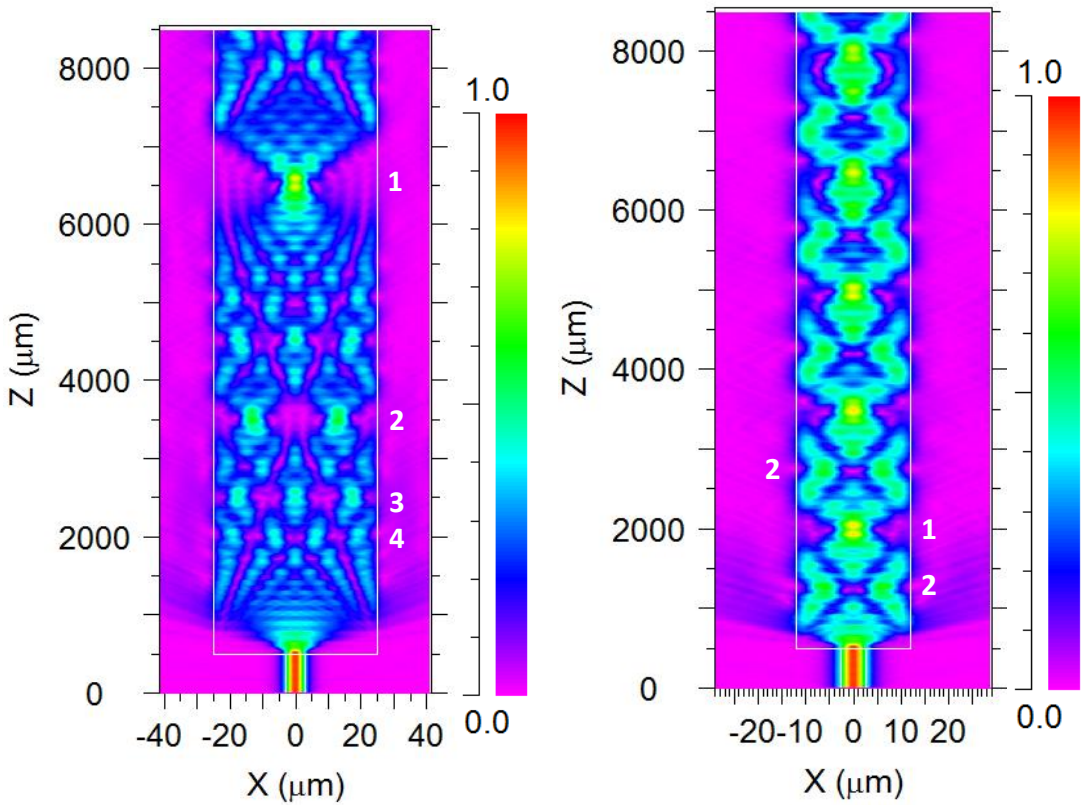

(a) (b)

Figure 2.28: X-Z view of electric field profile inside the MMI for TE polarized light at λ = 1550 nm. The numbers 1,2,3 etc. specify the number of resolved images; (a) For L_{mmi} = 8000 μm and W_{mmi} = 50 μm, two images appear at a distance of $\sim$3000 μm from the interface. (b) For L_{mmi} = 8000 μm and W_{mmi} = 24 μm, two number of highly resolved images appear at a distance of $\sim$ 650 μm from the interface. These two figures (a) and (b) indicate that as the W_{mmi} is increased then L_{mmi} also increases to get the same number of resolved images.

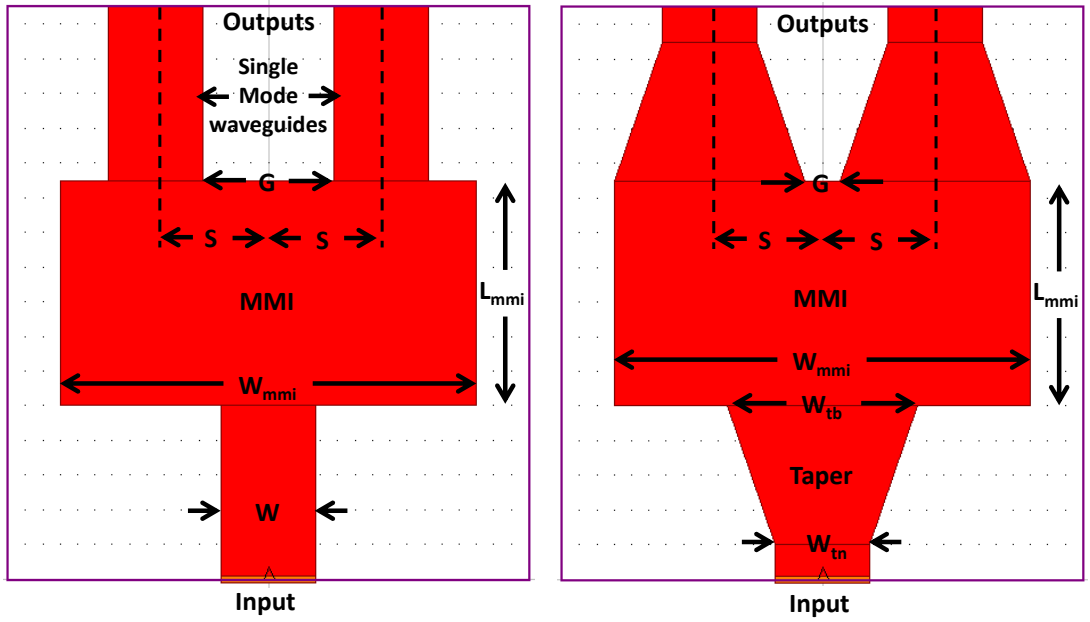

(a) (b)

Figure 2.29: Schematic top view of the 1x2 MMI couplers used for design optimization in Rsoft-BeamProp simulation tool: (a) Structure used for optimizing the position of the output waveguides, (b) Structure used for optimizing the width of the output and input tapers. Where W_{mmi} and L_{mmi} are width and length of the MMI region, W_{tn} and W_{tb} are width of the taper waveguides at narrow and broader sides, G is the gap between the inner edges of the output taper waveguides and $2S$ is the separation between the output taper waveguides.

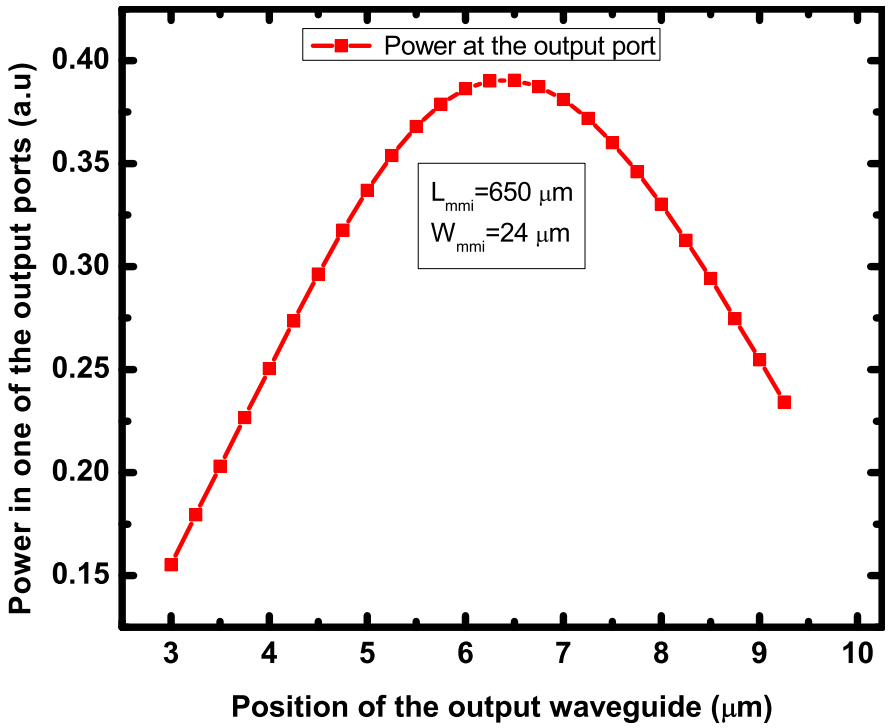

Figure 2.30: Optical power at either of the two output ports of the MMI based 1x2 power splitter as a function of their position from the center of x coordinate. It is clear from the plot that when the position gets 6.5 μm from the center the output power reach maximum value.

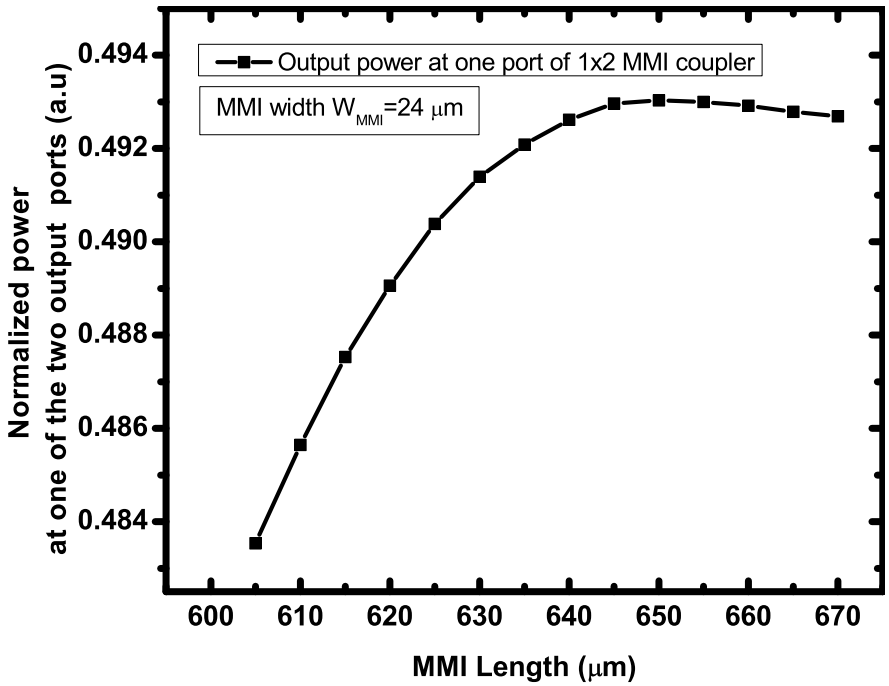

Figure 2.31: Finding optimum MMI length for the 1x2 power splitter having the MMI width (W_{mmi}) of 24 μm. The figure shows that the maximum of 49.3 $\%$ of input optical power is dropped at one of the output port of the device when the MMI length (L_{mmi}) becomes 650 μm.

In order to minimize the optical losses which occur at junctions, single mode waveguides are attached with the multimode waveguide through adiabatically tapered waveguides of legth L_t having width variation from W_{td} (at broader side) to W_{tn} (at narrow side) as shown in Fig. 2.29(b). For optimizing the value of W_{td}, W_{tn} is fixed at 5.5 μm and W_{tb} is varied from 5.5 to 13 μm for all the three taper waveguides which are at the input and output sides of MMI coupler while monitoring the power from the output taper waveguides. As we see from Fig. 2.32 that the output power at either of the taper waveguides keep on increasing with W_{tb}. However, due to the limitations of photolithographic technology in the lab and for avoiding lateral extension of output taper waveguides beyond the boundaries, we have chosen W_{tb} to be 11 μm in such a way that the spacing between the closer edges of the output taper waveguides to be G = 2 μm.

Fig. 2.31 shows that for L_{mmi} = 650 μm power at either of the output ports get maximum. The single mode waveguide of width W = 5.5 μm is connected at the middle point of MMI through a tapering waveguide and two bend waveguides of radii R = 25000 μm and widths W = 5.5 μm are attached at the outputs through two tapering waveguides. The Rsoft-BeamProp simulation of 1x2 MMI coupler with bend waveguides at the output shows the power throughput of $\sim$ 99 $\%$.

The MZI based on MMI coupler has been designed by connecting two 1x2 MMI optical couplers in back to back configuration through two straight waveguides of width W = 4 μm and interfacing taper waveguides (Taper waveguide(a)) of length L_t = 250 μm. This MZI design results in a throughput power of 98 $\%$.

The dimensions of various sections of MZI are (1) straight waveguide(a); rib height = 4.5 μm, rib width = 4 μm, slab height = 3 μm. top oxide cladding thickness = 1 μm (2) straight waveguide(b); rib height = 4.5 μm, rib width = 5.5 μm, slab height = 3 μm and top oxide cladding thickness = 1 μm (3) taper waveguide(a); tapering length = 250 μm and width variation = 4 to 5.5 μm. (4) taper waveguide(b); tapering length = 500 μm and width variation = 5.5 to 11 μm. (5) multimode interference coupler; MMI width = 24 μm and MMI length = 650 μm. (6) bend waveguide; bending radius = 25000 μm, width = 5.5 μm and (7) separation between the MZI arm is 250 μm.

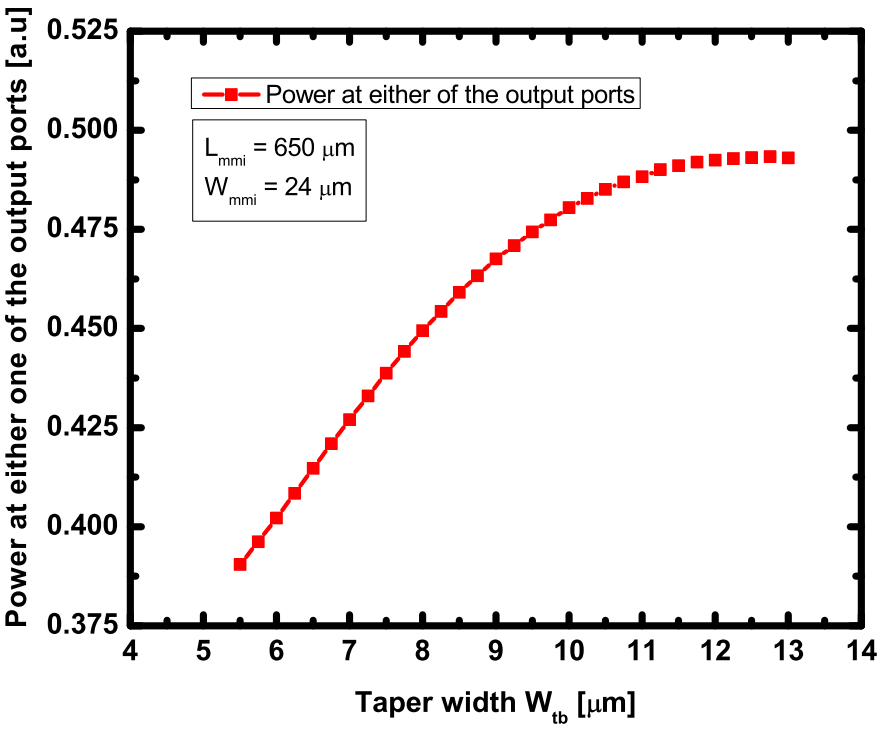

Figure 2.32: Optical power output as a function of width of the taper waveguide used in both output and input sides of 1x2 MMI power splitter for TE polarized light at λ = 1550 nm.

2.3 Mach-Zehnder Modulator (MZM)

The MZM has been designed by incorporating a p-i-n waveguide at one of the parallel of arms of MZI shown in Fig. 2.33. This p-i-n waveguide operates as a phase modulator when it is driven by an electrical signal. When the light is coupled to the input port of the MZM, it is equally split and guided as fundamental mode through respective arms. The light which is guided through the p-i-n waveguide is phase modulated and attenuated in accordance with the electrical signal applied to it and then it is guided to the combiner section of the MZI. The light which is being guided by the another arm (so called reference arm) acquires a phase shift only due to the path which has traveled. These two modes are allowed to interfere at the combiner of MZI to produce the optical interference pattern at the output port of MZM in accordance to their phase relationships. Let the intensity of the electric field at the input port of the MZM be E_{in} then E_{ref} and E_{mod} be the intensity at reference and modulator arms of MZM respectively. According to the law of conservation of energy it can be written as,

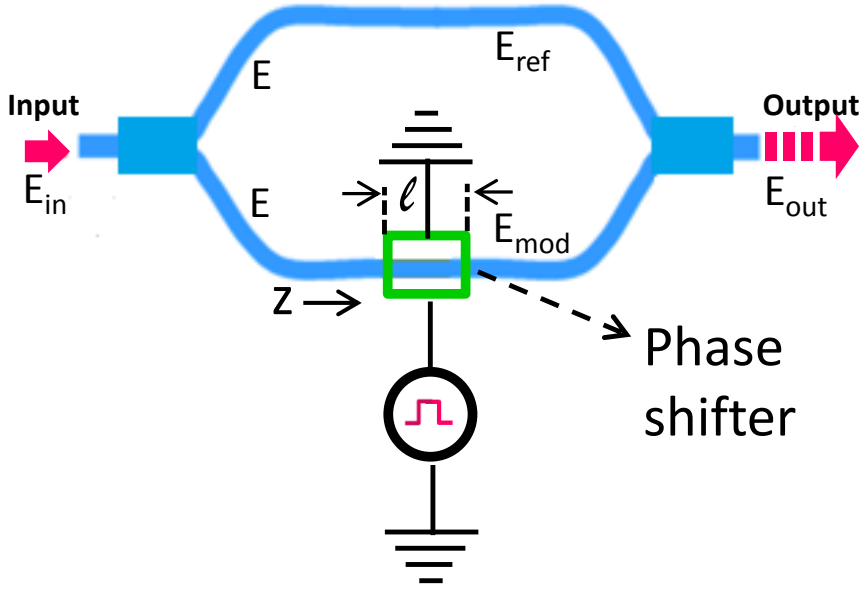

Figure 2.33: Schematic view of the Mach-Zehder modulator (MZM) showing electric field at various positions

hence the electric field at the input,

$$E_{in} = E_p e^{j\omega t} \tag{2.8}$$

$$E = \frac{E_{in}}{\sqrt{2}} \tag{2.9}$$

Let E_p be the peak electric field at the input port, α and $\alpha+\Delta\alpha$, β and $\beta+\Delta\beta$ be the attenution, phaseshift constants of reference and modulating arms of MZM respectively. The electric field at any point along the reference arm (E_{ref}) may be written as,

$$E_{ref} = \frac{E_p}{\sqrt{2}} e^{(-\alpha+j\beta)z+j\omega t} \tag{2.10}$$

the electric field for the modulating (E_{mod}) arm (at any point beyond the p-i-n waveguide) is written as,

$$E_{mod} = \frac{E_p}{\sqrt{2}} e^{(-\alpha+j\beta)z+(-\Delta\alpha+j\Delta\beta)l+j\omega t} \tag{2.11}$$

where l is the length of the p-i-n diode / waveguide. The total electric field at the output of the MZM is the sum of electric field from the reference and modulator arms.

$$E_{out} = E_{ref} + E_{mod} \tag{2.12}$$

$$E_{out} = E_{ref}\{1 + e^{(-\Delta\alpha + j\Delta\beta)l}\} \tag{2.13}$$

Assuming adiabatic transition among the different waveguide structures of the MZI, the intensity of light at the output port (S_{out}) of MZM can be written as,

$$S_{out} = E_{out}E_{out}^{*} \tag{2.14}$$

$$S_{out} = E_{ref}E_{ref}^{*}\{1 + e^{(-\Delta\alpha + j\Delta\beta)l}\}\{1 + e^{(-\Delta\alpha - j\Delta\beta)l}\} \tag{2.15}$$

$$S_{out} = \frac{|E_p|^2}{2}\{1 + e^{(-\Delta\alpha - j\Delta\beta)l} + e^{(-\Delta\alpha + j\Delta\beta)l} + e^{-2\Delta\alpha l}\} \tag{2.16}$$

$$S_{out} = |E_p|^2\{cosh(\Delta\alpha l) + cos(\Delta\beta l)\}e^{(-2\alpha Z - \Delta\alpha l)} \tag{2.17}$$

where Z is the total length of the either arms of the MZM.

$$\frac{S_{out}}{S_{in}} = \{cosh(\Delta\alpha l) + cos(\Delta\beta l)\}e^{(-2\alpha Z - \Delta\alpha l)} \tag{2.18}$$

Equation (2.18) implies that the the intensity of light at the output port of the MZM is proportional to the sum of cosine function of the phase-shift constant ($\Delta\beta$) and cosine hyperbolic function of the absorption ($\Delta\alpha$) which in turn caused by the injection or depeletion of free carriers in the p-i-n waveguide as given equations (1.3) and (1.4) respectively. Also, this function is modulated by the exponentially decaying function of sum of the absorption due to plasma dispersion in p-i-n waveguide and passive waveg-

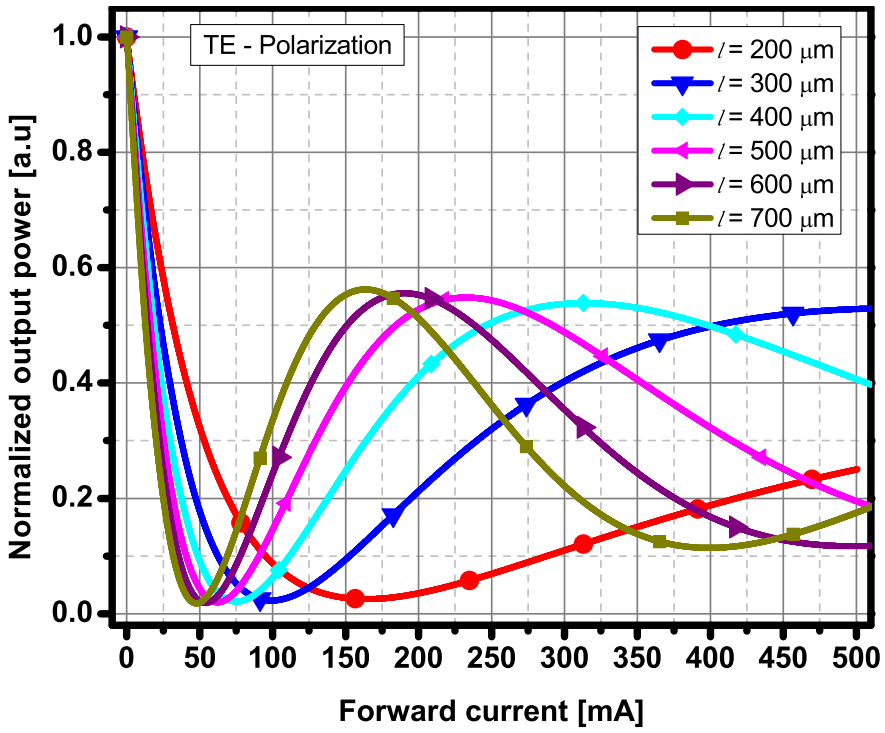

Figure 2.34: Simulated optical output power as a function of forward current with the length (l) of the p-i-n waveguide that is integrated with one of the arms of the MZI for TE polarized light input of λ = 1550 nm.

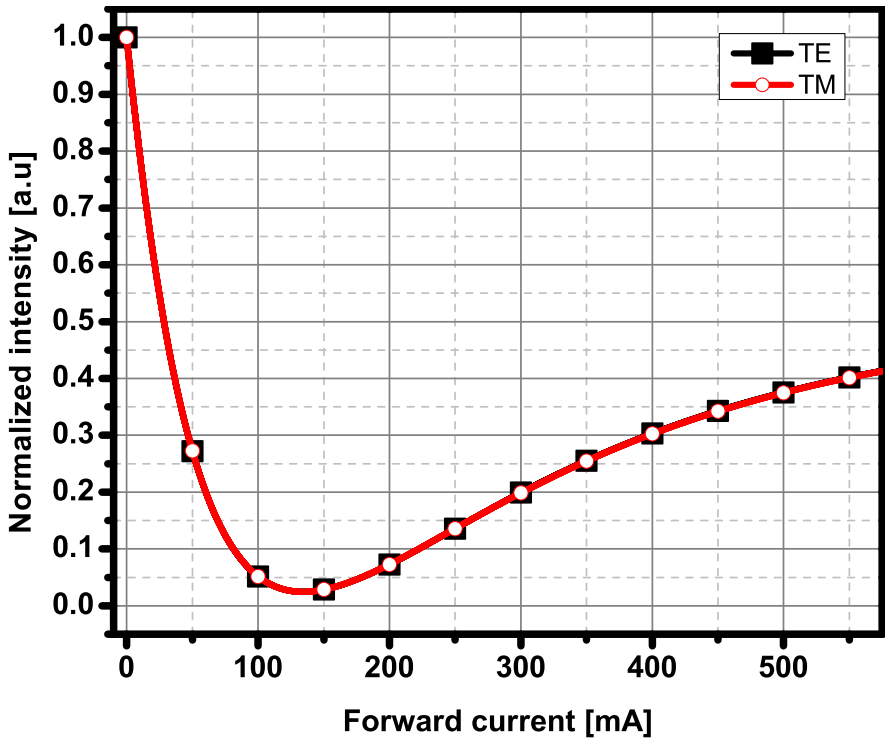

Figure 2.35: Simulated optical output power of MZM as a function of forward current of the p-i-n waveguide of length L = 230 μm for TE and TM polarization at λ = 1550 nm.

uide arm. It is also noted that, for the attenuation due to the passive waveguide to be minimum, the overall length of MZI is expected to be as small as possible. The intensity of the light for TE and TM polarization have been estimated by using the above equation and is shown in Fig. 2.35. The estimated extinction for both TE and TE polarization are obtained to be 16 dB.

2.4 Conclusions

The single mode SOI rib waveguide with an uniform layer of silicon dioxide on its surfaces has been designed to satisfy the requirement of higher confinement and low carrier transit time. The range of waveguide dimensions which ensure single mode guiding and wavelength dependency on mode sizes, effective index have been estimated by using finite element method of simulations. The designed SOI waveguide with optimum dimension has been converted into a p-i-n waveguide by introducing p and n type doping windows on left and right sides of rib. The profile has been assumed as the full Gaussian and the effect of variations in diffusion profile parameter such as junction depth, surface doping concentration, the distance between the closer edges of doping on electrical characteristics such as recombination rate of free carriers, rise time and fall time, then optical characteristics such as effective absorption and effective index of p-i-n waveguide have been studied. For the final design, a set of optimum values for the diffusion profile parameters have been selected from that the bias dependent attenuation, and effective index characteristics of p-i-n waveguide/VOA have been estimated. Since the intensity modulation of light requires an interferometer for converting the phase modulated optical signal into the easily observable intensity variations. A Mach-Zehnder interferometer based on 1x2 MMI coupler has been designed. The multimode interference based couplers have been chosen because of its superiority in less wavelength and polarization dependent operations, compactness, low loss and tolerance to variations in dimensions due to errors in fabrication. Finally the p-i-n waveguide has been integrated with the suitably designed MZI to make the Mach-Zender modulator. The phase and modulation depth characteristics of the designed MZM has also been studied.

CHAPTER 3

Process Optimization and Device Fabrication

In this chapter, process optimizations and fabrication of single-mode p-i-n waveguide structures and other integrated optical components like 1x2 MMI based optical power splitters, MZIs, etc. in 5 μm SOI substrate (see also Table 3.1) have been discussed.

3.1 Mask Design and Fabrication

After designing the devices viz., straight waveguides, bend waveguides, variable optical attenuators (VOAs), 1x2 optical power splitters, Mach-Zehnder interferometers (MZIs) and Mach-Zehnder modulators (MZMs), the first step in fabrication process flow is the design of layouts for photo masks. However, some of the actual dimensions of the designed device structures are slightly altered during the design of the mask layout. The reasons for this alteration and the effects of variations in the device dimensions will be discussed.

All the above mentioned device structures have been designed with oxide upper claddings of thickness $\sim$ 1 μm. However, during thermal oxidation of SOI samples, some amount of silicon will be consumed. The consumption of silicon during the oxidation of <100> silicon crystal is found to be around 44 $\%$ of the total thickness of the grown silicon dioxide. Therefore, the lateral dimensions of the layout for optical guiding structures had to be increased by 0.5 μm in all directions to compensate for the shrinkage of waveguide dimensions due to oxidation. The mask design includes passive reference devices e.g. straight waveguides, bend waveguides, 1x2 optical power splitters, MZIs and active devices like MZMs and VOAs (see Fig. 3.1). These additional reference structures would be used to estimate the characteristics of various sections of VOA and MZM.

Fabrication of complete VOA and MZM requires totally six lithographic steps. The mask layouts which are shown in Fig. 3.2 contains the patterns: 1. optical guiding

Table 3.1: Specifications of the SOI wafer

S.No.	Specifications	Value	Reason
1	Crystal orientation	<100>	Si wafer with <100> orientation has lowest interface state density at $Si-SiO_2$ interface
2	Doping	p-type (boron doped)	Absorption of light by holes is less than electrons at $\lambda \sim$ 1550 nm
3	Resistivity	> 5000 Ω-cm	Higher the resistivity lower the absorption loss due to free carriers
4	Crystal growth method	Float zone	To reduce the inclusion of carbon and oxygen impurities during the crystal growth
5	Device layer thickness	5 μm	To fabricate large cross-section single mode waveguide
6	BOX layer thickness	1 μm	This thickness is larger than the evanescent tail length of the guided single mode
7	Handle wafer thickness	500 μm	For good mechanical strength and easy handling

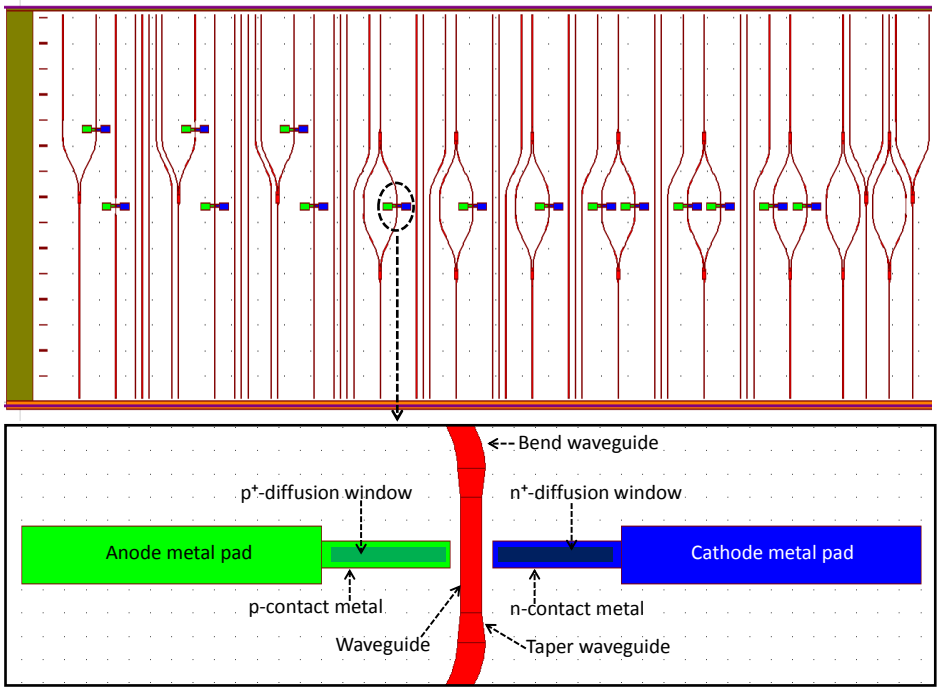

Figure 3.1: Complete mask layout which includes all the passive integrated optical guiding structures such as straight and bend waveguides, 1x2 optical power splitters, MZIs and active structures such as VOAs and MZMs in single windowpane. (Note: picture not to scale).

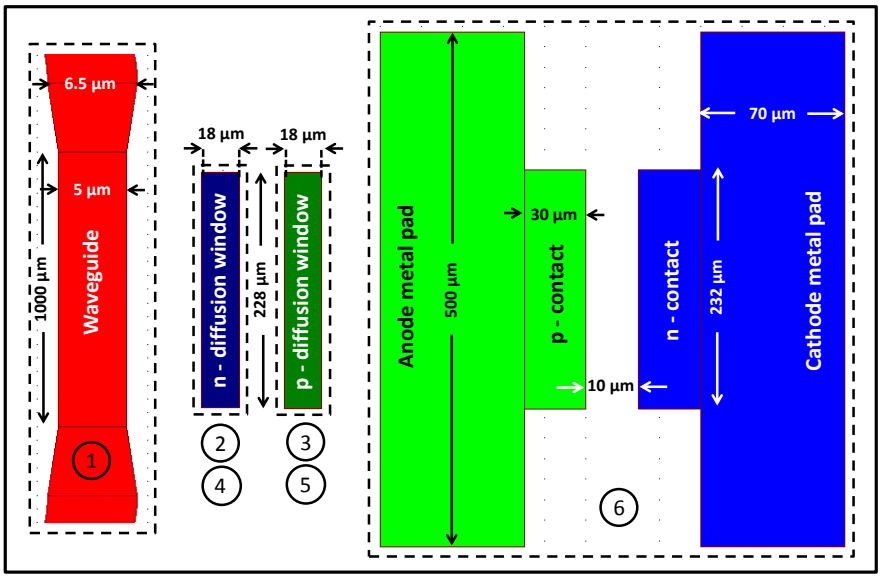

Figure 3.2: Schematic top view of mask layouts which consist of four out of six individual layouts: 1. optical guiding structures, 2. n^+ - diffusion windows, 3. p^+ - diffusion windows, 4^{th} and 5^{th} would be similar to n^+ and p^+ - diffusion masks whose dimension have been shrinked by 1 μm in all directions and they are not shown this figure and 6. metal contacts and pads.

structures, 2. n^+ - diffusion windows, 3. p^+ - diffusion windows, 4. n^+ - diffusion windows shrunk by 1 μm in all directions, 5. p^+ - diffusion windows shrunk by 1 μm in all directions and 6. metal contacts and pads.

Each mask layout file and a fresh photomask plate which had been coated with chromium and positive photoresist were loaded into a computerized UV mask writing system. The patterns were written with a focused UV laser beam of wavelength around 442 nm on the photoresist layer of the mask plate by using the automated laser encoder and writing head of mask writing system (DWL-66, Heidelberg instruments). The mask plates were then developed with photoresist developer and Cr etching solutions.

3.2 Sample Preparation

Prior to processing of the samples, a set of cleaning procedure is followed to remove the particles, contaminants, trace level organic and inorganic impurities, some unwanted native films, and films that have been deposited during previous processing on the samples. The selection of particular cleaning procedure varies among various process steps. The details of individual cleaning steps have been explained in the appendix.

Fresh SOI wafers of specifications given in Table 3.1 were diced into rectangular pieces of required dimensions (2cm x 3cm), then cleaned with trichloroehylene (TCE) followed by acetone and thoroughly rinsed in de-ionized (DI) water. The residual DI water on the surface of the sample was dried using N_2 air gun. The chemical oxidation of sample surface was carried out by immersing it in HNO_3 and heating at 70 °C for 5 minutes. A very thin oxide layer which had been formed over the sample's during the oxidation were etched away by soaking it in diluted HF solution (10:1::DI-H_2O:$\%$ HF) for 30 seconds, thoroughly rinsing in DI water and dried using N_2 air gun. The water traces residing on the samples were removed by baking the samples at 120 °C for 10 minutes in an oven and then cooled down to room temperature.

3.3 Fabrication of Optical Waveguide Structures

An uniform layer of positive photoresist (PPR) of thickness $\sim$ 1 μm was spin coated over the top surface of the SOI samples and then soft baked at 80 °C for 17 minutes in the oven. The sample were subjected to UV exposure ('i' line of mercury vapor lamp spectrum having wavelength $\sim$ 365 nm) through the first mask shown in Fig. 3.3 for 12 seconds by using MA6/BA6 mask aligner. The photoresist patterns were developed on the surface of the samples using the developer solution, samples were rinsed in DI water then dried in N_2 air. The photoresist patterns on the wafer surfaces were hardened by baking them at 120 °C for 40 minutes in the oven.

Reactive ion etching (RIE)

The sample were loaded into the RIE chamber and etch patterns were created on them by using the fluorine based plasma chemistry (SF_6:CHF_3:O_2::25:15:10 sccm, RF power: 150 W, pressure: 50 mTorr and temperature: 10 °C) to result in an etch depth of $\sim$ 1.5 μm then unloaded from the chamber. The photoresist mask on the samples surface were completely stripped off by using piranha solution (H_2SO_4:H_2O_2 (50 $\%$)::3:1), thoroughly rinsed in DI water and dried using N_2 air gun. The microscopic top view of the fabricated sample is shown in Fig. 3.4.

3.4 Thermal oxidation

After fabricating the waveguiding structures, the samples were cleaned with piranha solution, soaked in 10 $\%$ HF solution for 30 seconds, rinsed in running DI water and dried in N_2 air. Then they were subjected to RCA1 and RCA2 cleaning, thoroughly rinsed in DI water, soaked in 10 $\%$ HF solution for 30 seconds, again rinsed in DI water and dried using N_2 air gun.

A tsuprem4 simulation was carried out to optimize the thermal oxidation process parameters that would result in oxide mask layer of thickness around 0.67 μm for phosphorus diffusion. The dry-wet-dry mode of thermal oxidation procedure was fol-

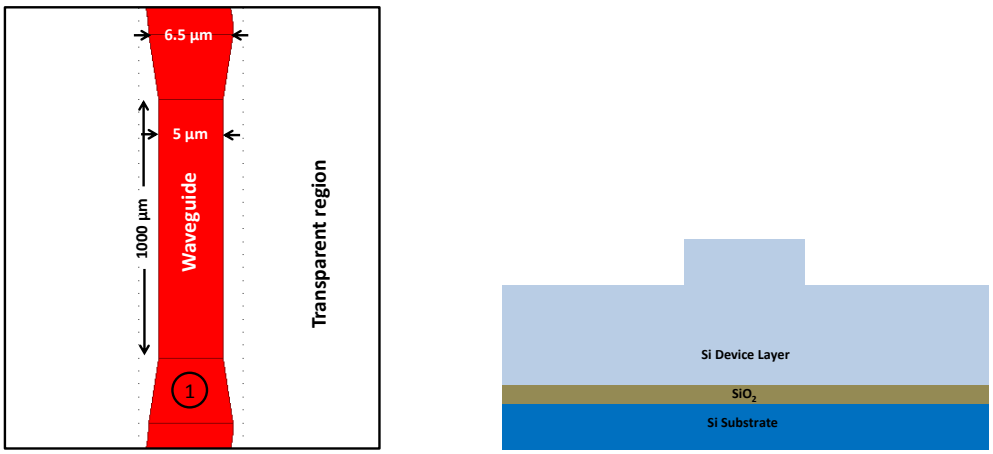

(a) (b)

Figure 3.3: First photolithography and RIE; (a) Top view of first mask layout showing a section of MZM which consist of an optical waveguide in is arm. (d) The cross section view of the SOI sample after first photolithography and reactive ion etching followed by photoresist stripping.

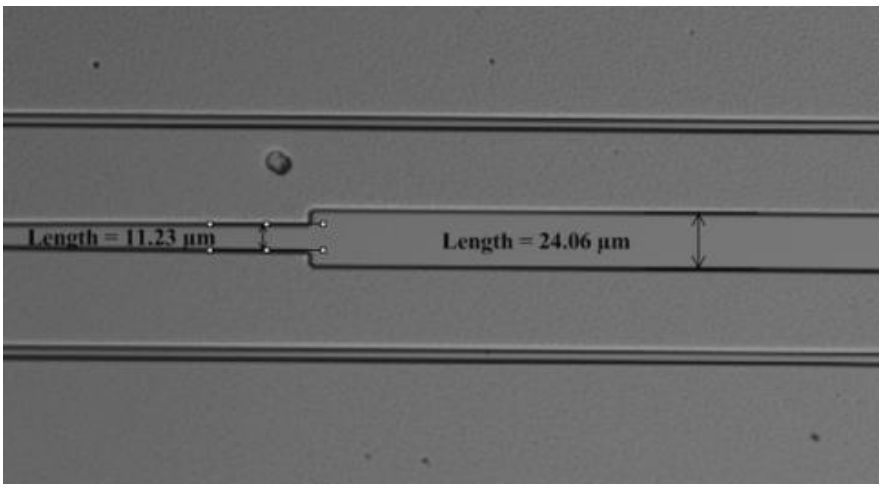

Figure 3.4: Microscopic top view of the sample after reactive ion etching and resist stripping. The figure shows MMI region of MZI, and waveguides.

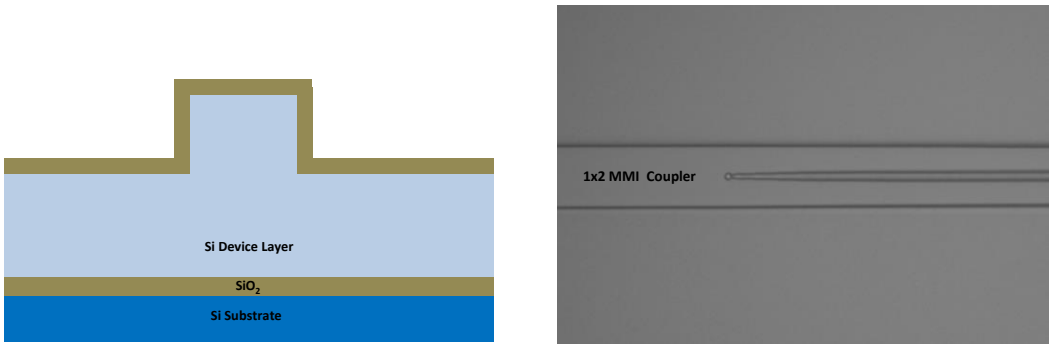

(a) (b)

Figure 3.5: (a) Schematic cross section of the sample after oxidation (b) Microscopic top view of the oxidized sample showing a section of 1x2 MMI coupler.

lowed for growing the masking oxide over the samples containing optical guiding structures. First, the samples were placed in a quartz boat and slowly loaded (at the rate 10 cm/min.) into the quartz furnace maintained at 1000 °C in N_2 ambient. The dry oxidation of the samples were carried out for 30 minutes in dry O_2 ambient, made by flowing O_2 at the rate of 150 l/h inside the quartz furnace. Second, the dry oxidation was stopped and wet oxidation was carried out for 135 minutes by supplying the O_2 through a water bubbling chamber maintained at 95 °C. Third, the wet oxidation was stopped and dry oxidation was carried out for 30 minutes as we have mentioned it previously. Finally, the samples were annealed in full N_2 ambient at 1000 °C for 15 minutes and slowly unloaded (at the rate 10 cm/min) from the furnace. This oxidation process had resulted in a layer of SiO_2 of thickness around $\sim$ 0.67 μm over the samples as predicted by the Tsuprem4 simulation. The schematic cross section view and microscopic image of the oxidized sample are shown in Fig. 3.5.

The oxidized samples were cleaned with piranha solution, rinsed thoroughly in DI water and dried using N_2 air gun, soaked in 5 $\%$ HF solution for 5 seconds, rinsed in running DI water and dried using N_2 air gun. The water traces on the samples were evaporated by heating them at 120 °C for 30 minutes in the oven then cooled down to room temperature.

The second photolithography was carried out to transfer the patters of the second mask which consists of n^+ - diffusion widow. The oxide regions of the sample, which

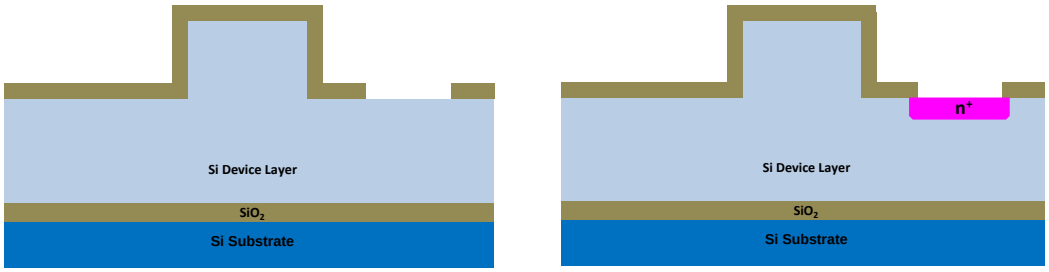

(a) (b)

Figure 3.6: Schematic cross section view of the sample: (a) after second photolithgraphy and patterning of masking silicon dioxide, (b) after phosphorus diffusion.

have not been covered by the hardened resists were etched away as shown in Fig. 3.6(a) by using buffered hydrofluoric (BHF) acid solution to delineate the windows for phosphorous diffusion. The samples were thoroughly rinsed in DI water and dried in N_2 air.

Phosphorus diffusion

In order to optimize the phosphorus diffusion in SOI wafers, Tsuprem4 simulations were carried out. It was found from the simulation that, to obtain a diffusion profile shown in the Fig. 3.7 with surface concentration, sheet resistance and junction depth of $4\times10^{20}\ cm^{-3}$, 54 Ω/square and 0.26 μm respectively, phosphorus diffusion has to be carried out at 820 ^0C for 130 minutes. The samples were thoroughly cleaned by using the standard cleaning procedures followed prior to high temperature diffusion process, then dried in N_2 air and slowly loaded into the open-tube phosphorous diffusion furnace maintained at 820 °C under N_2 (flow rate 50 l/h) ambient. The ambient of phosphorous bearing impurities (P_2O_5) was created in the furnace by passing carrier gasses (O_2 and N_2 with flow rates of 2.5 l/h and 4 l/h respectively) through a $POCl_3$ bubbling chamber (maintained at 4 °C) and passing them into the furnace. In order to dilute and uniformly distribute the impurities into the furnace, an additional nitrogen supply (flow rate 50 l/h) was made and mixed with the impurity vapor. The chemical reactions which undergo inside the furnace are expressed as,

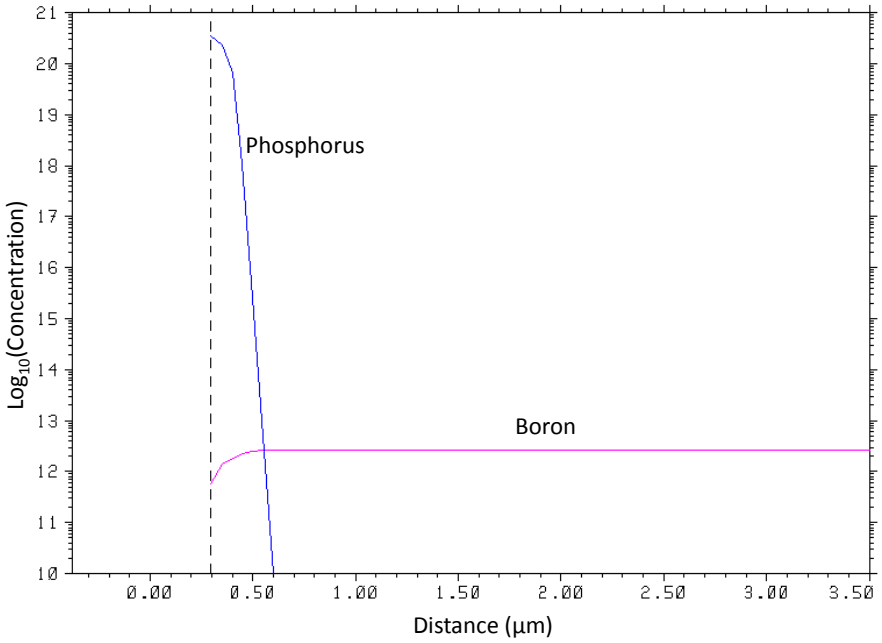

Figure 3.7: Simulated impurity concentration profile at n^+ - diffusion window after phosphorus diffusion for 130 min at 820 °C. The surface concentration of phosphorus and junction depth are estimated to be $\sim 4{\times}10^{20} cm^{-3}$ and $\sim$ 0.26 μm respectively.

$$4POCl_3 + 3O_2 \longrightarrow 2P_2O_5 + 6Cl_2 \tag{3.1}$$

$$2P_2O_5 + 5Si \longrightarrow 4P + 5SiO_2 \tag{3.2}$$

O_2 reacts with $POCl_3$ to produce P_2O_5 in the furnace. The P_2O_5 molecules are adsorbed on the sample's surface and they crack into atoms of phosphorous and oxygen on the surface of silicon (SOI) samples. Phosphorous atoms diffuse into the silicon samples and O_2 reacts with Si to form a thin layer of SiO_2 over the diffusion windows. Also phosphorus atoms readily combines with SiO_2 to form phosphosilicate (PSG) glass every where on the sample's surface. The diffusion was carried out for 130 minutes then impurity supply was stopped and the quartz boat was slowly unloaded with the samples from the furnace under N_2 ambient. The microscopic image of a sample taken just after phosphorous diffusion is shown in Fig.3.8. The Samples were soaked into BHF solution for 2 minutes to remove the PSG, then thoroughly rinsed in DI water and dried in N_2.

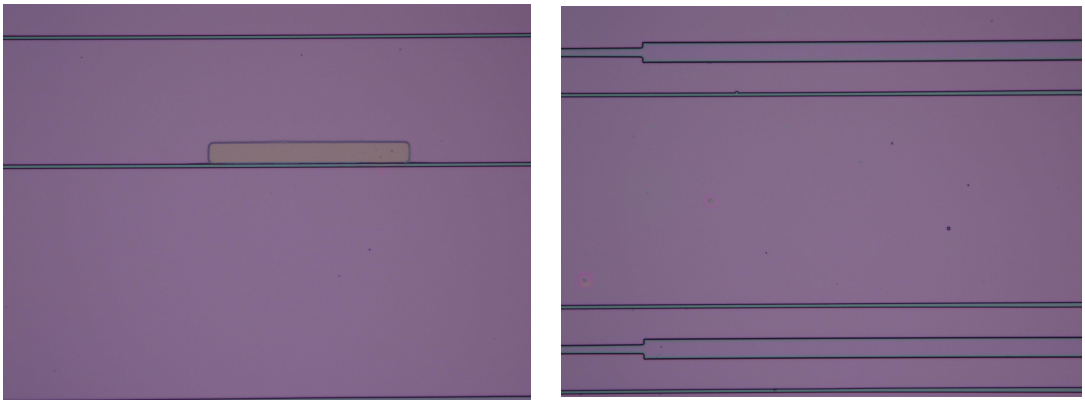

(a) (b)

Figure 3.8: Microscopic views of a SOI sample just after phosphorous diffusion. The brownish-violet colour shows a layer of phosphosilicate formed over the sample's surface: (a) the SOI sample showing diffusion window of a p-i-n waveguide, (b) the SOI sample showing waveguides and input section of a MZI.

3.5 Measurement of Sheet resistance

The sheet resistance of the semiconducting slices are usually measured by using four point probing technique. It is a simple apparatus as shown in Fig. 3.9 comprises of four metal probing tips which have been fixed with an insulating fixer one after another with spacing of S in a straight line. The probes were placed on the surface of the dummy sample (which has been doped with phosphorus impurities along with main samples in the furnace) as shown in the figure and controlled current source (I) and high impedance voltmeter were connected between the outer probes and inner probes respectively. Measurements were carried out by varying the injected current (I) through the outer probes and measuring corresponding voltage (V) drop across the inner probes. The sheet resistance R_s (Ω/square) was calculated by using the following expression.

$$R_s = \frac{\pi}{ln(2)} \frac{V}{I} \tag{3.3}$$

From repeated measurements on different places of the doped samples, we have estimated the average value of the sheet resistance as 47 Ω/square which in close agreement

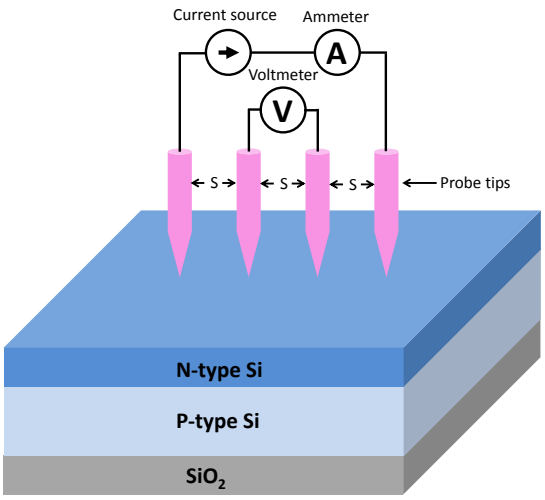

Figure 3.9: Schematic view of sheet resistance measurement by using four probe method

to the value (54 Ω/square) estimated by Tsuprem4 simulations.

3.6 Thermal Oxidation

After the phosphorus diffusion followed by removal of PSG, the samples were thoroughly cleaned by following standard cleaning procedures for oxidation. The dry oxidation was carried out for 10 minutes followed by wet oxidation for 50 minutes, again dry oxidation for 10 minutes at 900 °C to grow $\sim$ 300 nm thick SiO_2 (which is found enough for masking diffusion of boron through n^+ windows at around 1050 °C from Tsuprem4 simulations) to close phosphorous diffusion widows.

3.7 Boron Diffusion

Photolithography and oxide etching

The photolithography by using the p^+ - diffusion mask followed by oxide etching were carried out on the samples to delineate the windows through oxide layer as shown in Fig. 3.11(a) for boron diffusion. The samples were thoroughly cleaned with DI water and dried using N_2 air gun.

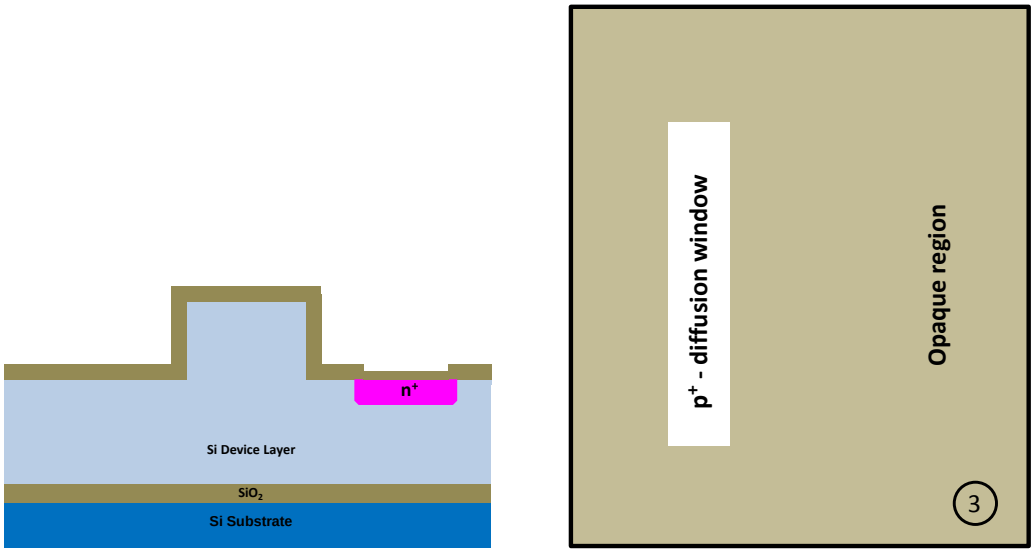

(a) (b)

Figure 3.10: Schematic cross section views of the SOI samples: (a) phophorous diffsion windows are closed by thermal oxidation of the sample, (b) Schematic top view of the p^+ - diffusion mask layout.

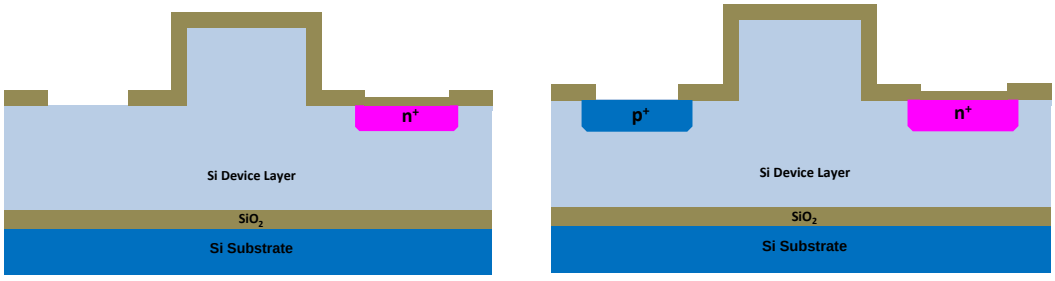

(a) (b)

Figure 3.11: Schematic cross section view of the sample: (a) after third photolithgraphy and patterning of silicon dioxide mask for boron diffusion. (b) The SOI sample after boron diffusion at 1050 ^0C for 10 minutes.

Solid source boron diffusion

We use boron nitride (BN1100) discs as a source for diffusion of boron into SOI substrates at high temperatures. The BN discs contain sintered mix of 40 % SiO_2 and 60 % BN. The BN discs were soaked into dilute HF solution (HF:DI H_2O::2:3) for 2 minutes to etch a thin layer containing a mix of SiO_2 and B_2O_3 (If the BN discs have already been used) then thoroughly rinsed in DI water and dried in N_2 air. Temperature of the diffusion furnace was set to 400 °C and maintained with full N_2 flow. In order to remove the water content from the cleaned BN discs, they were kept in a quartz boat and slowly loaded into the diffusion furnace and heated up at 400 °C for two hours in N_2 ambient. Temperature of the furnace was linearly ramped to 1000 °C and the BN discs were oxidized for 30 min in O_2 ambient with flow rate of 150 l/h to form a thin layer of B_2O_3 on the surfaces of BN discs. The oxidized BN discs were slowly unloaded from the furnace in full in N_2 ambient and the temperature was ramped up to 1050 °C. The cleaned samples and BN discs were alternatively placed one after the another into the quartz boat and again loaded slowly into the furnace. The nitrogen flow was set at 150 l/h and 3 % of oxygen flow was added with it. The boron diffusion was carried out for 10 minutes at the same temperature. The down flow of nitrogen transports B_2O_3 from the BN discs on the SOI samples and they are adsorbed on its surfaces. The B_2O_3 is cracked into boron and oxygen as expressed by the equations (3.4) and (3.5). The oxygen flow helps to enhance the diffusivity of boron in Si and produces etchable borosilicate glass (BSG) to some extent on diffusion windows. However, during the boron diffusion, very high concentration of boron on the diffusion windows makes a phase of boron-rich-silicon which is not easily to removable by etching. The values of boron diffusion parameters like temperature and time duration were estimated from Tsuprem4 simulations. The estimated concentration profile is shown in Fig. 3.12.

$$4BN + 3O_2 \longrightarrow 2B_2O_3 + 4N_2 \tag{3.4}$$

$$2B_2O_3 + 3Si \longrightarrow 4B + 3SiO_2 \tag{3.5}$$

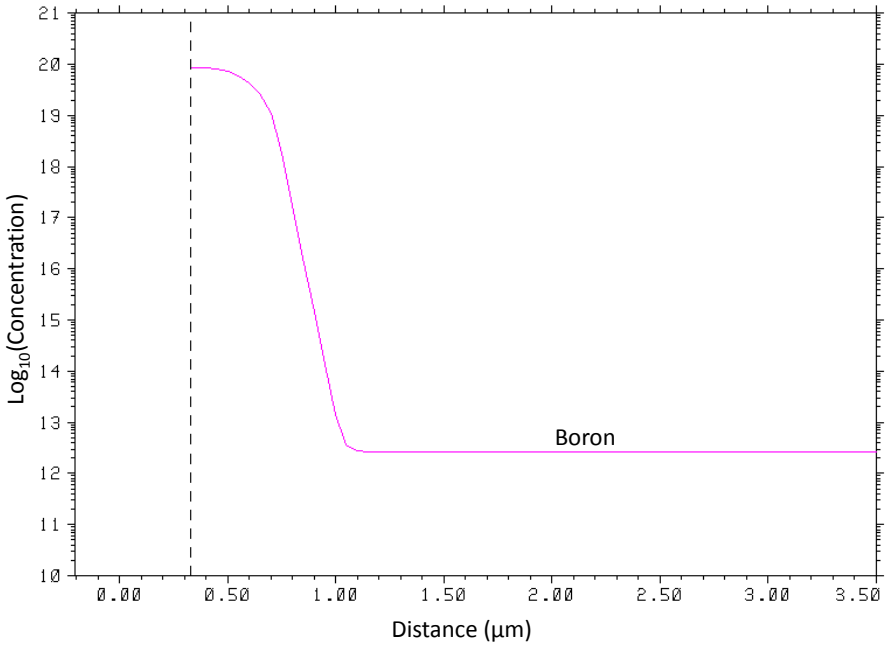

Figure 3.12: Simulated impurity concentration profile at p-diffusion window after boron diffusion at 1050 ^0C for 10 minutes. The surface concentration of boron and junction depth are estimated to be $\sim 9\times10^{19}cm^{-3}$ and $\sim$ 0.7 μm respectively.

Low temperature oxidation (LTO)

The samples were kept in quartz boat then slowly loaded into wet oxidation furnace and oxidized (wet oxidation) at 750 ° for 20 minutes to convert all the boron-rich-silicon in to BSG. The samples were slowly unloaded from the furnace then soaked into BHF solution until complete removal of BSG was ensured.

Drive-in

In order to drive-in the predeposited impurities of the samples, they were placed in a quartz boat and slowly loaded into annealing furnace maintained at 900 °C in N_2 ambient. The samples were kept inside the furnace for 60 minutes in full N_2 ambient to drive-in the diffused impurities well into silicon substrate such that the junction depths becomes 1 μm (for both n+ and p+ sides). The samples were slowly unloaded from the furnace. The sheet resistance for n^+ doping and p^+ doping after the drive-in were estimated to be 35 Ω/square and 52 Ω/square respectively. These values are found to be in close agreement to the values obtained from Tsuprem4 simulations (38 and 57

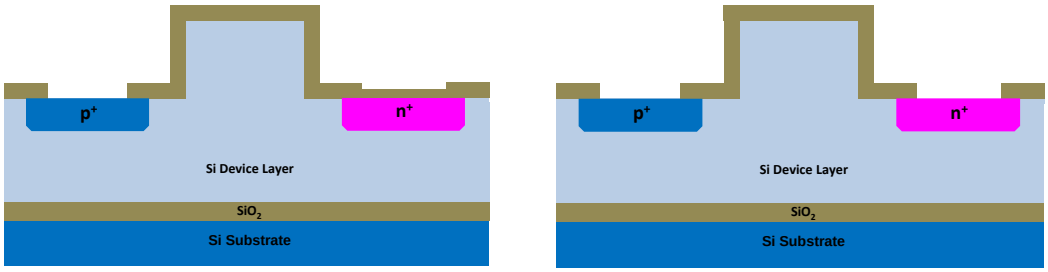

(a) (b)

Figure 3.13: Schematic cross section view of the sample: (a) after Drive-in at 900 ^0C for 60 minutes, (b) after cleaning the surfaces of n^+ and p^+ windows by using fourth and fifth lithographies using respective masks and oxide etching.

Ω/square respectively).

3.8 Lithography for making ohmic contacts on diffused regions

In general the quality of ohmic contact formed by metal-semiconductor (for the present case Aluminum-silicon) interface is not only depending upon the doping concentration on the semiconductor surface (at the interface), but also decided by its roughness and cleanliness. So, a photolithography and etching could be carried out to make clean surfaces at diffused regions of the wafer. However it was found that, after carrying out the phosphorus diffusion, BHF removal, oxidation boron diffusion and low temperature oxidation on the SOI wafer successively, the insulating layers which are wrapping the surfaces of n (silicon dioxide) and p (borosilicate) diffused widows have been found different in thickness and constituents. Also when they were etched with BHF solution, it was found that the etch rate of the layer on p diffused widow was greater than that for the n diffused windows. So, in order to form clean surfaces on p and n diffusion windows photolithography followed by etching were carried out for both p and n diffused windows respectively (the fourth lithography followed by oxide etching for p region and fifth lithography followed by oxide etching for n region). The samples were thoroughly rinsed in DI water and dried in N_2.

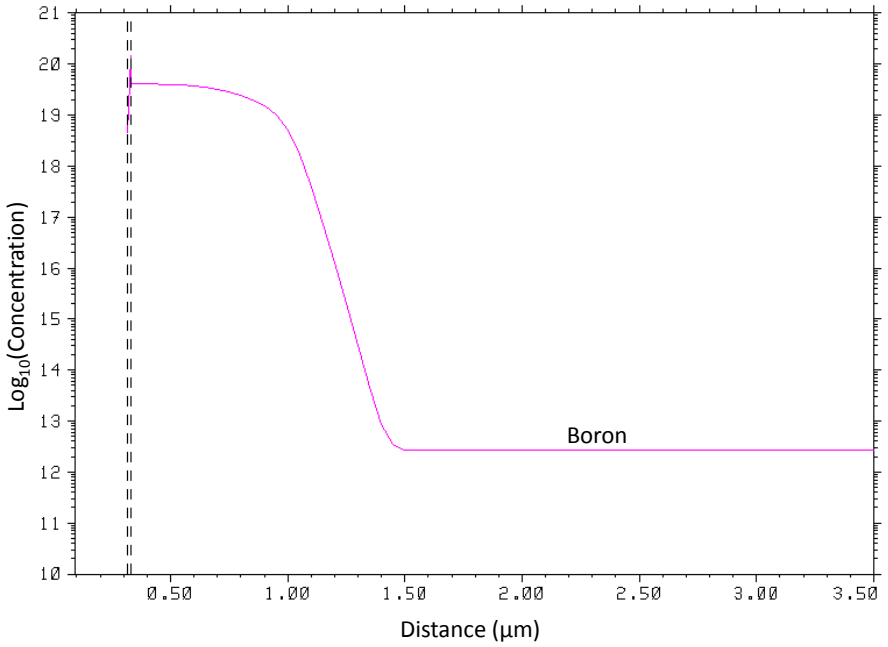

Figure 3.14: Simulated impurity concentration profile at p^+-diffusion window after drive in at 900 ^0C for 60 minutes in N_2 ambient. The surface concentration of boron and junction depth are estimated to be $\sim 5{\times}10^{19} cm^{-3}$ and $\sim$ 1.03 μm respectively.

For making ohmic contacts with the doped regions of the samples, they were thoroughly cleaned and soaked into 5 $\%$ HF solution for 5 seconds and dried in N_2. The samples were loaded in to the metallization chamber and layer of metal was coated on front surface of every sample by thermally evaporating aluminum under high vacuum conditions to form a uniform aluminum layer of thickness $\sim$ 500 nm.

3.9 Metallization

Photolithography and patterning of Al film

After the deposition of aluminum films on the top surface of the samples, an uniform layer of PPR was spin coated and baked for 17 minutes at 80 °C. The PPR was exposed to UV light through the metallization mask and developed with a standard developer solution. The samples were baked for 40 minutes at 120 °C to harden the resist mask. The exposed aluminum regions were etched away by using aluminum etching (H_3PO_4:CH_3COOH:HNO_3::76:15:3:5 ml) solution then resist mask was stripped

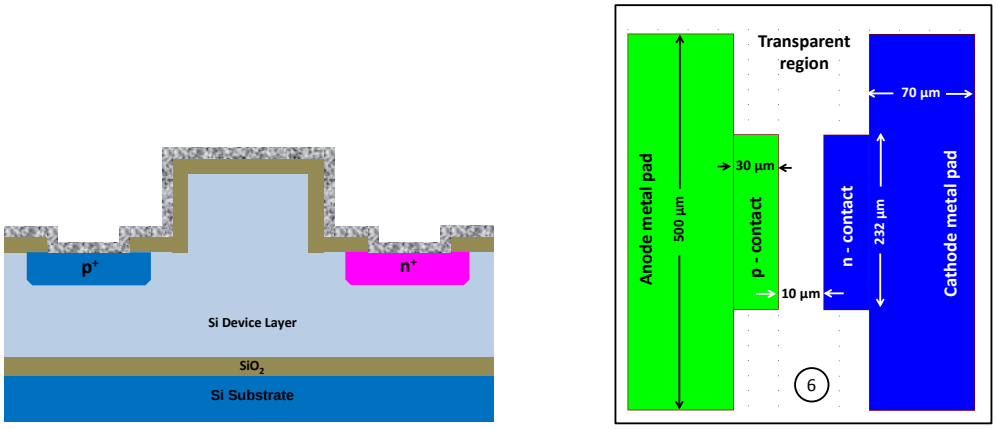

(a) (b)

Figure 3.15: (a) Schematic cross section view of the sample after Al deposition. (b) Schematic top view of the sixth mask which is used to pattern the metal films coated on the samples.

with acetone, thoroughly cleaned with DI water and dried in N_2. The microscopic top view of a sample after patterning the Al layer is as shown in the Fig. 3.17.

3.10 Polishing

In order to efficiently couple the light to and from various devices which are present in the processed samples, each device requires an optically smooth and flat surface at its both input and output ends. So the samples were polished at end-facets by using a mechanical polishing machine, which uses polishing sheets made up of polythene films coated with diamond grains of sizes ranging from 30 μm to 0.1 μm. Then the samples were cleaned with DI water, acetone and again in DI water. The water from the samples were dried by using nitrogen air gun.

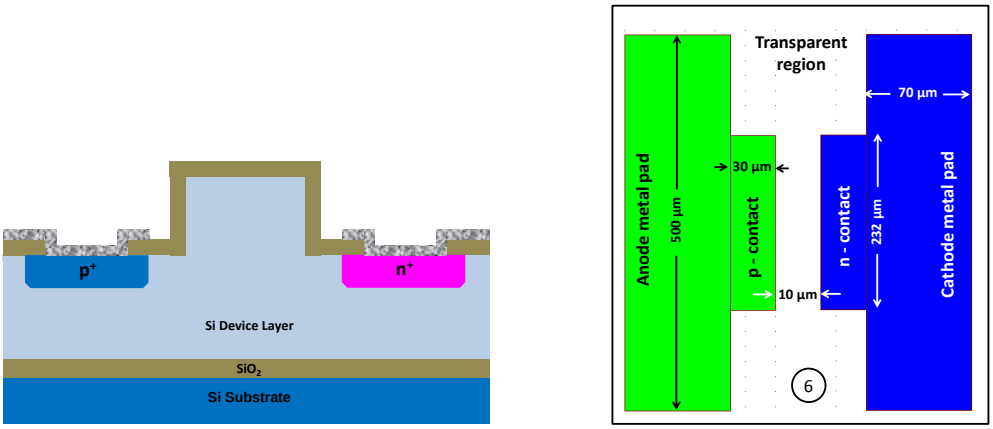

(a) (b)

Figure 3.16: Schematic cross section view of the sample; (a) After Drive-in at 900 ^0C for 60 minutes. (b) After cleaning the surfaces of n^+ and p^+ windows by using fourth and fifth lithographies using respective masks and oxide etching.

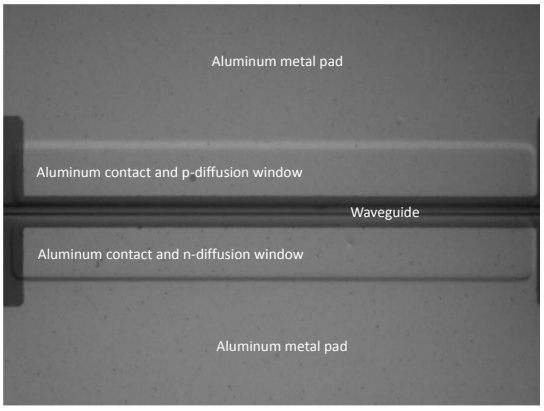

Figure 3.17: Microscopic image of top view of the p-i-n waveguide used in VOA and MZM showing its various sections after patterning of Aluminum.

CHAPTER 4

Experimental Results and Discussions

This chapter discusses the experiments and their results for the fabricated devices viz. straight waveguides, bend waveguides, 1x2 MMI couplers / splitters, Mach-Zehnder interferometers (MZIs), p-i-n diodes / waveguides, variable optical attenuators(VOAs) and Mach-Zehnder modulators (MZMs) when they are excited with an optical, electrical and both signals in the laboratory.

4.1 Optical Loss and Mode-Profile Measurement

The optical loss-metrics of passive and active optical / optoelectronic devices, which have been fabricated in SOI wafers were measured using an end-fire optical coupling system shown in Fig. 4.1. It consists of a tunable laser source (TLS), fiber mount (FM), polarization controller (PC), collimation lens (CL), polarizer (P), input coupling lens (IL), mounting stage for the device under test (DUT), output coupling lens (OL), optical power detector / meter (PM) and infrared camera (IR). Both tunable laser source and optical power meter are interfaced with a computer for automating some parts of the measurements. The positions of all the lenses and the DUT are manually controlled by using respective micropositioners which had been attached to them (micropositioners are not shown in the figure). The light generated by the tunable laser source is collected through a single mode fiber (SMF) and passed through the polarization controller to promote a particular type of polarization (say TE). The light output from the polarization controller is sent via another SMF, and then collimated by the lens after collecting the light from the fiber, whose end- facet is kept exactly at the focal point of the lens. The collimated light is passed via the polarizer and then focused into the input end-facet of the particular waveguide by using the input coupling lens.

The polarization-controller is tuned to maximize the one of the two linear polarizations (TE or TM), and the output coupling lens is kept at a distance of its focal length

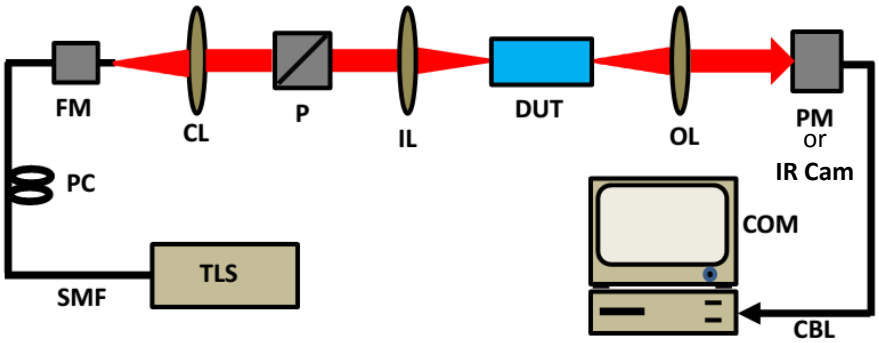

Figure 4.1: Schematic of the end-fire coupling system used for optical characterization of the fabricated devices. The setup consist of a tunable laser source (TLS), polarization controller (PC), collimation lens (CL), polarizer (P), input coupling lens (IL), mounting stage for the device under test (DUT), output coupling lens (OL), optical power detector / meter (PM) and infrared camera (IR).

from the end-facet of the waveguuide. The distance between the input end-facet of the sample and the input coupling lens and the vertical position of the sample are adjusted by using respective micropositioners until the light is coupled into any one of the waveguides. At a stable wavelength (1550 nm), optical power and specific polarization of the input laser light, the optical power output of each one of the above mentioned devices in a sample are maximized by properly adjusting the position of the sample and lens in such a way that the light coupling into the device get maximized, then the measurements are carried out. The approximate locations of each one of the devices are identified and conformed by replacing tunable IR laser with a visible laser source of wavelength 632 nm.

The insertion loss of the devices were measured at a wavelength of 1550 nm by measuring optical power input P_{in} to the device and optical power received from the output port of each device P_o using optical power meter. It is estimated by using equation 4.1,

$$Insertion\,loss(IL) = 10\log_{10}(\frac{P_o}{P_{in}}) \tag{4.1}$$

Where, P_{oT} is the total optical power output and P_{in} is the input optical power. The value of insertion losses for a number of straight waveguides, bend-waveguides and waveguides for attenuators have been measured and compared for both TE and TM

polarized light of wavelength around 1550 nm.

4.1.1 Insertion Loss of Various Waveguides

The insertion loss of a number of waveguides have been measured by using the end-fire optical coupling system. Fig.4.2 shows the insertion loss as a function of device number for straight waveguides having width $W \sim 4$ μm. A typical value of insertion loss was found to be 6.13 (5.86) dB for TE (TM) polarization. Fig.4.3 shows the insertion loss as a function of device number for waveguides having width $W \sim 5.5$ μm. The typical value of insertion loss was found to be 6.43 (4.65) dB for TE (TM) polarization. Fig.4.4 shows the insertion loss as a function of device number for bend waveguides having width $W \sim 5.5$ μm and bending radius $R \sim 25$ mm. The typical value of insertion loss was found to be 7.10 (6.18) dB for TE (TM) polarization. Fig.4.5 shows the insertion loss as a function of device number for a number of attenuator waveguides. The typical value of insertion loss of 6.58 (6.35) dB was exhibited by the attenuator waveguides for TE (TM) polarization.

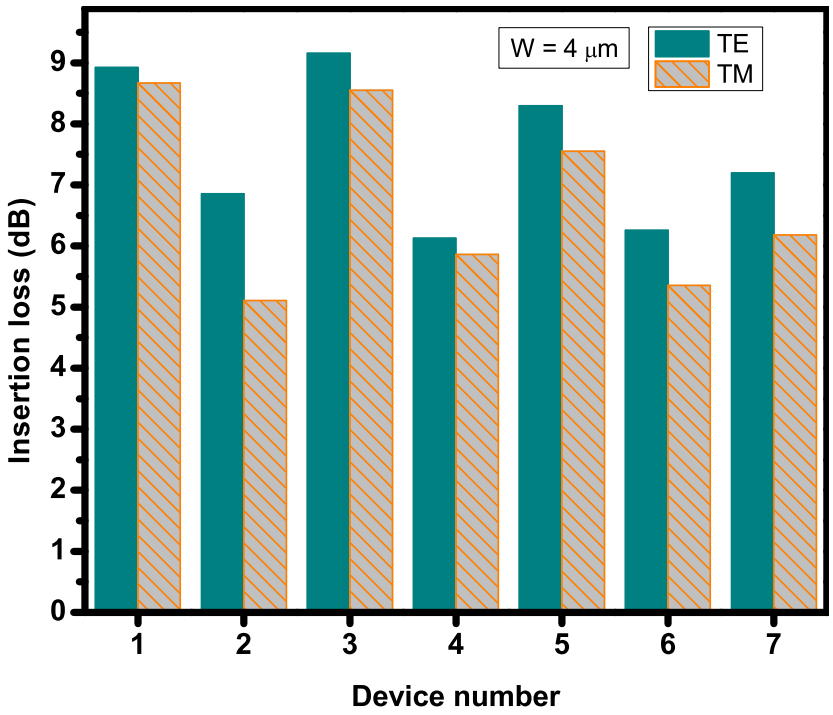

Figure 4.2: The insertion loss as a function of device number for the fabricated straight waveguides having l (length) = 2.3 cm, $W \sim 4$ μm, $H \sim 4.5$ μm and $h \sim 3$ μm when excited with TE and/or TM polarized light of λ = 1550 nm.

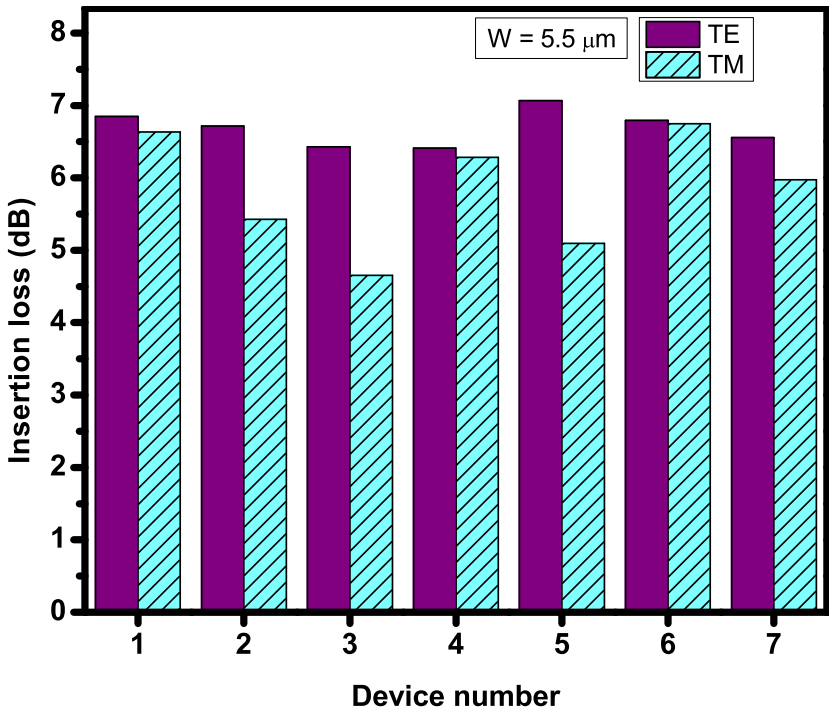

Figure 4.3: The insertion loss as a function of device number for the fabricated straight waveguides having $l \sim 2.3$ cm, $W \sim 5.5$ μm, $H \sim 4.5$ μm and $h \sim 3$ μm when excited with TE and/or TM polarized light of λ = 1550 nm.

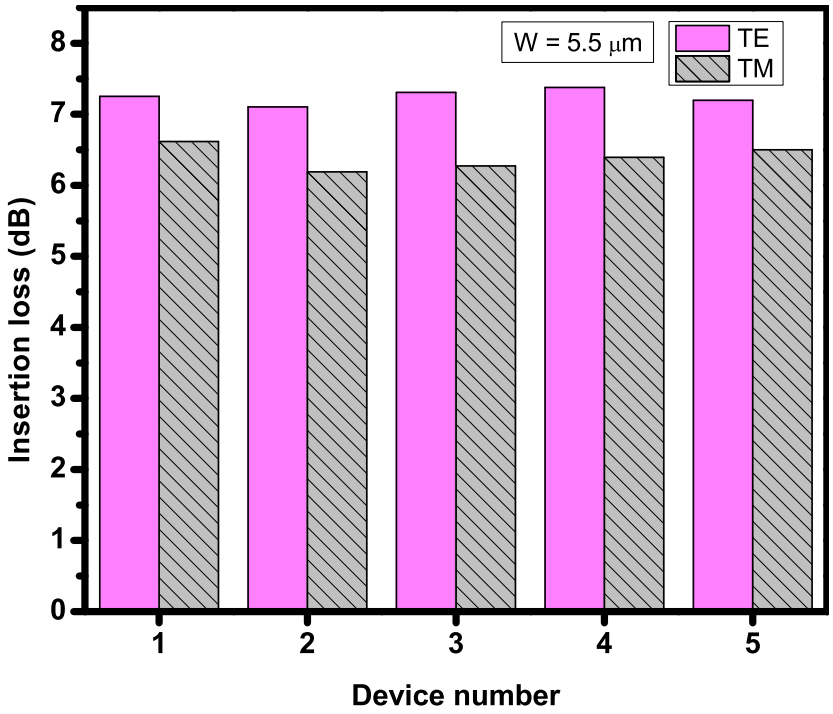

Figure 4.4: The insertion loss as a function of device number for the fabricated bend waveguides having $l \sim 2.3$ cm, $R \sim 25$ mm, $W \sim 5.5$ μm, $H \sim 4.5$ μm and $h \sim 3$ μm when excited with TE and / or TM polarized light of λ = 1550 nm.

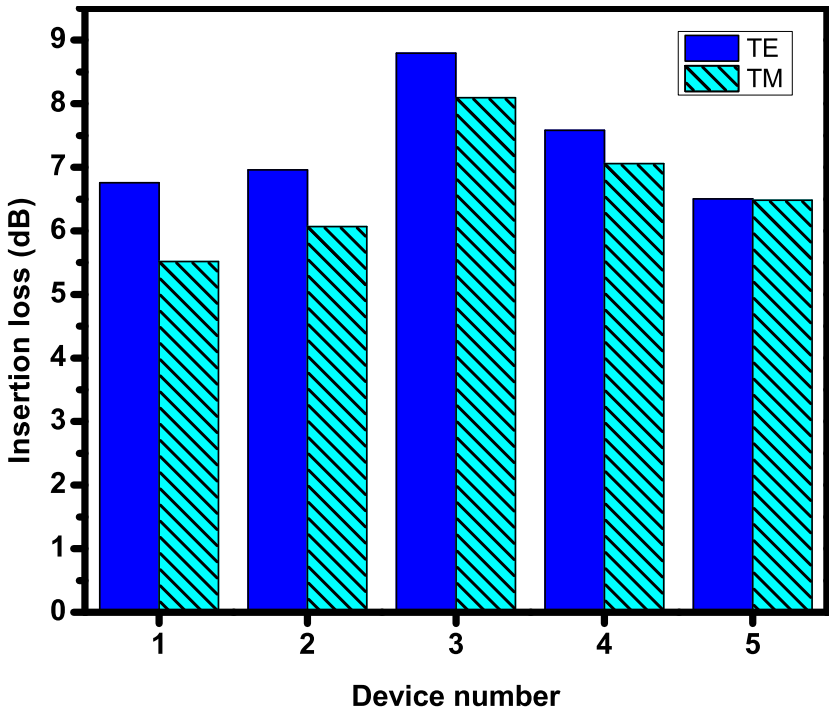

Figure 4.5: The insertion loss as a function of device number for the fabricated attenuator waveguides having $l \sim 2.3$ cm, $H \sim 4.5$ μm and $h \sim 3$ μm when excited with TE and / or TM polarized light of λ = 1550 nm.

While examining the insertion loss characteristics of all the fabricated passive integrated optical devices, it is interesting to note that the insertion loss for TM polarization is found to be less than that for TE polarization. This trend in insertion loss shown by the devices is believed to be due to the high confinement of TM polarized light than that of TE polarized light in the devices.

The propagation loss (also known as waveguide loss) which comprises of losses due to bulk scattering, absorption and radiation of the optical waves in the waveguide are usually measured by using any one of techniques such as waveguide cut-back method, light scattering and Fabry-Perot cavity resonance. However, the Fabry-Perot cavity resonance method was adopted for the measurement of propagation loss of waveguides in our laboratory because of its simplicity and reliability for medium level reflecting surfaces (for normal incidence, the Fresnell reflectivity $R = (n_{si} - n_{air})^2/(n_{si} + n_{air})^2$ $\sim$31 $\%$) formed by air-silicon interfaces at polished waveguide ends.

The optical beam from the input lens is coupled into the waveguide then it is allowed to propagate along the waveguide axis with allowed optical field distributions (modes).

A fraction of propagating wave is reflected back and forth inside the waveguide by the two end facets causing cavity resonance, then the rest of it is transmitted from the both ends which is measured by the optical power meter placed at the output side of the device under test. The optical output power was measured as a function of the wavelength of the input light. The loss in the waveguide may be expressed as,

$$\alpha L\,(neper) = \ln[\frac{\sqrt{\zeta}-1}{R(\sqrt{\zeta}+1)}] \tag{4.2}$$

where,

$$\zeta = \frac{I_{max}}{I_{min}} \tag{4.3}$$

is the ratio between the maximum intensity I_{max} to minimum intensity I_{min} of the output light verses wavelength and R is the reflectivity of the waveguide end-facets (assumed as equal for both ends).

Since,

$$\frac{log_{10}(x)}{ln(x)} = 0.434 \tag{4.4}$$

The optical loss in decibel (dB) may be expressed as

$$\alpha L\,(dB) = 4.34\log_{10}[\frac{\sqrt{\zeta}-1}{R(\sqrt{\zeta}+1)}] \tag{4.5}$$

The measurements have been carried out by automating the laser source (for wavelength tuning with constant power) and optical power meter by interfacing them with the computer using LabView program. For TE polarization, the typical value of propagation loss for the waveguide of with $W \sim 5.5$ μm and $W \sim 4$ μm were found to be around 1.3 dB/cm and 1.4 dB/cm for TE polarization. Whereas, for TM polarization they were found to be around 1 dB/cm and 1.1 dB/cm respectively.

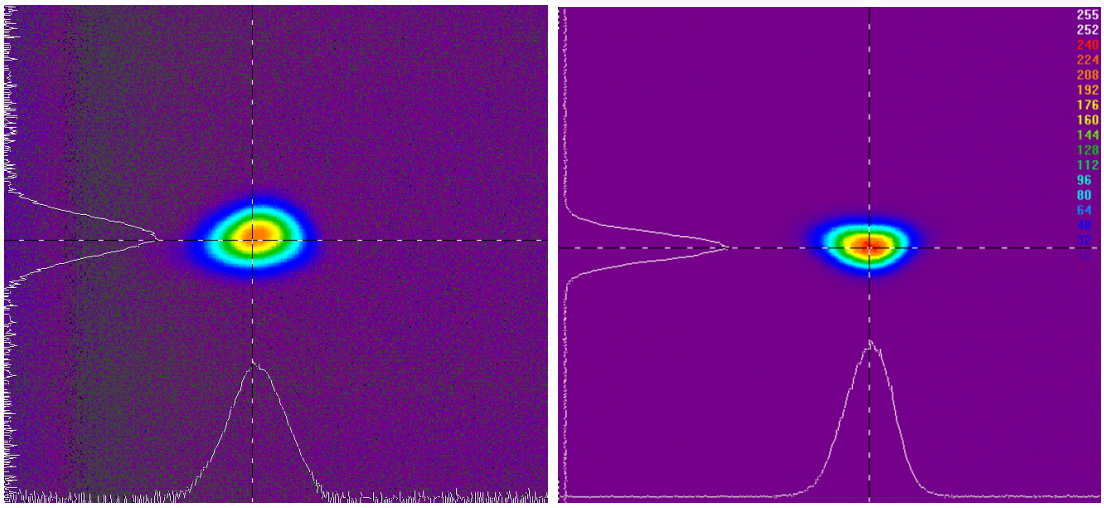

(a) (b)

Figure 4.6: The mode profiles of the waveguide have W = 4 μm at λ = 1550 nm: (a) for TE polarization, (b) for TM polarization.

4.1.2 Mode Profile Measurement

The guided mode profile of each one of the fabricated devices has been recorded by collecting the light from their output ports through the lens (OL) and projecting it on the sensor of the IR camera. The captured mode profiles have been compared with the mode profile of a single mode fiber which had been kept in place of the sample during the measurement of fiber mode profile. Let the effective diameter of actual and captured mode profiles of a single mode fiber be W_f and W_{fc} respectively and the effective width (height) of actual and captured mode profile of the device be ω_x (ω_y) and W_{xc} (W_{yc}) respectively. Then the scaling factor can be written as $a = W_f/W_{fc}$. Then the actual width and height of the device mode profile becomes $W_x = aW_{xc}$ and $W_y = aW_{yc}$ respectively. For TE(TM) polarization, the effective mode size of the waveguide having W = 4 μm was found to be around 5.5 (5.4) μm and 3.4 (3.4) μm along horizontal (x) vertical (y) directions respectively. These values are found to be in close agreement to the calculated values from FEMsim simulations. The mode profiles are shown in Fig. 4.6 for TE and TM polarized light.

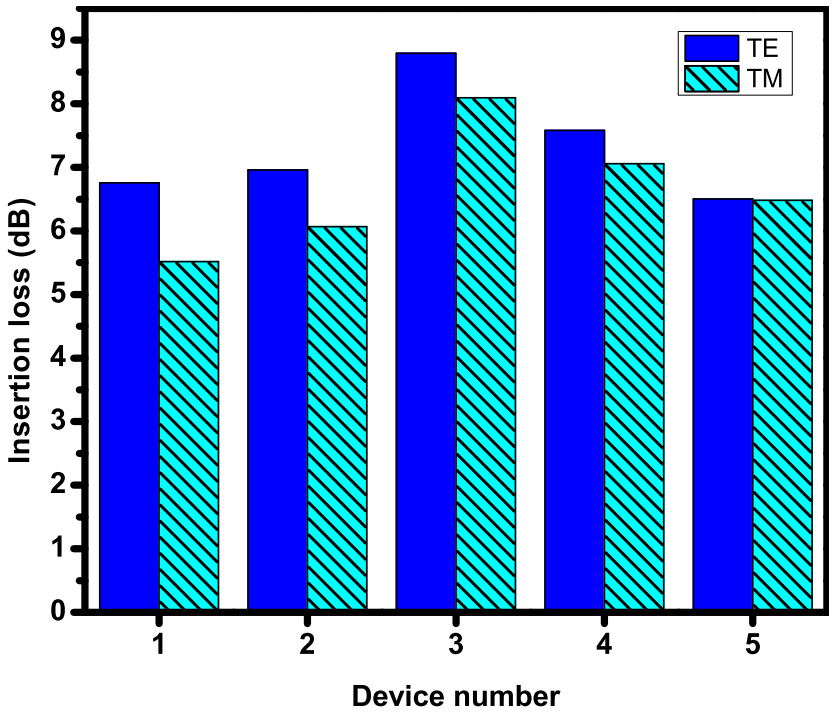

Figure 4.7: Insertion loss (IL) as a function of device number for the fabricated 1x2 MMI optical power splitters when exited with TE and/or TM polarized light of $\lambda \sim 1550$ nm.

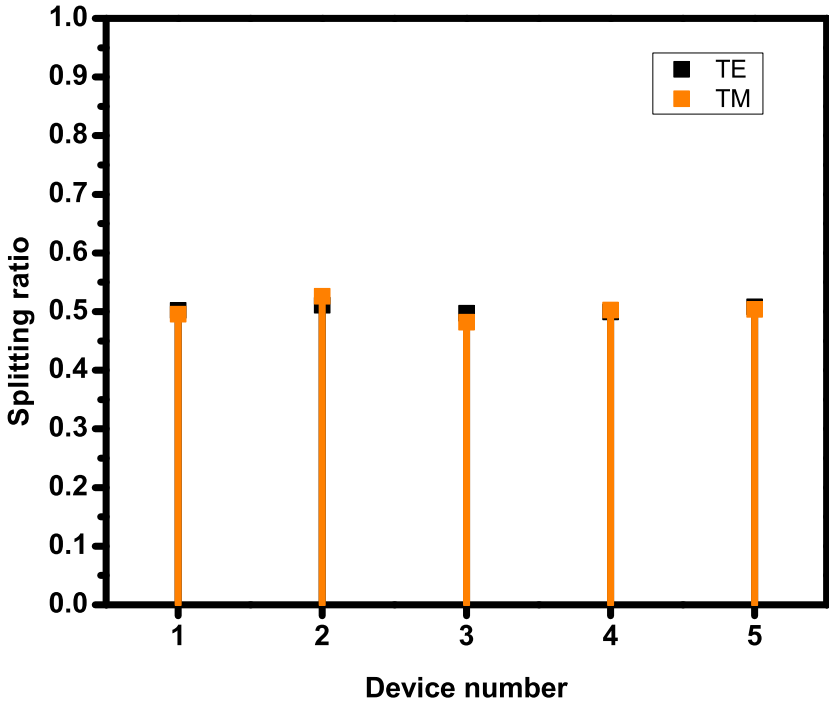

Figure 4.8: The optical power splitting ratio as a function of device number for the fabricated 1x2 MMI optical power splitters when exited with TE and/or TM polarized light of $\lambda \sim 1550$ nm.

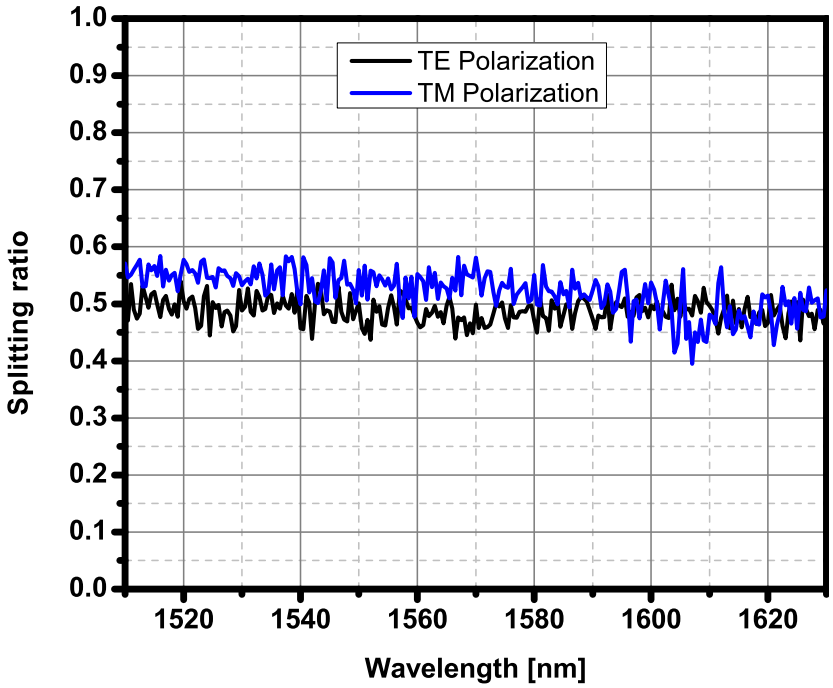

Figure 4.9: The optical power splitting ratio of a fabricated 1x2 MMI optical power splitter as a function of communication wavelength covering C and L optical band for TE and TM polarized light.

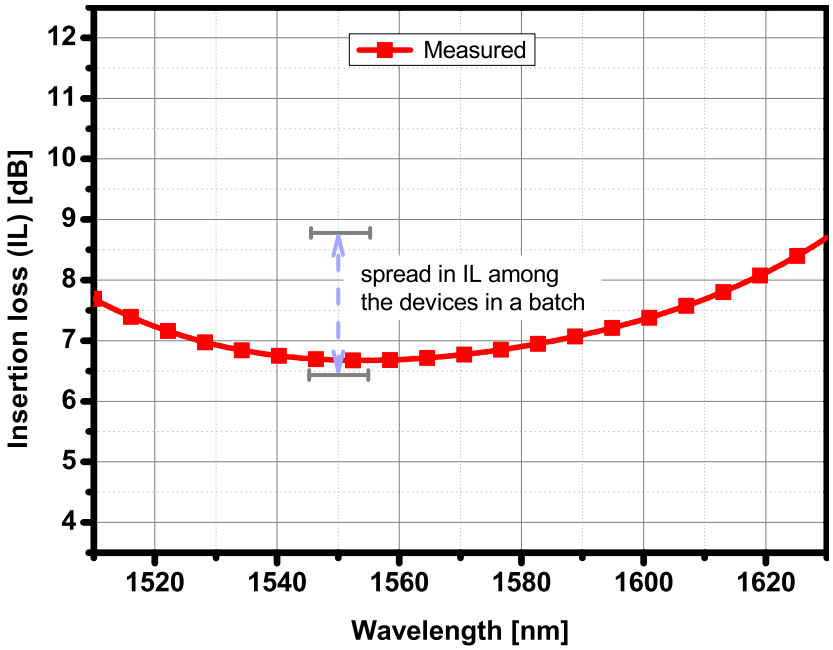

Figure 4.10: The wavelength dependent insertion loss characteristics of a 1x2 MMI optical power splitters for TE polarized light under C+L optical band. The devices in a sample (or batch) show a spread in insertion loss from 6.50 dB to 8.79 dB (compared around the wavelength of 1550 nm.)

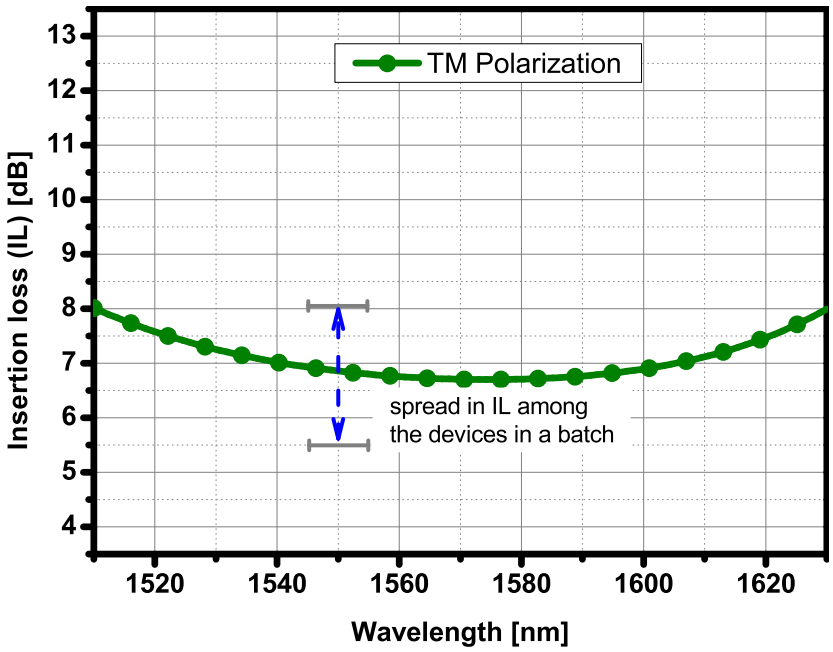

Figure 4.11: The wavelength dependent insertion loss characteristics of a 1x2 MMI optical power splitter for TM polarized light under C+L optical band. The devices in a sample (or batch) show a spread in insertion loss from 5.5 dB to 8 dB (compared around the wavelength of 1550 nm.)

4.1.3 1x2 MMI Optical Coupler or Power Splitter

In order to measure the insertion loss and power splitting ratio of the 1x2 MMI power splitters, a linearly polarized light of wavelength of $\sim$ 1550 nm was coupled with its input port and the optical power at either of the output ports were measured for both TE and TM polarizations. Fig. 4.7 shows the insertion loss as a function of device number for the wavelength of $\sim$ 1550 nm. The devices show a typical insertion loss of 6.76 (5.52) dB for TE (TM) polarization. The power splitting ratio is defined as the ratio of power at one of the output ports to sum of power at all the output ports of the device $[P_{out1}/(P_{out1} + P_{out2})]$. Fig. 4.8 shows the splitting ratio as a function of device number. The typical value of splitting ratio was found to be around 0.508 (0.503) for TE (TM) polarization. The wavelength dependent power splitting ratio as shown in Fig. 4.9 for TE and TM polarizations were obtained by measuring the output optical power at either of the output ports, while maintaining the input power constant and varying the wavelength of the light coupled at the input port. The value of power splitting ratio was found to be nearly 50 $\%$ for both polarizations. Fig. 4.10 and Fig. 4.11 show the insertion loss as a function of wavelength covering C+L optical band for TE and TM

polarizations respectively. The splitter shows almost flat response around C band. All the devices in a batch were working but showing a spread in insertions loss as shown in figures.

4.1.4 MMI based Mach-Zehnder Interferometer (MZI)

In order to measure the insertion loss and wavelength dependent characteristics of MZIs, a linearly polarized light was coupled into the input port of each one of the devices and the corresponding optical power output was measured for both TE and TM polarizations. Fig. 4.12 shows the insertion loss for MZIs as a function of device number. The devices show a typical insertion loss of 7.15 (6.43) dB for TE (TM) polarization. The Fig. 4.13 and Fig. 4.14 show the insertion loss as a function of wavelength for TE and TM polarizations respectively. The MZI shows almost flat response for full C optical band and the insertion loss variation over full C and L band is found to be within 4(3) dB for TE(TM) polarization.

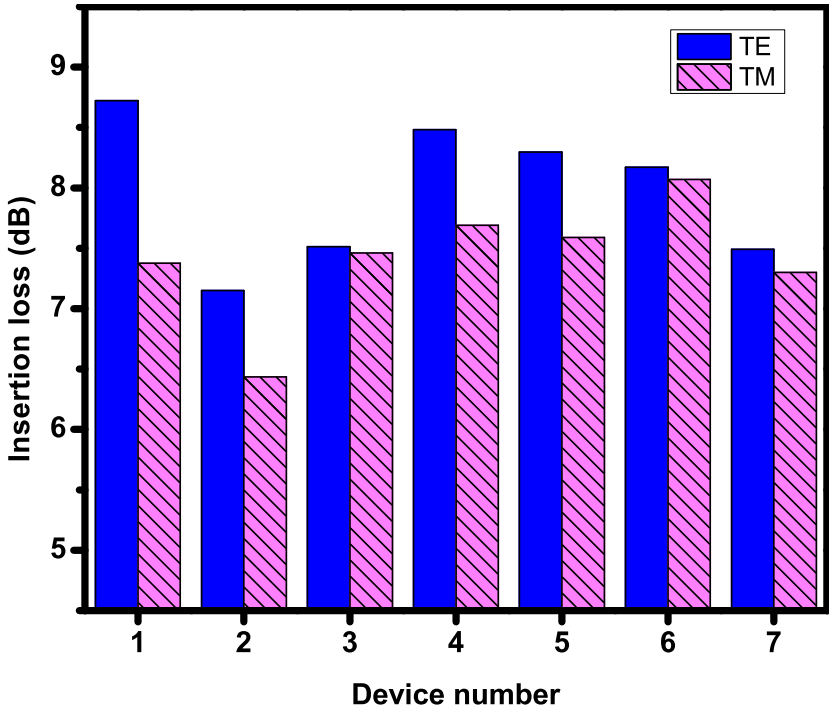

Figure 4.12: The insertion loss as a function of device number for the fabricated MZIs when exited with TE or TM polarized light of λ = 1550 nm.

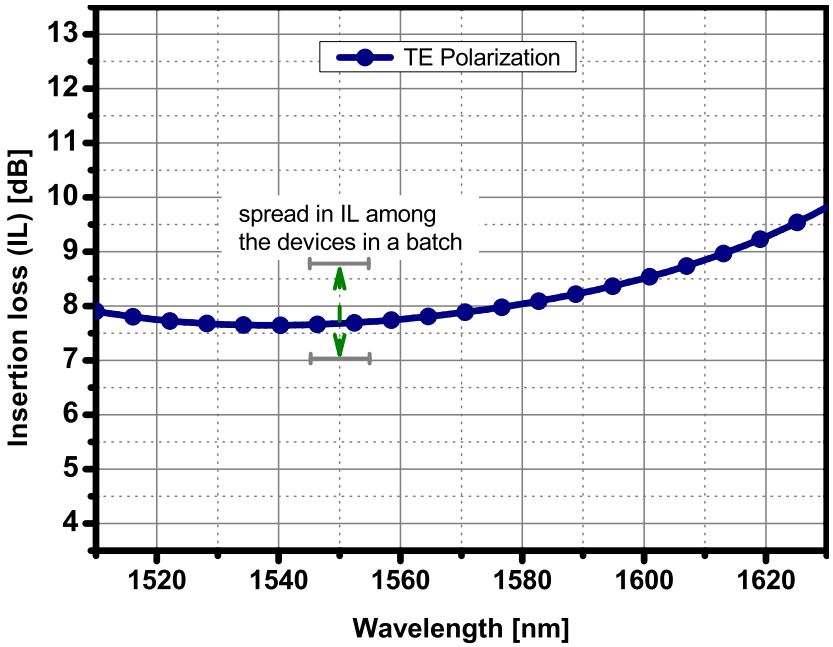

Figure 4.13: The wavelength dependent insertion loss characteristics of MZIs for TE polarized light under C+L optical band. The device shows a almost flat response for C band. The devices in a sample (or batch) show a spread in insertion loss from 7.15 dB to 8.72 dB (compared around the wavelength of 1550 nm.)

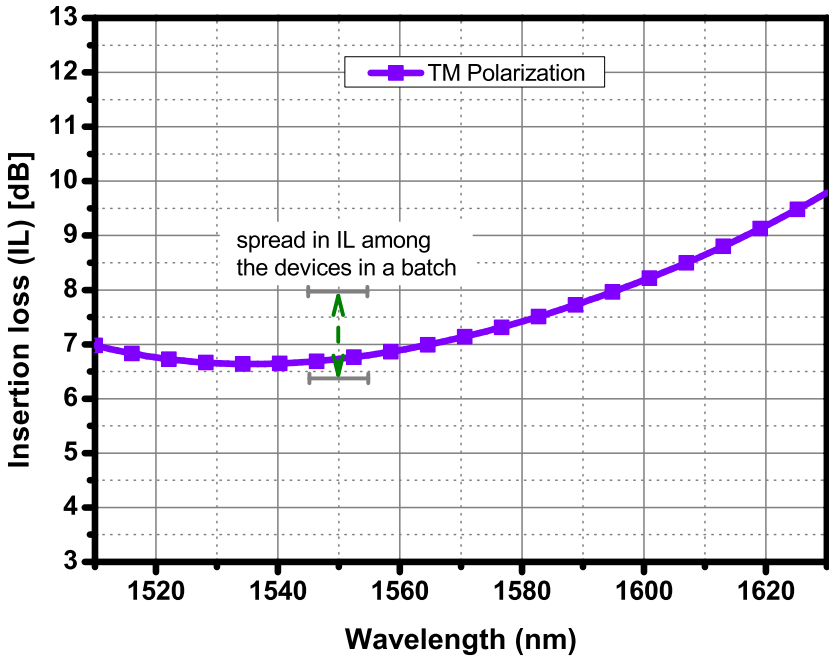

Figure 4.14: The wavelength dependent insertion loss characteristics of MZI power splitter for TM polarized light under C+L optical band. The device shows a almost flat response for C band. The devices in a sample (or batch) show a spread in insertion loss from 6.43 dB to 8.07 dB (compared around the wavelength of 1550 nm.)

4.1.5 p-i-n Waveguide: Current-Voltage Characteristics

The fabricated samples containing p-i-n diodes / waveguides with p^+ and n^+ impurity windows of length L = 230 μm and width W_d = 20 μm of each were characterized by using the semiconductor device parameter analyzer (Agilent B1500A). The anode and cathode metal pads of the p-i-n diode were connected to the semiconductor parameter analyzer through two probing tips and then the device current was measured as a function of applied bias voltage. The steady state current-voltage (I-V) characteristics were obtained for all the p-i-n diodes in the sample and a typical characteristic curve is shown in Fig. 4.15. The typical value of reverse saturation current and series resistance are found to be of the order of 3 nA and 900 Ω (at +1V bias) (which includes the contact resistance between the probe tips and metal pads) respectively.

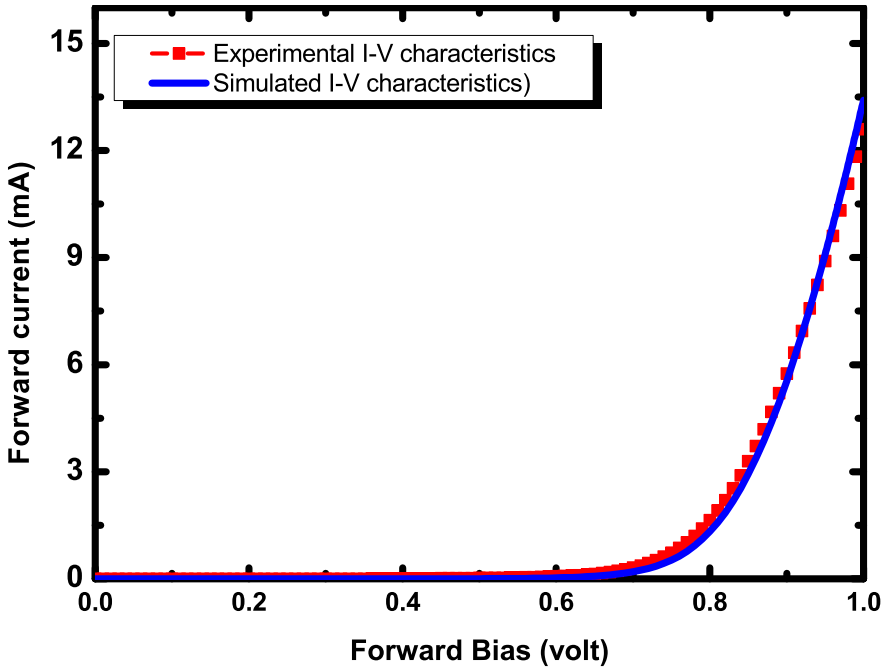

Figure 4.15: The typical I-V characteristics of one of the fabricated p-i-n diodes / waveguides.

4.1.6 Variable Optical Attenuator (VOA): Attenuation Characteristics

The optical attenuation characteristics of VOAs were measured by using the electrical probing system integrated with the end-fire optical coupling setup shown in Fig. 4.16.

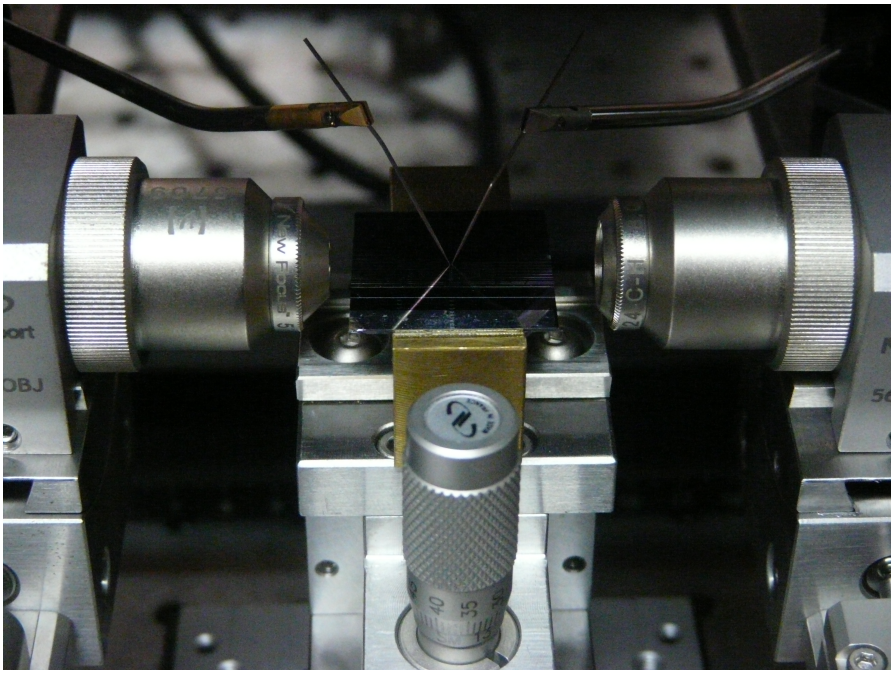

Figure 4.16: Photograph of the electrical probing system integrated with the end-fire optical coupling setup which was used to characterize VOAs and MZMs.

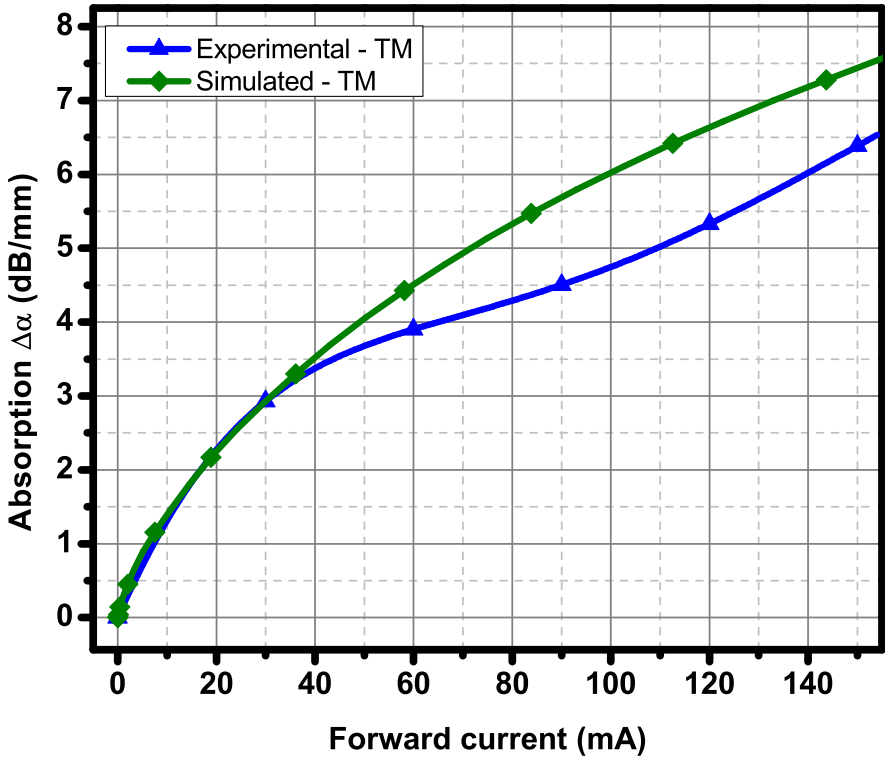

Figure 4.17: The measured and simulated optical attenuation as a function of forward current to variable optical attenuators having a length of 230 μm for TM polarization light at around λ = 1550 nm.

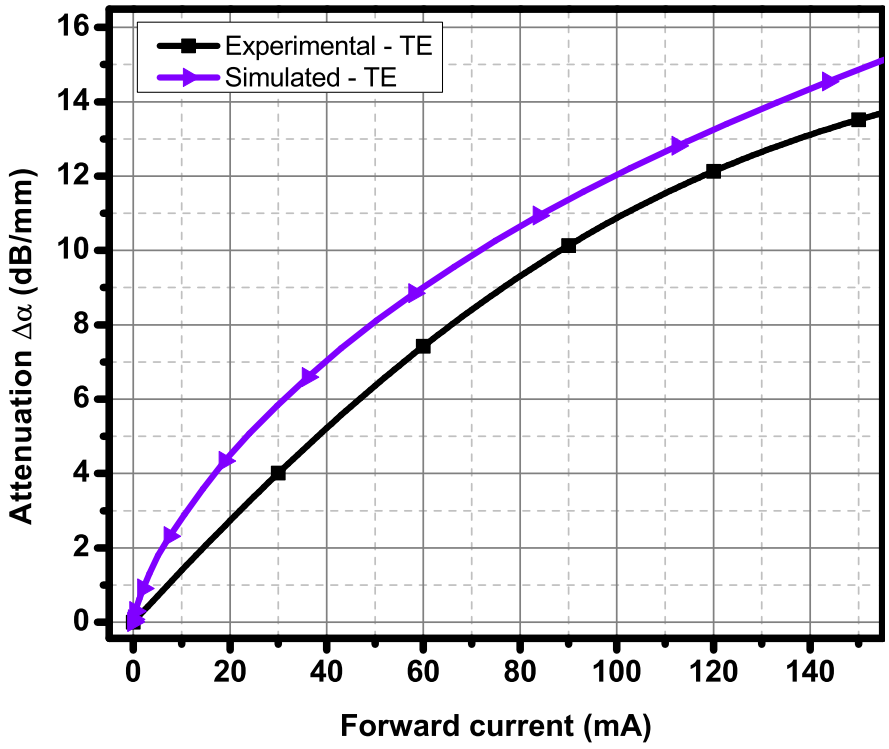

Figure 4.18: The measured and simulated optical attenuation as a function of forward current to variable optical attenuators having a length of 230 μm for TE polarization light at around λ = 1550 nm.

The laser light of wavelength ~1550 nm obtained from a tunable laser was controlled with a polarization controller, collimated by a lens to get a pencil beam of light and passed in parallel to the rail of the characterizing setup. The collimated light beam was polarized by a Ken-Thompson polarizer then coupled to the input port of the VOA using an input coupling lens. The output light of the VOA was collected by using an output coupling lens and measured with an optical power meter. The anode and cathode metal pads were connected to a variable direct current source through two probing tips having tip diameters of 8 μm. The optical power output from the VOA was measured as a function of injected current while keeping the input optical power and polarization fixed. The optical attenuation as a function of injected current under forward biased mode for a group of VOAs for TE and TM polarizations are shown in Fig. 4.17 and Fig. 4.18 respectively. The measured attenuation characteristics matches with the simulated characteristics for the injected current rage of 0 - 40 mA, beyond which it tends to deviate for the TM polarization. This is expected because the heat dissipated during the current flow through the device causes reduction of mobility of charge carriers and increment of the real part of the refractive index. These changes and their effects may

be pronounced beyond the current range of 40 mA so that the absorption coefficient deviates from the simulated curve in which we have not included the thermooptic effect. This temperature effect may be reduced if the contact resistance can be reduced by optimizing the annealing temperature and time during the deposition of aluminum over the samples. However, the attenuation characteristics for TE polarized light is showing the similar trend of simulated curve but with a negative shift in attenuation as shown in Fig. 4.18. This may be due to the less overlap and hence the less interaction between the guided optical mode with the injected carriers. This less overlap is assumed due to nonidealities of the waveguide structure and dimensions (The fabricated waveguide shows slanted side walls instead of being vertical). The reference current of 15 mA was considered for a performance comparison between attenuation of light under TE and TM polarisation. It is found from the Fig. 4.17 and Fig. 4.18 the typical attenuation of light by the VOA are found to be 2.07 dB/mm for TE and 3.58 dB/mm for TM polarisations respectively.

4.1.7 Mach-Zehnder Modulator: Modulation Characteristics

The optical modulation characteristics of MZMs were measured by using the electrical probing system integrated with the end-fire optical coupling setup shown in Fig. 4.16. The laser light of wavelength $\sim$1550 nm obtained from the tunable laser was controlled by using the polarization controller, collimated by the collimation lens to get the pencil beam of light and passed horizontally in space. The collimated light beam was polarized by the polarizer then coupled into a MZM using the input coupling lens. The light output from the MZM was collected by the output coupling lens and measured by the optical power meter. The anode and cathode metal pads of MZM were connected to the variable, direct current source by using the two probing tips. The optical power output from the MZM was measured as a function of injected current while keeping the input optical power and polarization constant.

The light guided by the input waveguide of the MZM is equally splitted by the 1x2 MMI splitter and which are feed through the reference arm and modulator arm of MZM respectively. The light wave which is guided by the modulator arm passes into the p-i-n

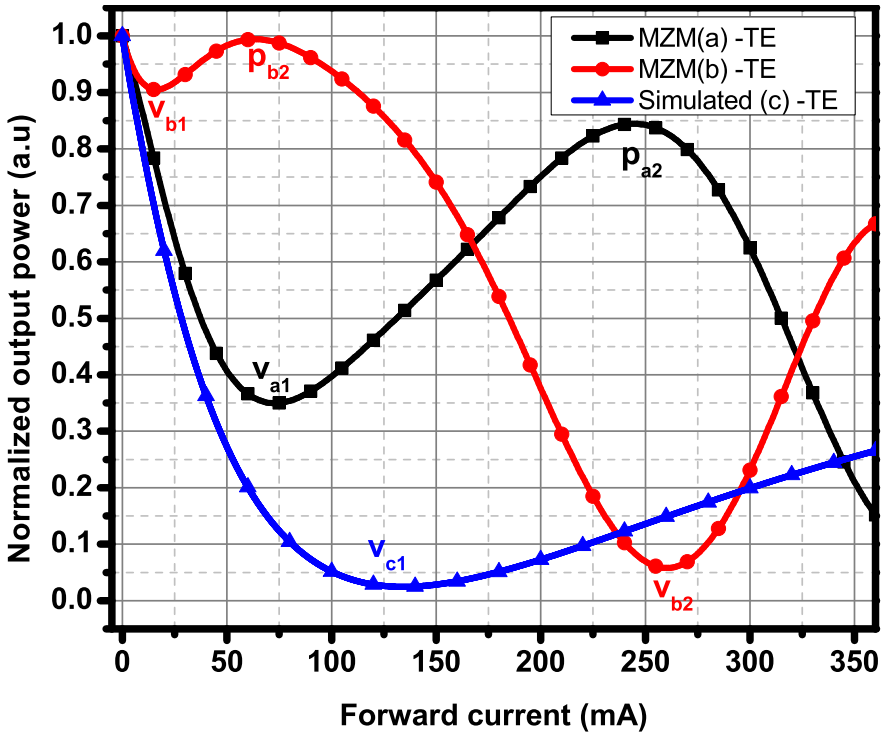

Figure 4.19: Optical modulation characteristics of Mach-Zehnder modulator (MZM): The optical output power as a function of injected current for TE polarization at λ = 1550 nm.

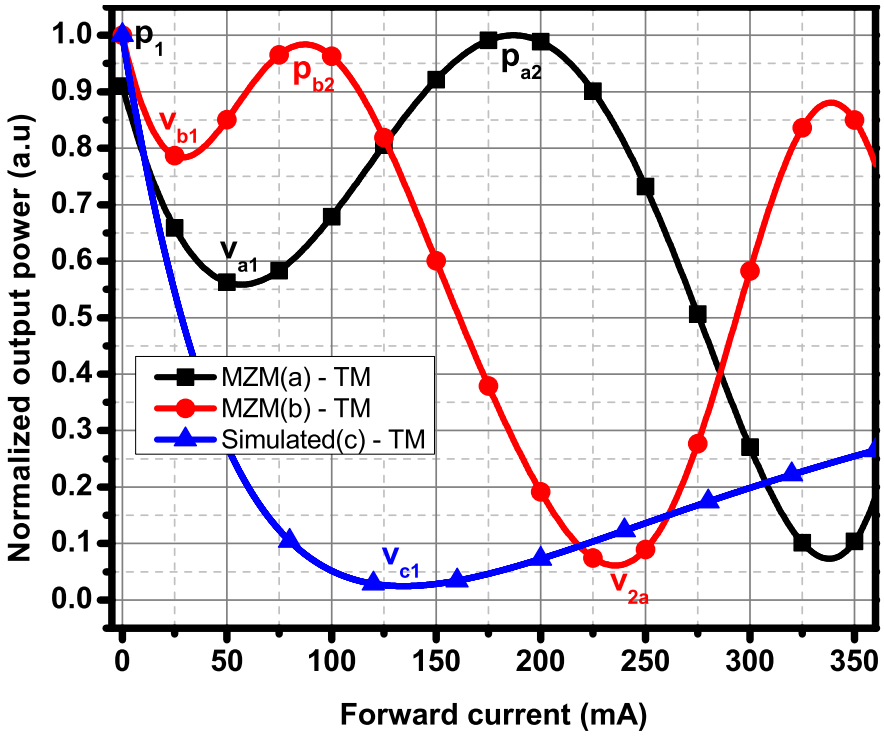

Figure 4.20: Optical modulation characteristics of Mach-Zehnder modulator (MZM): The optical output power as a function of injected current for TM polarization at λ = 1550 nm.

waveguide, hence it acquires additional phase and attenuation according to the driving electrical signal. The light which is guided by the reference arm does not acquire any additional phase and absorption. When these two guided light waves are combined and made to interfere at the 2x1 MMI combiner, they produce interference patterns at the output port of MZM according to their phase differences. When the phase differences are $2m\pi$, they produce a maximum light intensity and the light is coupled and guided by the output waveguide, but when the phase difference become $(2m + 1)\pi$ with m = 0,1,2,3, . . . etc. they produce destructive interference, hence a very little optical power is coupled into the output waveguide of MZM.

Experimental (cuves 'a' and 'b') and simulated (curve 'c') direct current modulation characteristics of MZM for the TE and TM polarizations are shown in Fig. 4.19 and Fig. 4.20 respectively. The simulated curve for optical power output of MZM which accounts for plasma dispersion alone in silicon at room temperature falls rapidly with increase in injected current and gets minimum at 130 mA. When the current is increased beyond 130 mA, the optical output power slowly increases and reaches a second maximum (whose value is less than that of the first maximum) at very large value of current (which has not been shown in the figure). The experimental curve for optical power output of MZM falls rapidly with the increase in the injected current as predicted by the simulation, but gets minimum at a current value well less than that of 130 mA then it tend to increase with increasing current. Since, at these current level the Joule-heating (I^2R loss) of the silicon causes the temperature to rise above the room-temperature and produce the positive refractive index change due to thermo-optic effect which tend to counter act the effect of plasma dispersion in silicon.

The typical modulation characteristics for TE polarized light shown in the Fig. 4.19 exhibits extinction ratio of 4.56 dB (mostly due to the plasma dispersion effect) and 12.37 dB (mostly due to the thermo-optic effect) (by considering the second peak and second valley of the curve 'b'). And the typical modulation characteristics for TM polarized light shown in the Fig. 4.20 exhibits extinction ratio of 2.53 dB (mostly due to the plasma dispersion effect) and 12.07 dB (mostly due to the thermo-optic effect) (by considering the second peak and second valley of the curve 'b'). However these values are found to be less than that of the theoretically predicted value of 16.08 dB by

considering only plasma dispersion.

4.2 Conclusions

The VOA and MZI modulators were fabricated and the attenuation and phase characteristics respectively were studied and compared with simulation results. Typical attenuation of VOA was measured to be $\sim$2.07 (3.67) dB/mm for TE(TM)-polarized light ($\lambda \sim 1550$ nm) at a forward current of 15 mA. The voltage for 180^o phase shift and the figure of merit of the phase shifter is found to be 1.57 V and 0.36 V-mm. The extinction ratio of the MZI modulator for TE and TM polarizations are found to be 12.37 dB and 12.07 dB respectively.

CHAPTER 5

Summary and Conclusions

The p-i-n waveguide phase-shifter and/or variable optical attenuator with single mode SOI rib waveguide structures (device layer - 5 μm) have been designed, fabricated, and integrated successfully into one of the arms of a MMI based MZI. The design parameters of single mode waveguides, 1X2 MMI power splitter, and MZI structure were designed using RSoft BeamProp simulator.

The fabricated test waveguides were characterized for its single-mode guidance (at $\lambda \sim 1550\ nm$) and the guided mode profiles were found to be nearly polarization independent (5.4x3.4 μm^2). The insertion loss of these waveguides were measured by using the end-fire optical coupling system (with 20X objective, NA = 0.65). A typical value of insertion loss for $W \sim 4$ μm waveguide was found to be 6.13 (5.86) dB for TE (TM) polarization and for $W \sim 5.5$ μm waveguides, it was found to be 6.43 (4.65) dB for TE (TM) polarization. However, these losses would have been less if we could use Inductively Coupled Plasma etching instead of Reactive Ion Etching during the waveguide definition on wafers. The 3-dB MMI splitters were characterized in terms of splitting ratio (nearly 50:50), insertion loss (6.5 dB), and wavelength dependencies (flat response for optical C-band). The fabricated MZIs also show a flat wavelength response for full optical C band and the insertion loss variation over full C and L band has been found to be within 4(3) dB for TE(TM) polarization. Typical insertion was found to be 7.15 (6.43) dB for TE (TM) polarization at $\lambda \sim 1550$ nm.

The diffusion doping parameters for p-i-n waveguide structures (width - 4 μm) using MEDICI simulation tools. The 4-μm pin waveguides are integrated with 5.5 μm waveguides in either sides through adiabatic tapers. This is to facilitate better light coupling into the device. Physical processes which have been considered for the simulations were Shockley-Read-Hall recombination, Auger recombination, field dependent mobility, concentration dependent mobility, influence of carrier-carrier scattering on mobility and surface recombination of electrons and holes. The I-V characteristics of

the fabricated p-i-n diodes / waveguides of length L = 230 μm were characterized by using the semiconductor device parameter analyzer (Agilent B1500A). The typical value of reverse saturation current and forward series resistance (at +1V bias) were found to be of the order of 3 nA and 900 Ω (which includes the contact resistance between the probe tips and metal pads), respectively. The attenuation and phase characteristics of fabricated p-i-n waveguides were studied and compared with simulation results. The attenuation characteristic of VOA for TM polarized light follows the simulated characteristics upto 40 mA, however the experimental curve deviated for lager values of injected current. The experimental attenuation of light by VOA for TE polarization follows the trend of corresponding simulated characteristics but with a constant negative shift, this may be attributed to relatively less confinement and hence as is the interaction of the fundamental mode with the injected carriers. Typical attenuation of VOA was measured to be $\sim$2.07 (3.67) dB/mm for TE(TM)-polarized light ($\lambda \sim$ 1550 nm) at a forward current of 15 mA.

The voltage for π phase shift (V_{pi}) and the figure of merit ($V_{pi}L$) of the p-i-n waveguide were estimated to be 1.57 V and 0.36 V-mm, respectively. The extinction ratio of the Mach-Zehnder modulator for TE and TM polarizations were found to be 12.37 dB and 12.07 dB respectively which are less than the estimated extinction of 16 dB. However the extinction could be improved if we could balance mismatch in the phase due to presence p-i-n structure in modulator arm and mismatch due to fabrication errors by biasing another p-i-n structure housed at other arm of MZI. These deviation of the experimental characteristic of both VOAs and MZMs from the respective estimated characteristics may be attributed to thermooptic effect caused by joule heating of silicon and hence the counter acting thermooptic effect. However, the strength of detrimental thermooptic effect may be minimized by reducing the contact resistance of aluminum metal with diffused regions of silicon; by optimizing annealing temperature and time after patterning the metal. Also, instead of using only aluminum layer a stack of Ti/Al layers may be used with optimized metal deposition and annealing processes.

5.0.1 Outlook

The frequency response characteristics of the fabricated variable optical attenuators (VOAs) and Mach-Zehnder modulators (MZMs) may be studied for further investigations. The current induced heating effect (Joule heating) need to be studied since the themooptic effect based devices could be useful for slow switching applications. High speed optical modulators in submicron dimensional waveguides operating in depletion mode may be designed with p^+pnn^+ diodes with traveling wave electrodes. The interaction length of the modulators and hence the power dissipation may be decreased by integrating photonic crystals with the phase shifting regions to get slow light propagation. Since, in real time the temperature dependent effects are very important, a thermal model may be developed for both variable optical attenuators and modulators.

CHAPTER 6

APPENDIX

6.1 TCE and Acetone cleaning

The trychloroethelene commonly known as TCE is a halocarbon. It is an organic solvent used to degrease the wafers. Wafers are placed inside glass beakers with TCE then ultrasonic treatment is carried out for 2 minutes and heated to 70 ^0C for 2 minutes. In order to remove the traces of TCE from the wafer, the TCE solution is poured out then the beaker is filled with Acetone. The above mentioned ultrasonic treatment and heating are repeated. The wafers are taken out from the beakers,rinsed thoroughly in DI water and dried using nitrogen air gun.

6.2 Piranha Cleaning

Followed by every photolithographic processes, the removal organic compounds such as of photoresists from the wafer surface is done using Piranha solution. Which is a mix of the acid H_2SO_4 and a strong oxidizer H_2O_2 in the ratio of 3:1. This solution removes the organic compounds such as photoresists by decomposing it into CO_2 and H_2O. This reaction is basically exothermic hence should be carried out carefully. A piranha solution is prepared in the teflon beaker and the samples from which photoresists to be removed are kept inside the solution until the air bubbles formation is reduced. The samples are taken out from the beaker and rinsed thoroughly in DI water and dried using nitrogen air gun.

6.3 RCA-1 and RCA-2 Cleaning

The main aim of the RCA-1 cleaning of wafers is to remove the trace level impurities such as metals in group IB and IIB of periodic table and other metals such as Gold, Silver, Copper, Nikkel, Zinc, Cadmium, Cobalt and Chromium. This high PH solution consists of a mixer of the substances (H_2O : H_2O_2 : NH_4OH :: 5:1:1). When the solution is heated about 70 - 80 ^0C with the wafer for 15 minutes, it reacts with the wafer surface to form metal complexes, oxidize organic films, dissolves the native oxide and forms a new oxide layer. In this way a fresh wafer surface is obtained.

The RCA-2 solution consists of a mixer of the substances (H_2O : H_2O_2 : HCL :: 6:1:1) when heated to 70 - 80 ^0C with the wafers for 15 minutes, the RCA-1 insoluble hydroxides of alkalies and cation metals; Al^{3+}, Fe^{2+}, Mg^{3+} are dissolved. This RCA-2 solution also removes Au which might not have been removed by RCA-1 solution.

REFERENCES

[1] S. G. Mikhail Efimovich Levinshtein, *Transistors: From Crystals to Integrated Circuits*. World Scientific, 1998.

[2] D. M. Krzysztof Iniewski, Carl McCrosky, *Network Infrastructure and Architecture: Designing High-Availability Networks*. Wiley, 2008.

[3] J. D. Minford, *Handbook of aluminium bonding technology and data*. CRC Press, 1993.

[4] P. C. Andricacos, C. Uzoh, J. O. Dukovic, J. Horkans, and H. Deligianni, "Damascene copper electroplating for chip interconnections," *IBM Journal of Research and Development*, vol. 42, no. 5, pp. 567–574, 1998.

[5] R. H. Havemann and J. A. Hutchby, "High-performance interconnects: An integration overview," *Proceedings of the IEEE*, vol. 89, no. 5, pp. 586–601, 2001.

[6] M. B. I. S. Fellow. (Oct.) The intel "tri-gate transistor" structure: a closer look@ONLINE.

[7] M. Haurylau, G. Chen, H. Chen, J. Zhang, N. A. Nelson, D. H. Albonesi, E. G. Friedman, and P. M. Fauchet, "On-chip optical interconnect roadmap: challenges and critical directions," *Selected Topics in Quantum Electronics, IEEE Journal of*, vol. 12, no. 6, pp. 1699–1705, 2006.

[8] D. Miller, "Device requirements for optical interconnects to silicon chips," *Proceedings of the IEEE*, vol. 97, no. 7, pp. 1166–1185, 2009.

[9] A. Korpel, "Acousto-optics-a review of fundamentals," *Proceedings of the IEEE*, vol. 69, no. 1, pp. 48–53, 1981.

[10] G. Cocorullo, M. Iodice, and I. Rendina, "All-silicon fabry-perot modulator based on the thermo-optic effect," *Optics letters*, vol. 19, no. 6, pp. 420–422, 1994.

[11] F. Pockels, "Lehrbuch der kristalloptik," *Bull. Amer. Math. Soc. 16 (1909), 37-40 DOI: http://dx. doi. org/10.1090/S0002-9904-1909-01856-7 PII*, pp. 0002–9904, 1909.

[12] M. Takatsuji, "Quantum theory of the optical kerr effect," *Physical Review*, vol. 155, no. 3, p. 980, 1967.

[13] W. Franz, "Influence of an electric field on an optical absorption edge," *Z. Naturforsch, 13a*, vol. 484, 1958.

[14] R. Soref and B. Bennett, "Electrooptical effects in silicon," *Quantum Electronics, IEEE Journal of*, vol. 23, no. 1, pp. 123–129, 1987.

[15] G. T. Reed and A. P. Knights, *Silicon photonics*. Wiley Online Library, 2008.

[16] K. Biwojno, S. Sujecki, A. Vukovic, T. M. Benson, and P. Sewell, "Thermal models for silicon-on-insulator-based optical circuits," *Optica Applicata*, vol. 34, no. 2, pp. 149–162, 2004.

[17] T. S. Moss, G. J. Burrell, and B. Ellis, *Semiconductor opto-electronics*. Butterworths London, 1973, vol. 11.

[18] A. Liu, R. Jones, L. Liao, D. Samara-Rubio, D. Rubin, O. Cohen, R. Nicolaescu, and M. Paniccia, "A high-speed silicon optical modulator based on a metal–oxide–semiconductor capacitor," *Nature*, vol. 427, no. 6975, pp. 615–618, 2004.

[19] D. J. Thomson, F. Y. Gardes, J.-M. Fedeli, S. Zlatanovic, Y. Hu, B. P. P. Kuo, E. Myslivets, N. Alic, S. Radic, G. Z. Mashanovich *et al.*, "50-gb/s silicon optical modulator," *Photonics Technology Letters, IEEE*, vol. 24, no. 4, pp. 234–236, 2012.

[20] C. Tang, G. Reed, A. Walton, and A. Rickman, "Low-loss, single-model optical phase modulator in simox material," *Lightwave Technology, Journal of*, vol. 12, no. 8, pp. 1394–1400, 1994.

[21] C. Kopp, S. Bernabe, B. B. Bakir, J. Fedeli, R. Orobtchouk, F. Schrank, H. Porte, L. Zimmermann, and T. Tekin, "Silicon photonic circuits: On-cmos integration, fiber optical coupling, and packaging," *Selected Topics in Quantum Electronics, IEEE Journal of*, vol. 17, no. 3, pp. 498–509, 2011.

[22] W. Fang, S.-S. Li, C.-L. Cheng, C.-I. Chang, W.-C. Chen, Y.-C. Liu, M.-H. Tsai, and C. Sun, "Cmos mems: A key technology towards the "more than moore" era," in *Solid-State Sensors, Actuators and Microsystems (TRANSDUCERS & EUROSENSORS XXVII), 2013 Transducers & Eurosensors XXVII: The 17th International Conference on*. IEEE, 2013, pp. 2513–2518.

[23] F. Arnaud, A. Thean, M. Eller, M. Lipinski, Y. Teh, M. Ostermayr, K. Kang, N. Kim, K. Ohuchi, J.-P. Han *et al.*, "Competitive and cost effective high-k based 28nm cmos technology for low power applications," in *Electron Devices Meeting (IEDM), 2009 IEEE International*. IEEE, 2009, pp. 1–4.

[24] M. A. Taubenblatt, "Optical interconnects for high-performance computing," *Lightwave Technology, Journal of*, vol. 30, no. 4, pp. 448–457, 2012.

[25] N. Savage, "Light from silicon [silicon-based lasers]," *Spectrum, IEEE*, vol. 41, no. 1, p. 59, 2004.

[26] H. Rong, R. Jones, A. Liu, O. Cohen, D. Hak, A. Fang, and M. Paniccia, "A continuous-wave raman silicon laser," *Nature*, vol. 433, no. 7027, pp. 725–728, 2005.

[27] H. Rong, S. Xu, Y.-H. Kuo, V. Sih, O. Cohen, O. Raday, and M. Paniccia, "Low-threshold continuous-wave raman silicon laser," *Nature Photonics*, vol. 1, no. 4, pp. 232–237, 2007.

[28] P. Dong, W. Qian, S. Liao, H. Liang, C.-C. Kung, N.-N. Feng, R. Shafiiha, J. Fong, D. Feng, A. V. Krishnamoorthy *et al.*, "Low loss silicon waveguides for application of optical interconnects," in *Photonics Society Summer Topical Meeting Series, 2010 IEEE*. IEEE, 2010, pp. 191–192.

[29] E. Onaran, M. C. Onbasli, A. Yesilyurt, H. Y. Yu, A. M. Nayfeh, and A. K. Okyay, "Silicon-germanium multi-quantum well photodetectors in the near infrared," *Opt. Express*, vol. 20, p. 7608, 2012.

[30] F. Gardes, D. Thomson, N. Emerson, and G. Reed, "40 gb/s silicon photonics modulator for te and tm polarisations," *Optics express*, vol. 19, no. 12, pp. 11 804–11 814, 2011.

[31] H. Yue-Jiao, L. Fang, and L. Yu-Liang, "Silicon-on-insulator based electro-optic variable optical attenuator with a series structure," *Chinese Physics Letters*, vol. 22, no. 1, p. 95, 2005.

[32] I. Krubhakar, R. Narendran, Y. Karthik, and B. Das, "Fabrication of $1\times$ 8 integrated optical power splitter in soi substrate with optimized design parameters."

[33] G. Bhatt and B. Das, "Demonstration of itu channel interleaver in soi with large cross section single mode waveguides," in *SPIE Microtechnologies*. International Society for Optics and Photonics, 2011, pp. 806 904–806 904.

[34] X. Zheng, I. Shubin, G. Li, T. Pinguet, A. Mekis, J. Yao, H. Thacker, Y. Luo, J. Costa, K. Raj *et al.*, "A tunable 1x4 silicon cmos photonic wavelength multiplexer/demultiplexer for dense optical interconnects," *Opt. Express*, vol. 18, no. 5, pp. 5151–5160, 2010.

[35] S. Park, K.-J. Kim, I.-G. Kim, and G. Kim, "Si micro-ring mux/demux wdm filters," *Optics Express*, vol. 19, no. 14, pp. 13 531–13 539, 2011.

[36] S. Sudo, K. Mizutani, M. Nielsen, T. Okamoto, K. Tsuruoka, K. Sato, and K. Kudo, "Over 100-mw output power operation of voa integrated full c-band external cavity wavelength tunable laser utilizing high-refractive-index gap mirror," in *Semiconductor Laser Conference, 2006. Conference Digest. 2006 IEEE 20th International*. IEEE, 2006, pp. 19–20.

[37] M. Jung and J. Han Lee, "Actively q-switched, thulium–holmium-codoped fiber laser incorporating a silicon-based, variable-optical-attenuator-based q switch," *Applied optics*, vol. 52, no. 12, pp. 2706–2710, 2013.

[38] L. Wang, B. Hwang, and L. Yang, "Gain transients in copumped and counterpumped raman amplifiers," *Photonics Technology Letters, IEEE*, vol. 15, no. 5, pp. 664–666, 2003.

[39] S. Park, T. Tsuchizawa, T. Watanabe, H. Shinojima, H. Nishi, K. Yamada, Y. Ishikawa, K. Wada, and S. Itabashi, "Monolithic integration and synchronous operation of germanium photodetectors and silicon variable optical attenuators," *Optics Express*, vol. 18, no. 8, pp. 8412–8421, 2010.

[40] H. Chen, "Multiwavelength fiber ring lasing by use of a semiconductor optical amplifier," *Optics letters*, vol. 30, no. 6, pp. 619–621, 2005.

[41] D. Zheng, B. Smith, and M. Asghari, "Improved efficiency si-photonic attenuator," *Opt. Express*, vol. 16, no. 21, pp. 16 754–16 765, 2008.

[42] H. Dai, J.-Y. Pan, and C. Lin, "All-optical gain control of in-line erbium-doped fiber amplifiers for hybrid analog/digital wdm systems," *Photonics Technology Letters, IEEE*, vol. 9, no. 6, pp. 737–739, 1997.

[43] W. Bernhard, R. Mueller-Fiedler, T. Pertsch, and C. A. Waechter, "Cross talk reduction in switching networks by asymmetrical off-on switches," in *Optoelectronics' 99-Integrated Optoelectronic Devices*. International Society for Optics and Photonics, 1999, pp. 24–32.

[44] N. Takachio, H. Suzuki, M. Koga, and O. Ishida, "Wdm linear repeater gain control scheme by automatic maximum power channel selection for photonic transport network," in *Optical Fiber Communication Conference and Exhibit, 1998. OFC'98., Technical Digest*. IEEE, 1998, pp. 165–166.

[45] D. Downey, K. Jones, M. Farley, and G. Ryding, "Ion implantation technology," 1993.

[46] Y.-F. Liu, H.-Z. Yin, and H.-L. Zhu, "A new method to repair ion implantation-induced damage in the gate dielectric layer of mosfets," in *Solid-State and Integrated Circuit Technology (ICSICT), 2012 IEEE 11th International Conference on*. IEEE, 2012, pp. 1–3.

[47] B. Ginsberg, J. Burghartz, G. Bronner, and S. Mader, "Selective epitaxial growth of silicon and some potential applications," *IBM journal of research and development*, vol. 34, no. 6, pp. 816–827, 1990.

[48] G. Parker and C. Starbuck, "Selective silicon epitaxial growth by lpcvd using silane," *Electronics Letters*, vol. 26, no. 13, pp. 831–832, 1990.

[49] S. K. Ghandhi, *VLSI fabrication principles: silicon and gallium arsenide*. Wiley. com, 2008.

[50] J. D. Plummer, *Silicon VLSI technology: fundamentals, practice, and modeling*. Pearson Education India, 2009.

[51] L. B. Soldano and E. C. Pennings, "Optical multi-mode interference devices based on self-imaging: principles and applications," *Lightwave Technology, Journal of*, vol. 13, no. 4, pp. 615–627, 1995.

GENERAL TEST COMMITTEE

CHAIR PERSON
Dr. Harishankar Ramachandran
Head of the department
Professor
Dept. of Electrical Engineering
IIT-Madras, 600 036

RESEARCH GUIDES

Dr. Nandita Dasgupta
Research Guide
Professor
Dept. of Electrical Engineering
IIT-Madras, 600 036

Dr. Bijoy Krishna Das
Research Guide
Associate Professor
Dept. of Electrical Engineering
IIT-Madras, 600 036

MEMBERS

Dr. Enakshi Bhattacharya
Professor
Dept. of Electrical Engineering
IIT-Madras, 600 036

Dr. G. Ramanathan
Professor
Dept. of Chemical Engineering
IIT-Madras, 600 036

LIST PUBLICATIONS

P. Sakthivel, N. DasGupta and B. K. Das "Simulation and Experimental Studies of Diffusion Doped p-i-n Structures for Silicon Photonics", SPIE PHOTONICS WEST, San Francisco, California, USA Feb. 2013.

EDUCATION

B.Sc. Physics from Government Arts College, Thiruvanamalai, in 1999.

M.Sc. Physics from Sri R.K.M. Vivekananda college, Mylapore Chennai-4, in 2008.